University of New Mexico
UNM Digital Repository

Chemical and Biological Engineering ETDs | Engineering ETDs

9-10-2010

Field-structured chemiresistors : tunable sensors for chemical-switch arrays

Douglas Read

Follow this and additional works at: https://digitalrepository.unm.edu/cbe_etds

Recommended Citation
Read, Douglas. "Field-structured chemiresistors : tunable sensors for chemical-switch arrays." (2010).
https://digitalrepository.unm.edu/cbe_etds/3

This Dissertation is brought to you for free and open access by the Engineering ETDs at UNM Digital Repository. It has been accepted for inclusion in Chemical and Biological Engineering ETDs by an authorized administrator of UNM Digital Repository. For more information, please contact disc@unm.edu.

Douglas H Read
Canidate

Chemical and Nuclear Engineering
Department

This dissertation is approved, and it is acceptable in quality and form for publication:

Approved by the Dissertation Committee:

, Dr. Plamen Atanassov, PhD, Chairman

, Dr. James E Martin, PhD, Research Advisor

, Dr. John G Curro, PhD

, Dr. Steven J Koch, PhD

, Dr. Dimiter N Petsev, PhD

FIELD-STRUCTURED CHEMIRESISTORS: TUNABLE SENSORS FOR CHEMICAL-SWITCH ARRAYS

BY

DOUGLAS H READ

B.S., Chemical Engineering, University of New Mexico, 2003

DISSERTATION

Submitted in Partial Fulfillment of the
Requirements for the Degree of

Doctor of Philosophy

Engineering

The University of New Mexico
Albuquerque, New Mexico

July, 2010

Dedication

First and foremost I would like to give the utmost thanks to my advisor Dr. James Martin, to whom I dedicate this dissertation. Without his selfless dedication, patience and support as well as his brilliant and creative ideas, this work would not have been possible. He has not only instructed me technically, but through his example he has also taught me many life lessons—in short, how to be a man. I am not only proud and honored to call Dr. Martin my pedagog, but also my close friend.

I would also like to thank my wonderful wife Anita for her undying patience and support. Anita, you have been my foundation.

To my parents, words cannot express my gratitude for all of the support you have given me over the years. You have taught me that through hard work and perseverance anything is possible. And to my sisters, I thank you for always being there for me.

To my friend Kyle, for as long as I can remember you have been there for me—always with a listening ear. Thank you for your years of support and friendship.

ACKNOWLEDGMENTS

RESEARCH ADVISOR
Dr. James E. Martin, PhD, Sandia National Labs

DISSERTATION COMMITTEE CHAIR
Dr. Plamen Atanassov, PhD, University of New Mexico

DISSERTATION COMMITTEE MEMBERS
Dr. John G. Curro, PhD, University of New Mexico
Dr. Steven J. Koch, PhD, University of New Mexico
Dr. Dimiter N. Petsev, PhD, University of New Mexico

COLLABORATORS
Dr. Rodney Williamson, PhD, Sandia National Labs (Retired)
Dr. Gerald Gulley, PhD, Dominican University and Sandia National Labs
Brad Butler, Sandia National Labs (former undergraduate student intern)
Gavin Kurey, Sandia National Labs (former undergraduate student intern)

I would like to give special thanks to Alex Robinson (Sandia National Laboratories) for providing me with the latest generation sensor substrates, which he designed.

RESEARCH INSTITUTION
The entirety of this work was conducted at Sandia National Laboratories.

Sandia National Laboratories is a multi-program laboratory managed and operated by Sandia Corporation, a wholly owned subsidiary of Lockheed Martin Corporation, for the U.S. Department of Energy's National Nuclear Security Administration under contract DE-AC04-94AL85000.

FUNDING
This work was fully supported by the Division of Materials Science, Office of Basic Energy Sciences, U.S. Department of Energy (DOE).

FIELD-STRUCTURED CHEMIRESISTORS: TUNABLE SENSORS FOR CHEMICAL-SWITCH ARRAYS

by

Douglas H Read

B.S., CHEMICAL ENGINEERING, UNIVERSITY OF NEW MEXICO, 2003

PH.D, ENGINEERING, UNIVERSITY OF NEW MEXICO, 2010

ABSTRACT

We have developed a significantly improved composite material for applications to chemiresistors, which are resistance-based sensors for volatile organic compounds. This material is a polymer composite containing Au-coated magnetic particles organized into electrically conducting pathways by magnetic fields. This improved material overcomes the various problems inherent to conventional carbon-black chemiresistors, while achieving an unprecedented magnitude of response. When exposed to chemical vapors, the polymer swells only slightly, yet this is amplified into large, *reversible* resistance changes—as much as 9 decades at a swelling of only 1.5 %. These conductor-insulator transitions occur over such a narrow range of analyte vapor concentration that these devices can be described as chemical switches. We demonstrate that the sensitivity and response range of these sensors can be tailored over a wide range by controlling the stress within the composite, including through the application of a magnetic field. Such tailorable sensors can be used to create sensor arrays that can accurately determine analyte concentration over a broad concentration range, or can be used to create logic

circuits that signal a particular chemical environment. It is shown through combined mass-sorption and conductance measurements, that the response curve of any individual sensor is a function of polymer swelling *alone*. This has the important implication that individual sensor calibration requires testing with only a single analyte. In addition, we demonstrate a method for analyte discrimination based on sensor response kinetics, which is independent of analyte concentration. This method allows for discrimination even between chemically similar analytes. Lastly, additional variables associated with the composite and their effects on sensor response are explored.

TABLE OF CONTENTS

1. INTRODUCTION

Chemical sensors are invaluable resources used for a diverse number of applications. We use them every day in our cars (O_2 sensors and emission analyzers) and in our homes (smoke and carbon monoxide detectors). They are used by military, law enforcement, and for homeland security. In industry, chemical sensors are used to monitor and control chemical processes and to ensure safe working environments. In addition, there is growing concern over the ever-increasing environmental impact of industrial pollutants. Initiatives to control and mitigate the release of these pollutants—or to monitor reclamation site progress—depend on the ability to determine their concentrations in the field. Chemical sensing technologies capable of performing this task, such as GC-mass spectrometry or selective-polymer piezoelectric resonators, are generally robust and sensitive, but have several disadvantages associated with them. Simply stated these sensors are largely impractical for field use, due to excessive cost, size, power consumption, complexity or fragility. For these reasons there is a continuing need for an inexpensive, compact, robust and tailorable chemical sensor that has a transduction mechanism suitable for a portable field unit. Such a sensor would be useful for industrial pollution monitoring, leak detection for remote storage vessels or pipelines, contaminated site remediation monitoring, and water and air surety. It could also be an enabling technology for the embedded environmental monitoring networks that are now under development.[1–3] We have succeeded in developing a field-structured composite material that enables chemiresistors to fulfill these requirements. These *Field-Structured Chemiresistors* (FSCRs) have such an abrupt conductivity transition that they can serve as elements of chemical logic circuits, and their response can be controlled by managing

the stress field within the composite. We have developed many methods for controlling this stress to include processing methods which result in a permanent sensitivity change and dynamic tuning methods such as the use tensile strain or magnetic fields. Due to the high level of control we have achieved over their sensitivity, arrays of these sensors can be used to determine analyte concentration accurately over a broad range with simple assay-type logic circuits. This high level of control we have over sensor response has enabled us to identify the variables that affect response—as well as those that do not. In this dissertation we discuss the underpinning science and development of this sensor technology.

2. BACKGROUND: REVIEW OF CHEMICAL SENSORS

This chapter serves as an overview of various chemical sensor technologies to include how they work and their associated advantages and disadvantages. The following chapter concludes with an introduction to field-structured chemiresistors followed by a comparison to existing chemiresistor technologies.

2.1. Chemical Sensing Terminology

It is helpful to begin by introducing the terminology typically used to describe sensor response.[4] The term ***sensitivity*** refers to the slope of the sensor response curve or. The detection limits of a sensor are the minimum and maximum analyte concentrations that can be detected. The lower and upper detection limits, ***LDL*** and ***UDL*** respectively, are set at a response signal-to-noise ratio that is equal to a specified confidence limit (typically 3σ of the baseline signal). ***Range*** refers to the span of concentrations between the LDL and UDL (e.g. 1–10 *ppm* xylene). ***Dynamic range*** is a measure of the magnitude of the range and is defined the ratio between the UDL to the LDL. The ***baseline*** or ***offset*** of the sensor is the mean value of the transduction signal when no analyte is present. ***Response time*** is the amount of time it takes for the sensor's transduction signal to reach steady-state with a change in analyte concentration. Finally, analyte ***selectivity*** refers to the sensitivity of a sensor to a particular analyte, or class of analytes, with respect to other analytes. It is generally desirable, to have a sensor that is selective to the analyte of interest and insensitive to other chemicals, particularly those found readily in ambient conditions, such as water.

2.2. Analyte Concentration and Activity

It is also helpful to define the various forms of analyte concentration to which we will be referring. *C* refers to an amount analyte per unit volume of carrier gas. The units of *C* will typically be in terms of mass of analyte per unit volume of carrier gas such as μg/mL. Analyte concentration can also be expressed in *part-per-million* (*ppm*) and is defined as the number of moles of analyte per the number of moles of carrier gas or $C(ppm) = n / n_{N_2} \times 10^6\, ppm$. Finally, we often describe concentration in terms of a dimensionless variable, *activity, a*. Activity is used to describe an analyte's concentration normalized by its concentration at the point of total saturation. Activity is defined as the analyte's vapor pressure, *p*, divided by its saturation vapor pressure, *p**, or $a \equiv p(T) / p^*(T)$. Therefore, the concentration range of an analyte, in terms of activity, ranges from zero to one. In Section 3.5. we discuss the difference between concentration and activity as it relates to sensor response. Derivation of concentration in terms of experimental variables and expressions for the conversion between the unit systems can be found in Appendix C.1.

2.3. Gas Chromatography

A gas chromatograph (GC) is an instrument that has the ability to analyze complex mixtures of volatile organic compounds (VOCs). It works by using a carrier gas to push the analytes through an immobilized adsorbent. The analytes are separated based on their differing affinities for the adsorbent (partition coefficient). In other words, the residence time of the analyte in the column is proportional to its partition coefficient with respect to the immobile phase. Upon exiting the column the separated analytes flow to a detector where they can be identified and quantified. Types of detectors that are used include: photoionization detector (PID), flame ionization detector (FID), thermal conductivity detector (TCD), and electron capture detector (ECD).[5] Gas chromatography can also be combined with mass spectrometry for analyte detection (GC/MS). In this configuration and after being separated, the analyte is ionized and identified by its mass-to-charge ratio as shown in Figure 2-1 below.[6]

PIDs are one of the more common types of detectors and are available in hand-held models without the GC (RAE Systems Inc.) as seen below in Figure 2-2. PIDs have excellent sensitivity and precision and are capable of detecting VOC levels upwards of 0.1 ppm. PIDs, however, are not able to differentiate between different chemicals and are very expensive.

Gas chromatographs in general are very sensitive and can sense a broad range of chemicals simultaneously, but have several drawbacks. Bench top GCs versions are large (in terms of size and weight), complex, and expensive. For example the Agilent bench-top GC (model 6890) weighs over a hundred pounds, is 20×23×21 in., costs between $20,000 and $50,000 and requires a trained operator. Portable GCs such as the

Femtoscan and the HAPSITE are improvements in terms of size (35lbs for the HAPSITE), but still lack the ability for *in situ* analyte monitoring and come with a hefty price tag.

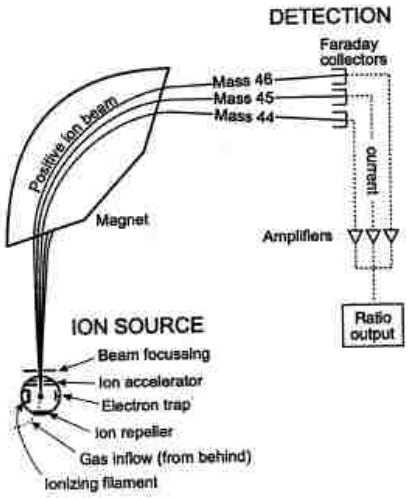

Figure 2-1. Operational schematic of mass spectrometer. The analytes are ionized, deflected, and separated in a magnetic field according to their mass-to-charge ratio. (Reprint from http://pubs.usgs.gov/of/2001/ofr01-257/images/figure1.gif).

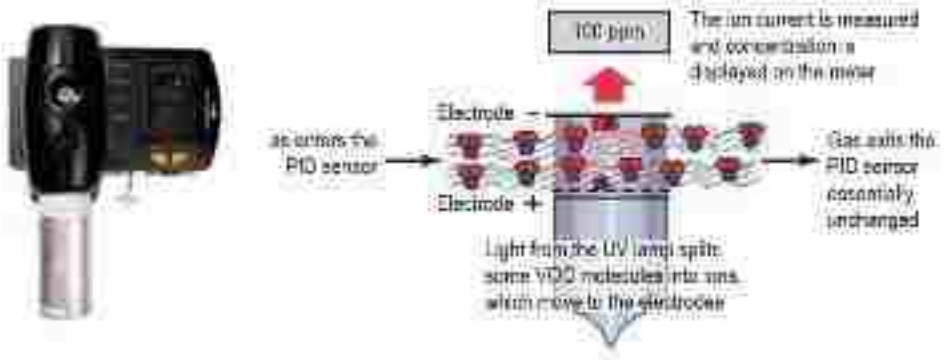

Figure 2-2. Image of a wall mounted PID sensor (Model AutoRAE lite®, RAE Systems Inc.) with a schematic of the PID chemical sensing process. (Reprint from www.raesystems.com).

2.4. Selective Polymer Based Chemical Sensors and The Artificial Nose

Sorption of an analyte into a polymer is the basis of most simple methods of sensing vapors of volatile organic compounds. Such devices include quartz crystal microbalances (QCM) and surface acoustical wave (SAW) sensors that transduce mass sorption into a frequency change,[7–10] and sensors that transduce mass uptake into a resistance, potential, or capacitance change, such as chemiresistors, chemicapacitors and CHEMFETs.[11–20] Regardless of the sensing mechanism, each individual sensor, being comprised of a single polymer, cannot discriminate between analytes if only the equilibrium mass uptake is used, unless somehow the partial pressure of the analyte is either known or measured. This is because a high concentration of analyte with a low affinity for the polymer phase can elicit the same equilibrium response as a low concentration of an analyte that has greater affinity. A single sensor is therefore more often used to measure the concentration of a known analyte.

For these polymer-based sensors, analyte discrimination is currently based on the *artificial nose* (or *electronic nose*) concept, wherein arrays of sensors having differentiating chemical affinities are exposed to the vapor.[19–22] Any analyte will then give a more-or-less unique relative equilibrium mass uptake to the array elements, generating a response fingerprint. This equilibrium approach can enable the discrimination of analytes having disparate chemical affinities, but will not be as useful for distinguishing homologous analytes, such as octane from decane, or xylene from mesitylene. The ability to distinguish between homologous analytes requires nonequilibrium information. We describe such a method for discrimination in Chapter

11. The following sections are an overview the main classes of selective polymer-based sensors.

2.4.1. PIEZOELECTRIC SENSORS: SAWS AND QCMS

Surface Acoustic Wave (SAW) and Quartz Crystal Microbalance (QCM) devices are piezoelectric substrates such as a quartz crystal, which are oscillated at very high frequencies (10–100 MHz). At a given input frequency, the crystal oscillates at its intrinsic resonant frequency. If mass is deposited onto the crystal, this oscillation frequency changes in proportion to this change in mass. QCMs are often used for *in situ* monitoring of thin-film deposition or mass adsorption processes.[23] For the application of VOC sensing, a thin layer of analyte-selective polymer is deposited onto crystal. When analyte is present, it is absorbed into the polymer and the mass uptake is transformed into a frequency shift of the oscillating crystal as depicted below in Figure 2-3.[7,24] These sensors can detect VOCs in very small quantities and have the ability to differentiate between various classes of analyte when several selective polymers are used in an array. Disadvantages include high expense (QCM systems are ~8,000–$10,000) and in some cases high power requirements. In addition they can require complex transduction equipment (crystal oscillator, frequency detector, output transducer) and a computer to receive the data.

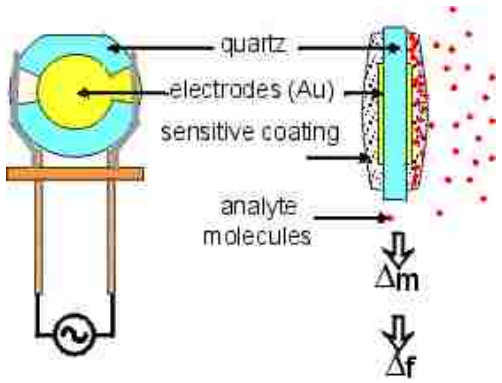

Figure 2-3. Illustration of a selective polymer film on a quartz crystal microbalance sensor. The change in mass due to analyte absorption into the polymer is translated into a change in the frequency of the QCM.

2.4.2. ELECTRONIC-BASED SENSORS

Electronic sensors are composed of materials whose electrical properties—such as resistance, capacitance, or potential—change in the presence of an analyte. We will discuss four types of electronic sensors used for the detection of vapor-phase VOCs: MOS sensors, ChemFETs, chemicapacitors, and conductive composite chemiresistors.

2.4.2.1. METAL-OXIDE SEMICONDUCTOR SENSORS

Metal-oxide semiconductor (MOS) sensors are composed of a porous thick film of polycrystalline SnO_2 as the sensing layer. In ambient conditions, oxygen and water vapor from the air are adsorbed at the surface of the SnO_2 film. The adsorbed oxygen carries a negative charge when the sensor is heated to temperatures between 200°C and 450°C. Electrical current flows through the sensor at the MOS grain boundaries and an increased baseline resistance is caused by the negatively charged oxygen molecules. When a combustible vapor contacts the SnO_2 film, a surface catalyzed reaction takes place with the already adsorbed oxygen and water vapor.[24] For reducing gases such as CO or H_2,

the reaction decreases the resistance of the sensor. For oxidizing gases such as NO_2 and O_3, the resistance increases. The magnitude of the change in resistance depends on variables such as: the microstructure and doping of the base material and on the morphology and geometrical characteristics of the sensing layer and substrate. A change in any of these variables allows for the tuning of the sensitivity towards different classes of analytes. Figaro Sensors has developed a MOS sensor that is capable of detecting VOCs.[26] MOS sensors have a quick response time (on the order of seconds), are relatively inexpensive, and have high sensitivity to combustible compounds. However, MOS sensors have high baseline drift, which greatly decreases its useful resolution. MOS sensors are also selective to water vapor making them problematic in ambient conditions and they do not work well for aromatic and halogenated VOCs.

2.4.2.2. CHEMFETS

Chemical field-effect transistors (ChemFETs) are potentiometric-based sensors that have been used for a variety of applications ranging from ion to bio sensors. We will discuss a variant of this sensor known as the work function field-effect transistor (WF-FET), which is schematically shown in Figure 2-4. ChemFETs are based on a conventional silicon *insulated gate field-effect transistors*, which serves as an impedance transformer and an amplifier. However for ChemFETs, an analyte-selective layer replaces the gate metal. In the presence of a compatible analyte, the electrostatic potential of the gate conductor is changed and the chemical is detected. Therefore for proper operation, an analyte is required to be able to donate or accept electrons in order to change the gate potential.[27] WF-FETs are small and lend themselves to arrays and require little power. However

many analytes irreversibly adsorb to the selective layer and even those that do not typically have long sorption kinetics. Kinetic data reported by Yang et al. (Ref. 28, Fig. 9) shows a single data point taking ~4hrs to collect and ~16hrs for an entire response curve for DMMP (and about half that for the highly volatile analyte MeOH), where the desorption of the analyte appears to be particularly slow. Equilibrium response data for a copper-phthalocyanine thin-film ChemFET reported by Yang et al. are shown in Figure 2-5 below. These data show a maximum 7% response to DMMP. In addition, and because these sensors are solid state, they obviously require semiconductor-process manufacturing.

In his 2004 review article, *Thirty Years of CHEMFETs*, Janata's comment on the state of ChemFETs pretty much sums it up. "[The] Field of solid-state sensors… is vibrant. It is evident from hundreds of papers that have been published within the past ten years. It is, therefore, quite remarkable that there has been no significant commercialization of these sensors, as [of] yet."[27]

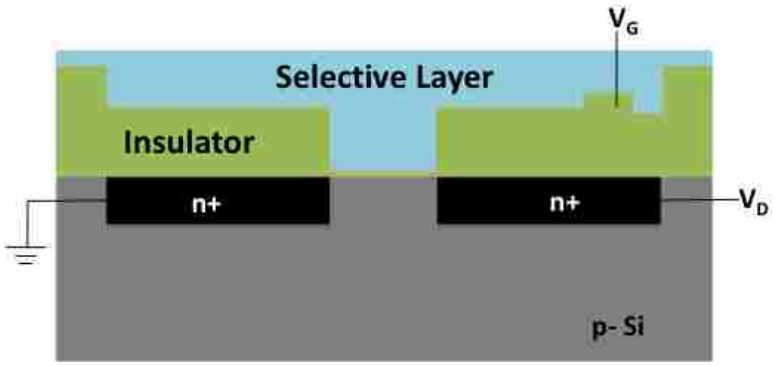

Figure 2-4. General Schematic of a CHEMFET in a work function vapor sensor (WF-FET) configuration.[27]

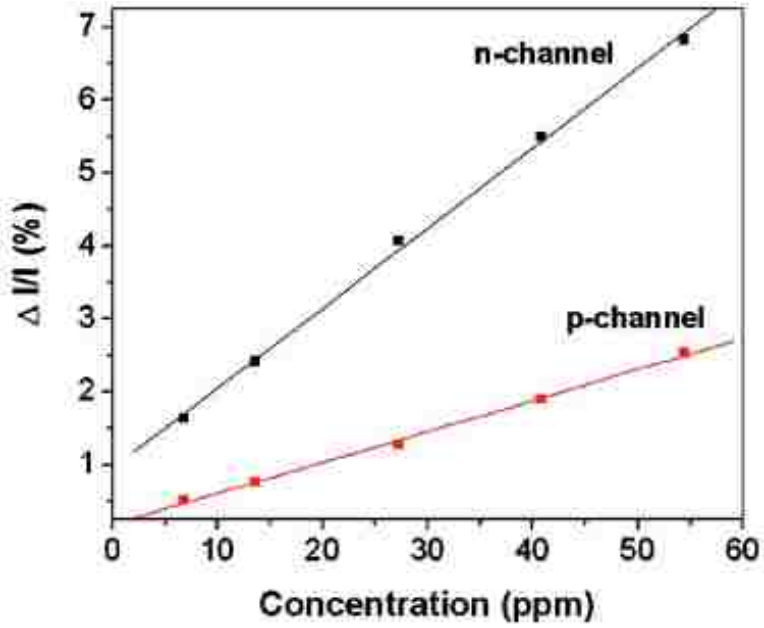

Figure2-5. ChemFET response to DMMP shows a maximum response of ~7 % in terms of relative current change (ΔI/I). This figure is reproduced from Yang et al. (Ref. 28, Fig. 11).

2.4.2.3. CHEMICAPACITORS

Chemicapacitors are VOC sensors, which are capacitors that use a selective polymer as the dielectric medium. Chemicals that absorb into this dielectric alter its permittivity thereby changing the capacitance.[13] Chemicapacitors have been developed with three types of capacitor geometries: (1) interdigitated electrodes, where electrodes lay on the same substrate plane; (2) parallel-plates composed of metal-polymer-metal layers, which cannot be microprinted due to inability to etch the upper electrode due to polymer destruction; and (3) micromachined parallel-plate such as those made by Seacoast Science.[13]

The micromachined parallel-plate capacitors are shown in Figure 2-6 below. The top plate of this sensor contains holes, which allow for transport of the analyte to the polymer layer (Figure 2-6a). The top plate is also anchored to prevent flexing with polymer swelling. The selectivity of a particular sensor is a function of the polymer-analyte interaction and the permittivity of the analyte. Therefore these sensors are especially suited to analytes that meet the criteria of having high permittivity and high polymer affinity. Figure 2-6b shows a linear dependence of equilibrium capacitor output voltage on analyte concentration. Although octane and toluene have similar affinities for the polymer, selectivity arises from their disparate dielectric constants (1.95 and 2.4 respectively). The chemicapacitors described by Patel et al. require a 10 kHz charge/discharge drive voltage and 1.8 V input voltage, though they require little power to operate (< 10mV).[13] These sensors are complex and costly to manufacture due to the extensive micromachining and semiconductor processing. In addition, they suffer from increased response time due to limited mass transport through the upper capacitor plate

before reaching the polymer.[13] SeaCoast Science, Inc. reports a lower detection limit of 61 ppm toluene with their chemicapacitors,[29] where FSCRs are capable of detecting toluene concentrations as low as 13 ppm (0.051 μg/mL).[30]

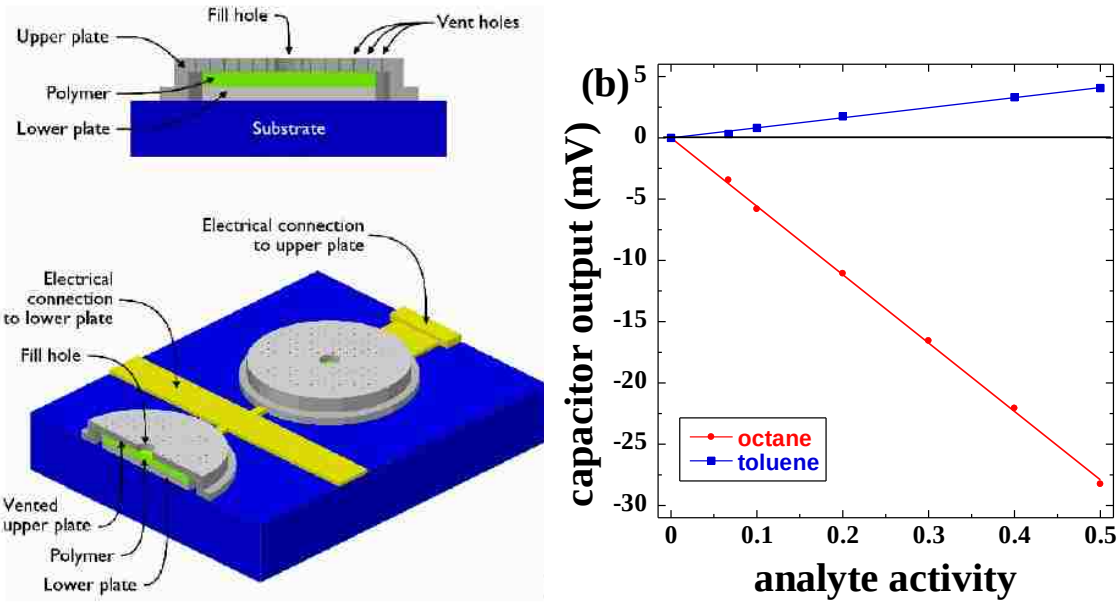

Figure 2-6. Seacoast Science's micromachined parallel-plate chemicapacitors. **(a)** Cross-sectional schematic of the sensor (reprint from Seacoast Science, Inc. "Whitepaper". *www.seacoastscience.com/technology.htm*). **(b)** Data reported by, and digitized from, Patel et al. (Fig. 7, Ref. 13), show a linear dependence of a PIB-filled capacitor output voltage on analyte concentration. Although these analytes have similar affinities for the polymer, selectivity is achieved due to the analytes' disparate dielectric constants.

2.4.2.4. CONDUCTIVE COMPOSITE CHEMIRESISTORS

Chemiresistors are electrically conductive composite materials whose resistance increases in the presence of volatile organic compounds. Chemiresistors traditionally consist of carbon black particles randomly distributed within an amorphous polymer matrix, with the volume fraction of carbon black sufficiently high to create charge-conducting percolative pathways.[31,32] Polymers typically used for Carbon-black Chemiresistors

(CBCRs) include: poly(ethylene-vinylacetate) (PEVA), poly(epichlorohydrin) (PECH), poly(isobutylene) (PIB), and poly(n-vinyl pyrrolidone). Figure 2-7 shows an array of CBCRs.

Chemical vapors swell the polymer matrix, reducing the conductivity by either increasing the contact resistance (reducing contact pressure) between particles or altogether breaking conductive pathways.[33] Carbon black chemiresistors (CBCRs) have several attractive features: they are small (microdot printable), inexpensive to fabricate, and their conductivity transduction mechanism is suitable for portable test units that require little power.[14–19] Chemical identification can be accomplished to some degree with chemiresistor arrays wherein each sensor is fabricated from a polymer that has a distinguishing chemical affinity for the analyte.[21,22,34]

While traditional chemiresistors have positive attributes, they also have significant problems. These include low sensitivity, large conductance drift, large sensor-to-sensor conductance variation, and poor reversibility, especially after exposure to high analyte concentrations. These problems are the result of several inherent traits of the materials used to create the composite as we will discuss in the following sections.

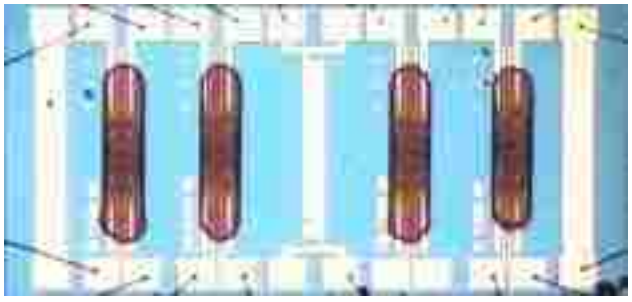

Figure 2-7. An array of four carbon-black chemiresistors on a microelectronic substrate. (Reprint from http://www.sandia.gov/sensor/MainPage.htm).

3. FIELD-STRUCTURED CHEMIRESISTORS

As discussed in the previous chapter, traditional random-composite chemiresistors have many inherent problems with the result that they simply have struggled to become a viable sensor technology. We have discovered that all of the shortcomings can be addressed by using magnetic fields to create reproducible percolative pathways through the polymer. In addition, unlike carbon black the particles used in FSCRs do not strongly adsorb organic compounds. In this section, we will give an overview of the basics of FSCRs.

3.1. What is an FSCR?

Unlike traditional chemiresistors, whose particle network is random, our approach is to force the conducting particles into well-organized percolative pathways to eliminate randomness from the particle composite.[35,36] To accomplish this we apply either simple uniaxial dc or complex, multi-axial ac magnetic fields to dispersions of Au-plated magnetic particles (such as iron or nickel) in curable polymeric resins.[37–39] The schematic and pictures in Figure 3-1 illustrate the various components that make up an FSCR device. Magnetic fields can be used to create a variety of particle organizations, such as the particle chains in Figures 3-1 and 3-2a and the more complex particle sheets and cells in Figure 3-2.

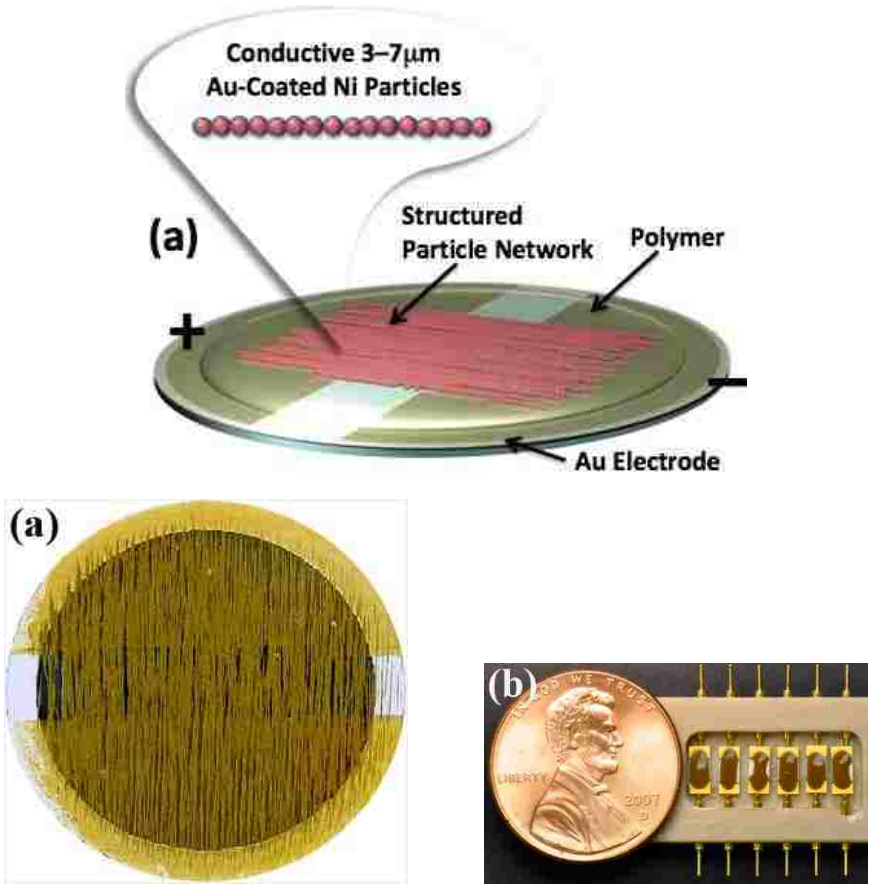

Figure 3-1. **(a)** Schematic of a field-structured chemiresistor (above) illustrates the conductive, structured particle network bridging the electrodes. Note the intimate contact of the particles when the FSCR is in an unstrained state. **(b)** An optical micrograph of a field-structured chemiresistor cured in a uniaxial magnetic field. The Au-coated nickel particles form a conductive, chain-like network that bridges the electrodes. The chain-like structure is readily discerned because of the relatively low particle concentration (7 vol.%). The outer diameter of this large, prototype FSCR is 12.0 mm and the electrode gap is 2.4 mm. **(c)** An array of six 4.5 × 2.0 mm FSCRs (U.S. penny for scale).

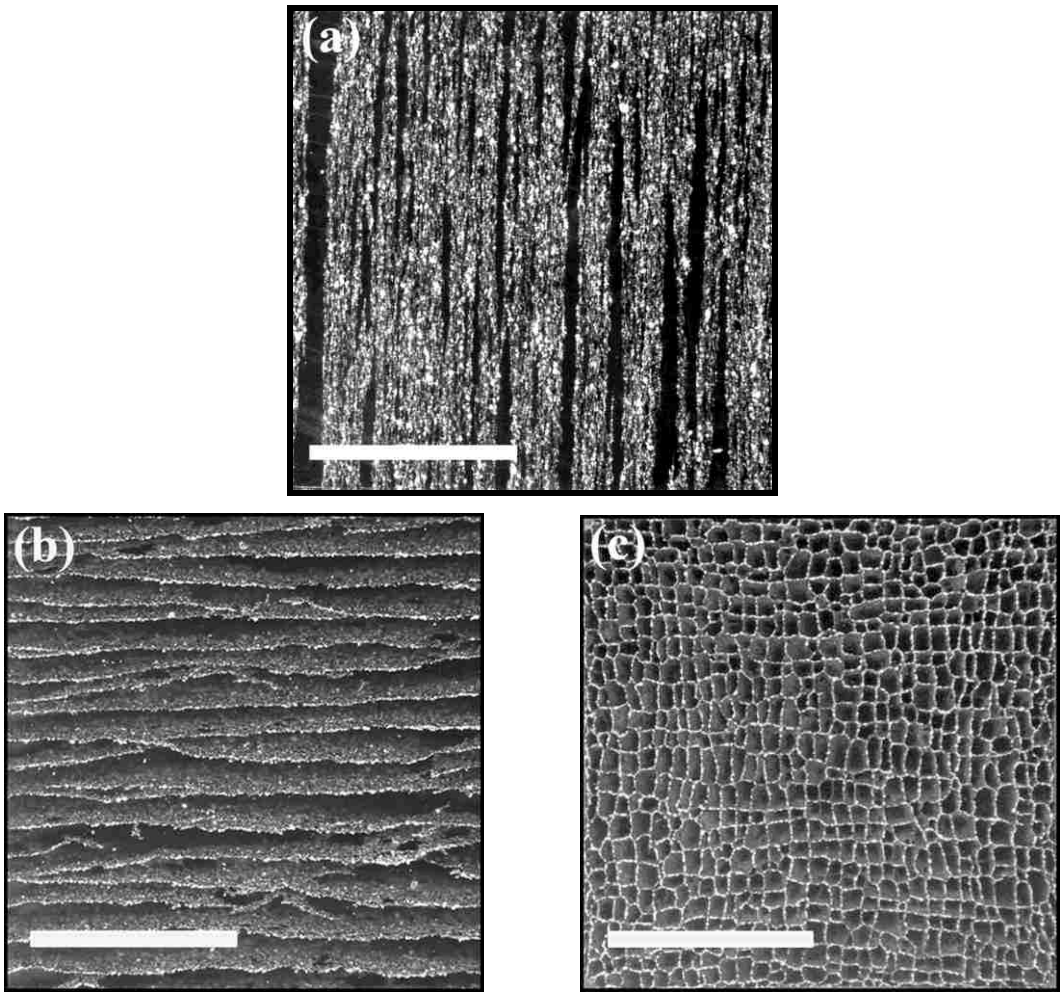

Figure 3-2. Optical micrographs illustrate how simple uniaxial or multi-axial magnetic fields can be used to create a variety of particle composites. **(a)** A uniaxial magnetic field leads to a low-dimensionality chain-like particle network. **(b)** A biaxial field, created by two orthogonal ac magnetic fields of different frequencies, leads to particle sheet formation. **(c)** A triaxial field, created by three orthogonal ac magnetic fields of different frequencies, can lead to more complex structures, such as the cellular particle network shown here. The white scale bar is 3 mm. The synthesis of these materials is reported by Martin et al.[35–39]

3.2. Why Structure the Composite?

In order to have a reasonable response (relative resistance change), a chemiresistor composite employing a random particle network, like those of CBCRs, must be formed slightly above the *percolation threshold*. This is the volume fraction of particles needed to *just* create conducting pathways between the electrodes. Particle clumping makes consistently achieving this condition surprisingly difficult, with the result that the sensor-to-sensor resistance variation is often a factor of 10,000. Second, CBCR responses are small—typically in the range of 10–20 % even for high concentrations of analyte vapors.

FSCRs do not rely on volume-fraction-dependent percolation, but are instead "artificially" forced to the percolation threshold. Such defined and controllable structures allow us to reproduce the initial device resistance and response to analytes to well within 10 %. This reproducibility enables us to examine the key factors that affect response—as well as the ones that don't. Most significant is the extremely large response these sensors have to even trace amounts of chemical vapors as we show in the following sections.[33] An additional feature is the use of magnetic fields to dynamically control sensor response, due to the strong magnetoresistance of field-structured composites, as we will discuss in Chapter 9.

3.3. How does an FSCR Work?

As discussed in the previous section, a uniaxial field causes the particles to form anisotropic chains that conduct charge from one electrode to the other. Current can pass through a chain of particles only if each particle is in electrical contact with its neighbors, so charge conduction through chain-like structures is inherently strain sensitive. When

an FSCR is exposed to chemical vapors, the elastomer swells due to the absorption of these vapors into the polymer matrix. This swelling-induced isotropic strain causes the encapsulated particle network to pull apart, breaking conductive pathways and diminishing inter-particle contact pressure (thereby increasing contact resistance) as shown below in Figure 3-3a. This small strain (uniaxial strain of 300 ppm or more) results in a measurable change in the net resistance of the composite, which is related to the concentration of analyte in the environment. The low dimensionality of particle network structures contributes to the extreme responses of these sensors, as typified by the fully reversible 8-decade resistance increase shown below in Figure 3-3b for a sensor exposed to 17 μg/mL *p*-xylene vapors. In fact, with a very sensitive sensor we developed, we have measured a fully reversible, 9-decade resistance increase at a *p*-xylene concentration of 1 μg/mL and have detected toluene concentrations as low as 0.05 μg/mL (13 ppm). At lower analyte concentrations the response becomes progressively smaller, but the detailed dependence of the steady-state resistance on the analyte concentration is unique for these devices, as we will discuss in the following section.

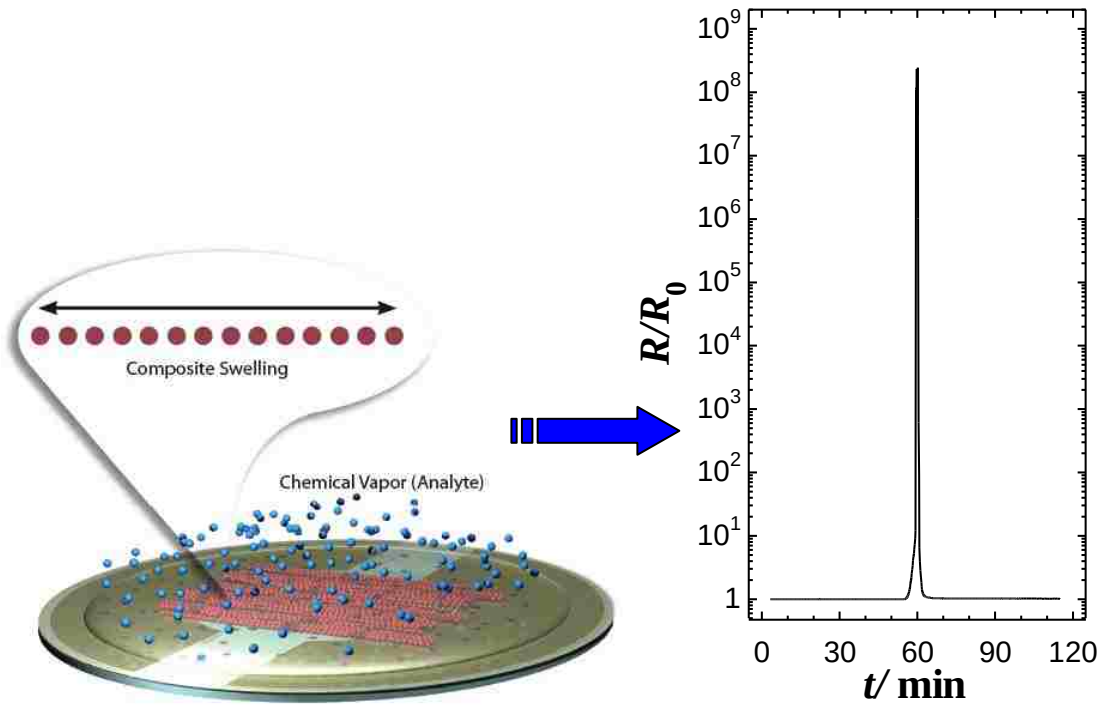

Figure 3-3. **(a)** FSCR operation schematic showing analyte absorption and composite swelling. **(b)** The composite swelling results in an extreme response of the FSCR to 17 μg/mL *p*-xylene. The sensor resistance, *R*, increases by 300,000,000 over its initial value, R_0.

3.4. Characterization of FSCR Response

Many detectors have a linear, or proportional, relationship between the analyte concentration and the equilibrium response. FSCRs have a super-linear relationship that makes them behave more like chemical switches, changing from charge conductors to insulators over a narrow range of analyte concentration. Before introducing the equilibrium (steady-state) response of these sensors, we will discuss the form of FSCR response kinetics.

3.4.1. FSCR TIME-DEPENDENT RESPONSE

Typical kinetic response of an FSCR to a step increase in analyte concentration is shown in Figure 3-4 below. From the baseline conductance, G_0, there is a quasi-exponential decrease in conductance as the analyte diffuses into the composite. The conductance then levels off to some value, G, as the concentration of analyte in the polymer reaches steady-state. This is the point at which thermodynamic equilibrium between the vapor-phase analyte and the analyte in solution with the polymer is reached (discussed in detail in Chapter 10). When the flowcell is purged with pure nitrogen, the analyte desorbs and the conductance increases on the same time scale until the baseline conductance is recovered.

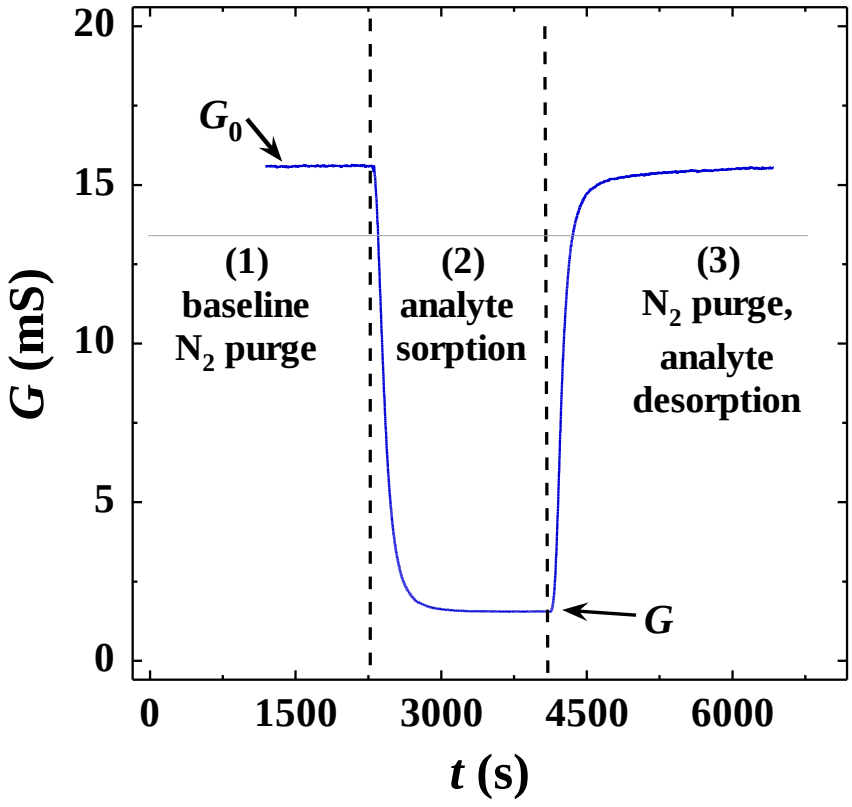

Figure 3-4. Response of an FSCR to a 2000 s exposure of 0.84 μg/mL *p*-xylene. The conductance drops quasi-exponentially, then recovers on the same timescale during the nitrogen purge.

3.4.2. FSCR EQUILIBRIUM RESPONSE: CHEMICAL SWITCH BEHAVIOR

In Figure 2-12a the relative steady-state resistance change $(R-R_0)/R_0$ of a typical sensor is shown as a function of the *p*-xylene concentration. The straight line on logarithmic axes shows that this resistance response is exponential in analyte concentration. From this observed exponential resistance increase the general form of this curve is

$$(R - R_0) / R_0 = (e^{\Gamma C / C_{1/2}} - 1) / (e^{\Gamma} - 1) \qquad \textbf{(3-1)}$$

When these same data are plotted as the steady-state conductance ratio $G/G_0 = R_0/R$, as shown in Figure 3-5b, the result is a sigmoidal curve. This figure clearly illustrates how the sensor transitions from a conductive to an insulating state over a narrow range of concentration to the extent that these sensors behave like chemical switches. From Eq. 3-1 the form of this curve is

$$\frac{G}{G_0} = \left[1 + \frac{e^{\Gamma C / C_{1/2}} - 1}{e^{\Gamma} - 1}\right]^{-1}, \qquad \textbf{(3-2)}$$

Where Γ is a fitting parameter whose value (typically 2–5) is determined by the abruptness of the conductor-insulator transition . $C_{1/2}$ is the response midpoint, which is defined as the analyte concentration that reduces G_0 by half. The sensor in Figure 3-5 has a response midpoint of ~4 and although the response is large, it occurs over a narrow analyte concentration range, from roughly 0.5 to 7.5 μg/mL. In Chapter 8 we show how

this switch-like response enables the synthesis of homogeneous FSCR arrays that have high sensitivity over a wide concentration range.

The super-linear increase of the sensor resistance is due to the swelling of the polymer, so one might attribute this super-linear response to a super-linear dependence of the swelling on analyte concentration. In fact as we will show in Chapter 10, swelling is linearly dependent on analyte concentration. It is therefore the transduction mechanism itself that transforms this fundamentally linear response into the exponential behavior we observe. One possible explanation is that the contact resistance between particles has an exponential dependence on swelling. This suggests quantum-mechanical tunneling as a mechanism of charge conduction, since tunneling currents are exponential in particle gap.

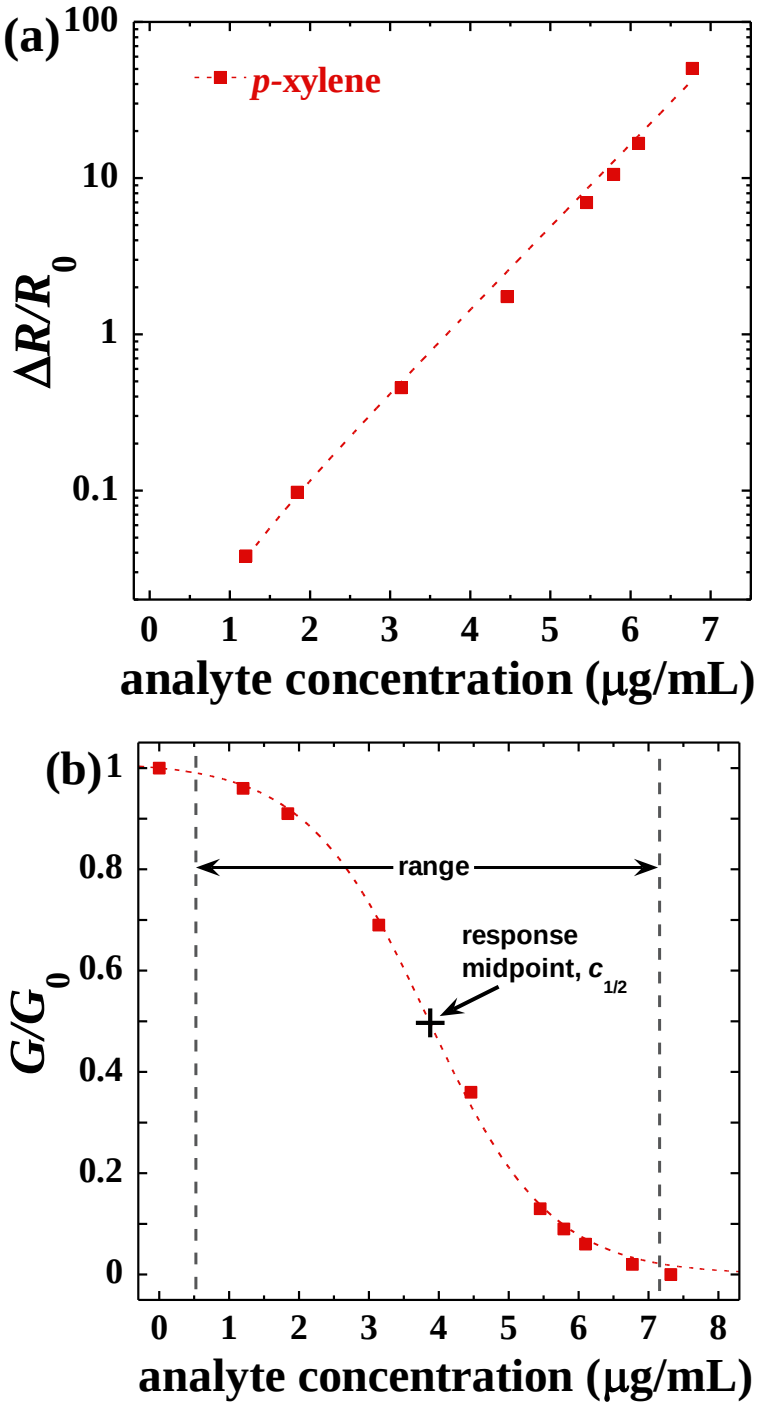

Figure 3-5. **(a)** The steady-state response of a typical 15 vol.% particle-phase chemiresistor is exponential in xylene concentration. Here ΔR is the resistance change, $R-R_0$. **(b)** The relative conductance G/G_0 is sigmoidal in shape when plotted against analyte concentration. Plotting the data in this form illustrates the chemical-switch nature of FSCRs as the composite goes from a conductive to an insulating state over a narrow range of concentration.

3.5. Selectivity and Concentration Versus Activity

Now that the form of response curve has been introduced, we can revisit the artificial nose concept (Section 2.3.2) as it relates to FSCRs. Flory-Huggins theory predicts that polymer swelling is determined both by analyte chemical affinity and volatility. The sorption isotherm is given by the Flory-Huggins equation[40–42]

$$\ln\left(\frac{p}{p^*}\right) \equiv \ln a = \ln\phi + (1-\phi) + \chi(1-\phi)^2, \qquad \textbf{(3-3)}$$

where p is the partial pressure of the analyte, p^* is the saturation vapor pressure, $a \equiv p/p^*$ is the analyte *activity*, ϕ is the volume fraction of absorbed analyte in the polymer, and χ is the Flory parameter, which is a measure of the polymer-analyte interaction energy. Because analyte activity is independent of the chemical nature of the polymer, variations in the χ parameter alone are the basis for *differential* response in selective polymer-sensor hetero-arrays (artificial noses), whereas the analyte saturation vapor pressure merely determines the response amplitude.

Flory-Huggins theory predicts that at fixed analyte partial pressure the swelling is greater for analytes with lower saturation vapor pressure, provided they are chemically similar. To demonstrate this, we tested the homologous series toluene, xylene, and mesitylene (phenyl rings substituted with 1, 2 and 3 methyl groups, respectively). These have similar χ values, but at room temperature mesitylene has about one-third the saturation vapor pressure of xylene, which in turn has about one-third that of toluene as

seen in Figure 3-6 and Table 3-1 below. At fixed analyte concentration, mesitylene should give the greatest response.

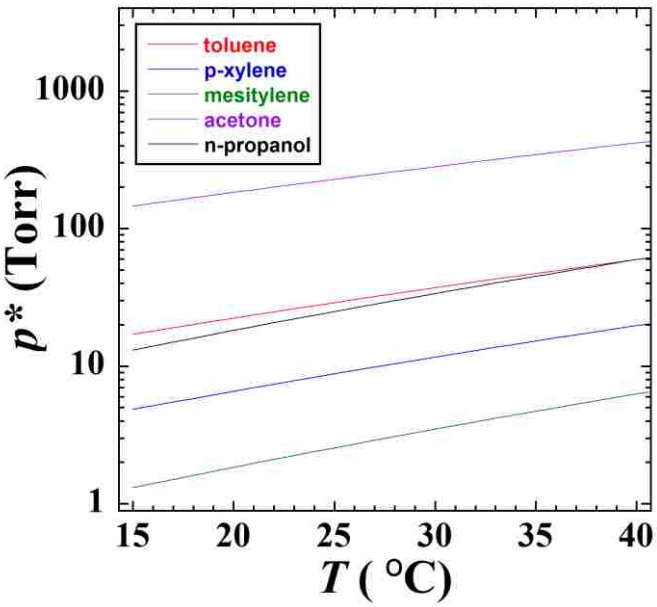

Figure 3-6. Vapor pressure curves for various analytes calculated from the Antoine equation, the constants for which are given in the table below.

analyte	*A*	*B*	*C*	*p** at 25 °C (Torr)
Toluene	7.1362	1457.29	231.827	28.97
p-xylene	7.15471	1553.95	225.23	8.80
mesitylene	7.26105	1695.83	222.415	2.55
acetone	7.31414	1315.67	240.479	228.19
n-propanol	7.77374	1518.16	213.076	24.94

Table 3-1. Room temperature saturation vapor pressures and Antoine coefficients for the analytes,[43] where $\log_{10}(p^*) = A - B/[T(^\circ C) + C]$.

A comparison of the steady-state responses of a silicone-based FSCR to these analytes is in Figure 3-7a. The response midpoints are 0.3, 1.0, and 2.5 μg/mL for mesitylene, xylene, and toluene, respectively, demonstrating that sensitivity does indeed increase inversely to volatility. In fact, a mesitylene concentration as low as 15 ng/mL is easily detected, which is far below what we can smell. At this concentration only one of every 330,000 molecules in air is mesitylene.

In a chemical spill of a particular size, the concentration of an analyte in the nearby air will increase in proportion to its volatility. In other words, one can expect chemicals to present themselves to a proximal sensor at roughly constant activity, not concentration. In equivalent spills of toluene and mesitylene, the toluene concentration will therefore be higher. Under these circumstances, the relative FSCR response is solely due to chemical affinity. To illustrate the importance of polymer-analyte chemical affinity, we measured the response of the same silicone FSCR to acetone and *n*-propanol in terms of activity instead of concentration, with the results in Figure 3-7b. This sensor is much less sensitive to these hydrophilic analytes than to the hydrophobic analytes. Propanol has much lower affinity for silicone than acetone since PDMS is hydrophobic and propanol is more hydrophilic than acetone. In fact, saturated water vapors give no measurable response at all, so this silicone-based sensor would be useful for environmental monitoring where moisture is present.

It is also noteworthy that the response data for mesitylene, xylene and toluene almost form a single curve on the activity plot. This occurs because plotting against this variable removes the effect of volatility from the response of these chemically similar analytes. Is there a response plot that also removes the effect of chemical affinity? If so,

then all response data would make a single *master transduction curve* that would be a characteristic of the individual sensor itself, with the important practical consequence that a sensor could be calibrated once and for all with just a single analyte. This will be the subject of Chapter 10.

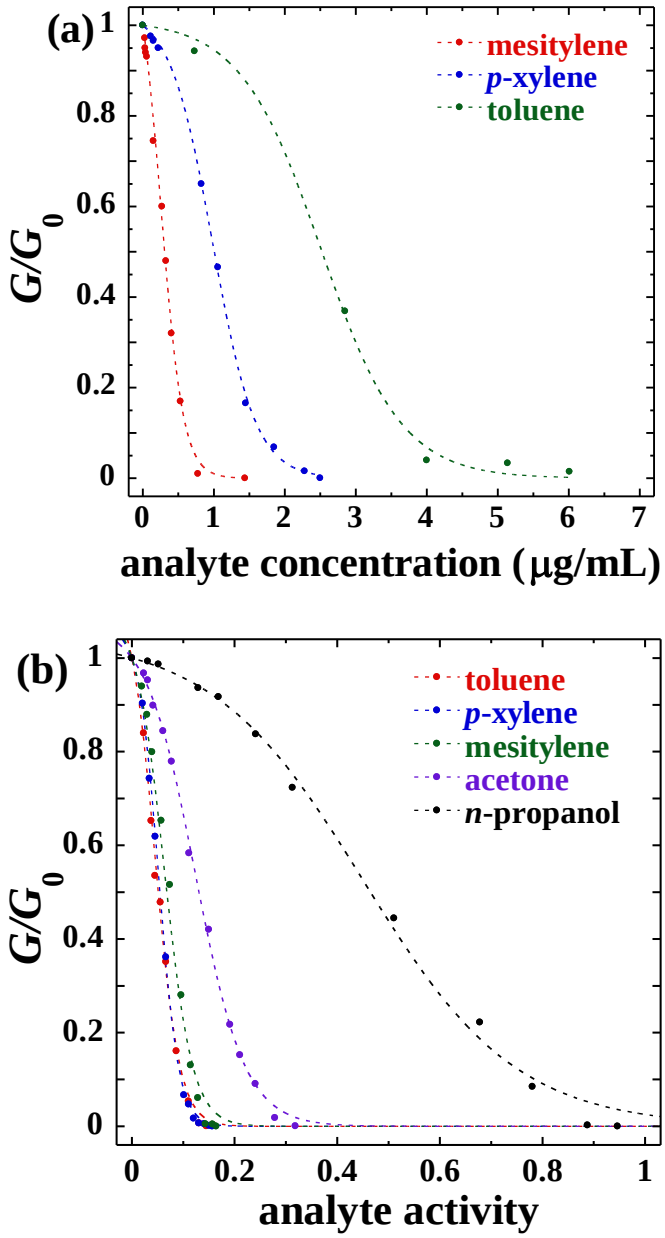

Figure 3-7. **(a)** The steady-state response of a field-structured chemiresistor to the homologous series toluene, xylene, mesitylene shows the expected sensitivity increase with decreasing volatility. **(b)** A plot of response data as a function of analyte activity eliminates the effect of analyte volatility. Differences in response are solely due to differences in chemical affinity. Much lower sensitivity is observed for hydrophilic analytes, such as *n*-propanol, whereas the response data for the homologous aromatic analytes now form a single, high-sensitivity curve.

3.6. FSCRs and Carbon-Black Chemiresistors: A Comparison

In this chapter we have touted the advanced capabilities of FSCRs, so it is fitting that we conclude with a direct comparison of FSCRs to traditional carbon black chemiresistors (CBCRs). The CBCR data used for this comparison are those reported in the 2003 SAND Report: SAND2003-3410, *Chemiresistor Microsensors for In-Situ Monitoring of Volitile Organic Compounds: Final LDRD Report*.[44]

The following Figure 3-8 is a direct comparison of a high-sensitivity CBCR and an FSCR. It should be noted that the poly(ethylene-vinylacetate) (PEVA) CBCR represents the most sensitive sensor reported in Fig.48 of Ref. 44,. Figure 3-8 shows that the CBCR has achieved a response of only ~3 % whereas at the same xylene concentration the FSCR has reached its response midpoint. The FSCR has *completely* switched off at the concentration where the CBCR has reached a ~10 % response. It is apparent from this comparison that field-structured chemiresistors represent an *extreme* advance in chemiresistor technology. In addition to increased sensitivity, many other issues plaguing traditional chemiresistor technologies have been addressed by FSCRs. FSCRs have complete reversibility, increased sensor-to-sensor reproducibility, increased base-line stability, chemical switch capability, and complete control and tunability of sensitivity (as we will detail in subsequent chapters). Chemiresistors in general have been the focus of a great deal of work over last two decades, and as such, many technological advances have been made in support of these sensors. This chemiresistor infrastructure includes sensor packaging, advanced electrodes and circuitry, microdot printing, selective polymers and membranes, array algorithms, and analyte

preconcentrators. Field-structured chemiresistors can be seamlessly integrated with these existing technologies, further expanding their utility.

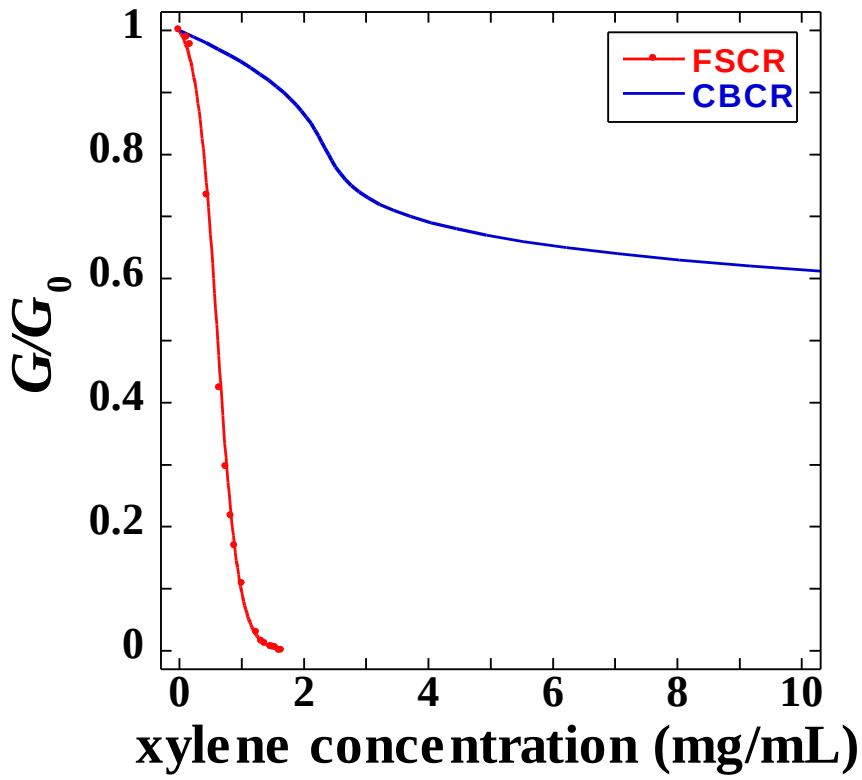

Figure 3-8. The comparison of the response of an FSCR to that of a particularly sensitive CBCR exposed to xylene illustrates the advantage of the structured composite for VOC sensing. The CBCR has only achieved a ~3 % response at the concentration at which the FSCR has reached its response midpoint. The FSCR has *completely* switched off at the point where the CBCR has reached a ~10 % response. The FSCR is composed of 15 vol.% gold-plated nickel particles structured in a uniaxial field and encapsulated in a PDMS elastomer cured at 25°C. The CBCR curve represents the fit to the data reported by Ho *et al* for a PEVA CBCR in fig.48, p.63 of SAND2003-3410.[44]

4. GENERAL EXPERIMENTAL METHODOLOGY

This chapter details the materials and methodology used to fabricate and characterize *typical* field-structured chemiresistors. Deviations from these methods are discussed on a case-by-case basis in the respective section.

4.1. FSCR Fabrication and Materials

To form the chemiresistor composite, the particles are mixed at the desired volume fraction with the uncured polymer precursor and aligned into connective networks by means of a magnetic field. Upon gelation of the encapsulating polymer, the particles become permanently structured in this orientation. When the elastomer is in an unstrained state the particles are in intimate contact with one another forming electrically conductive pathways between two electrodes on an insulating substrate (typically glass). This intimate particle contact is enhanced by compressive cure stresses within the polymer. In the following, we detail the general methodology and materials for the synthesis of typical FSCRs as well as the methodology used for sensor characterization.

4.1.1. PARTICLE PHASE

Typically, FSCRs are made with 3–7 μm spherical-agglomerate carbonyl nickel particles manufactured by Goodfellow Inc. (Part# NI006021). The morphology of these particles, which is a popcorn-like spherical agglomerate, was determined by SEM and the image is shown in Figure 4-1 below. The nickel particles are made to be electrically conductive by electrolessly plating the particles with gold. Details of this plating process can be found in Appendix E.1.

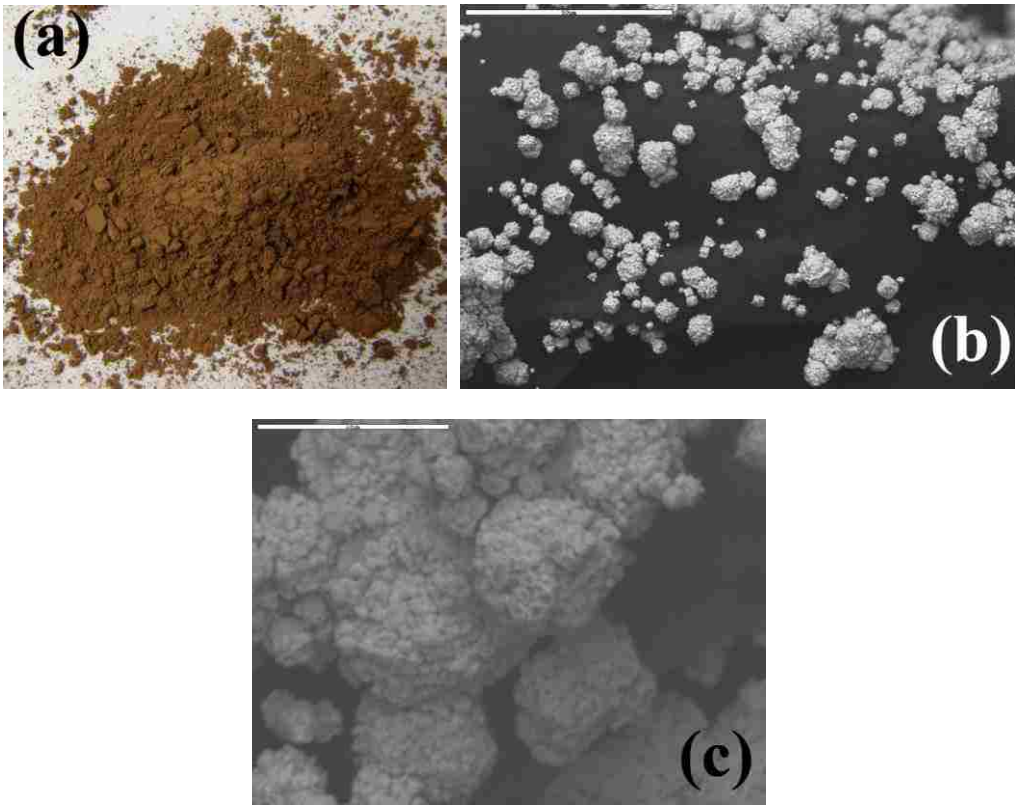

Figure 4-1. Images of gold-plated 3-7 μm carbonyl nickel particles. (**a)** The bulk powder has the appearance of ground cinnamon. (**b)** and **(c)** SEM images show spherical-agglomerate (popcorn-like) morphology of the coated particles. The scale bars are 50 and 5 μm respectively.

4.1.2. POLYMER PHASE

The model polymer used in this research is a two-part silicone, vinyl-terminated (Pt catalyzed) poly(dimethylsiloxane) (PDMS) and a vinyl modified q-silica resin (Gelest Inc. Optical Encapsulant 41). Figure 4-2 shows the reaction and resulting structure of the PDMS. Additional platinum catalyst (Pt-divinyl tetramethyl-disiloxane, Gelest part #: SIP6831) can be added to the crosslinker to decrease the cure time of the polymer system, which is especially useful for decreased cure temperatures. A plot of the dependence of cure time on catalyst concentration is in Appendix E.2. The effect of cure temperature on FSCR response is discussed in Chapter 8.

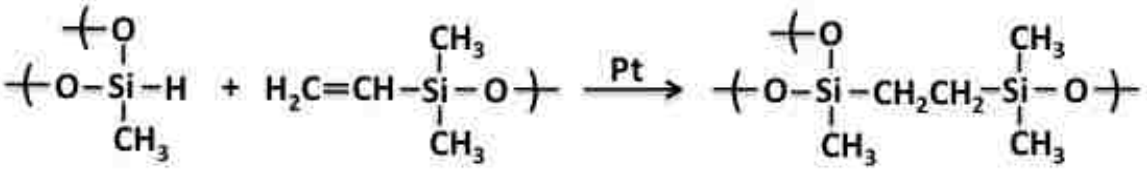

Figure 4-2. The addition-cure silicone used in this research is the product of a methylhydrosiloxane crosslinker (far left) and a vinyl-terminated PDMS resin with a platinum catalyst.

4.1.3. FABRICATION OF THE COMPOSITE PRECURSOR

FSCRs are fabricated by mixing the silicone precursors, parts A and B, by equal mass and stirring in the desired volume fraction of nickel particles (typically 15 vol.%). The uncured composite can be solvent cast with 50–100 vol.% hexane (with respect to polymer phase only) for increased response time. 5 μL of this precursor suspension is pipetted onto a glass substrate yielding a nominally 200 μm thick, 3mm diameter composite, which spans the two patterned gold electrodes (a typical electrode gap is 1–2 mm). The composite is then placed in a magnetic field and cured. After curing is complete, the sensor is removed from the magnetic field and allowed to cool. The latest generation sensor is shown in Figure 4-3 below. Before sensor response is tested, the sensor is exercised by exposing it to analyte vapors at a concentration sufficiently high to make the sensor non-conductive and then allowing the sensor to fully recover. A step-by-step description of this procedure is found in Appendix E.2.

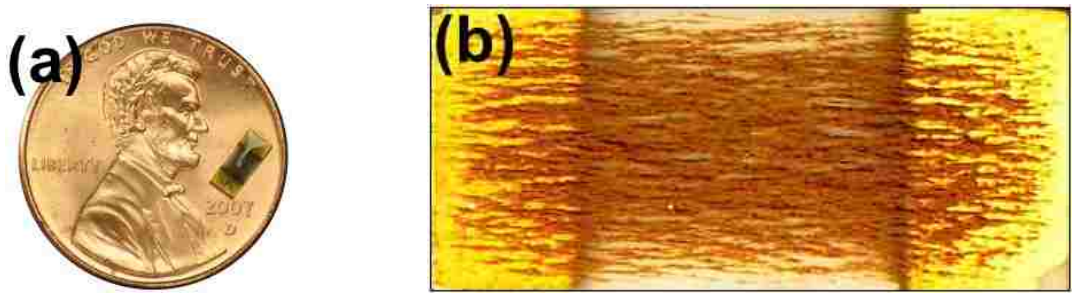

Figure 4-3. **(a)** An example of the latest generation of FSCRs on U.S. penny for scale. **(b)** A magnified view of this same sensor illustrates the PDMS-encapsulated, chain-like particle network, which bridges the ~2 mm electrode gap. The particles are 3–7 μm Au-coated carbonyl Ni.

4.1.4. FIELD-STRUCTURING PARTICLE NETWORKS

Particle structuring is what facilitates the unique and optimized chemical sensing characteristics of an FSCR. In this section we discuss the typical use of a uniaxial magnetic field for structuring particle networks. The use of this field results in an anisotropic chain-like, particle-network structure for the case of spherical and rod-like particles as shown in the previous Figures 4-3, 3-1b and 3-2a.

After the viscous composite precursor is deposited onto the substrate, the sensor is positioned between two parallel, 2.5×10.2×15.2 cm ceramic rare-earth magnets (obtained from Master Magnetics, Inc., part #: CB185CMAG). The magnets are separated by 5 cm, which results in a ~750 gauss uniform magnetic field. It should be noted that the sensor is placed in the top plane of the magnets in order to be subjected to a slight fringe field. This slight upward bending of the magnetic field lines in the fringe field has been found to help prevent particle settling. The chemiresistor composite is left in the magnetic field until fully cured. Figure 4-4 illustrates the typical method used for field

structuring the FSCRs. Experiments using helmholtz coils (shown in Figure 4-5 below) and permanent magnets have shown that FSCR response is independent of the field strength between 50 and 750 gauss as illustrated in Figure 4-6 below.

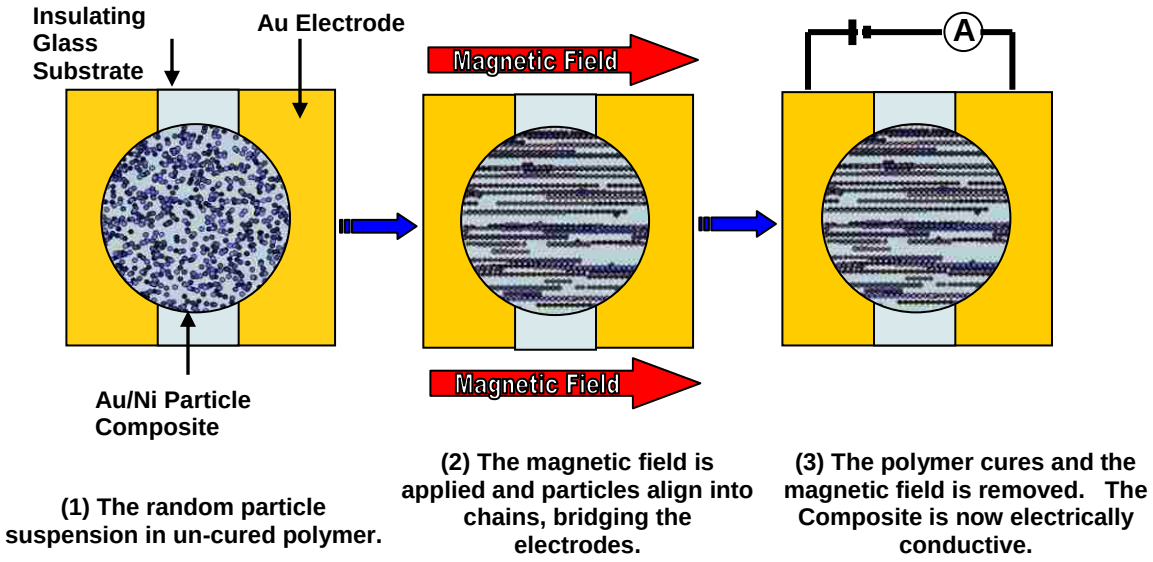

Figure 4-4. Schematic detailing the process of field-structuring the particles to form a conductive chain-like network.

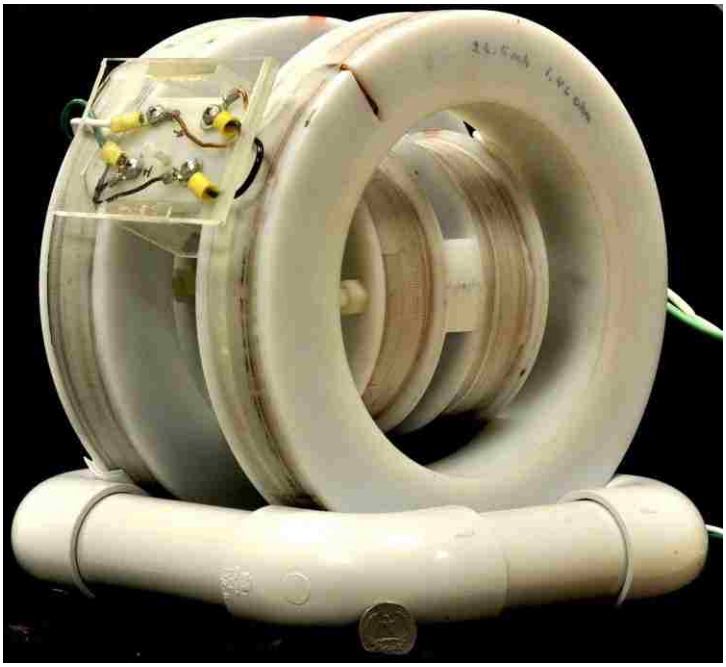

Figure 4-5. The resonate triaxial magnet system contains 3 orthogonal Helmholtz coils, which are controlled by a tunable, fractal capacitor bank. This system developed by Martin, can produce ac fields over large frequency ranges.[37,38] U.S. quarter for scale.

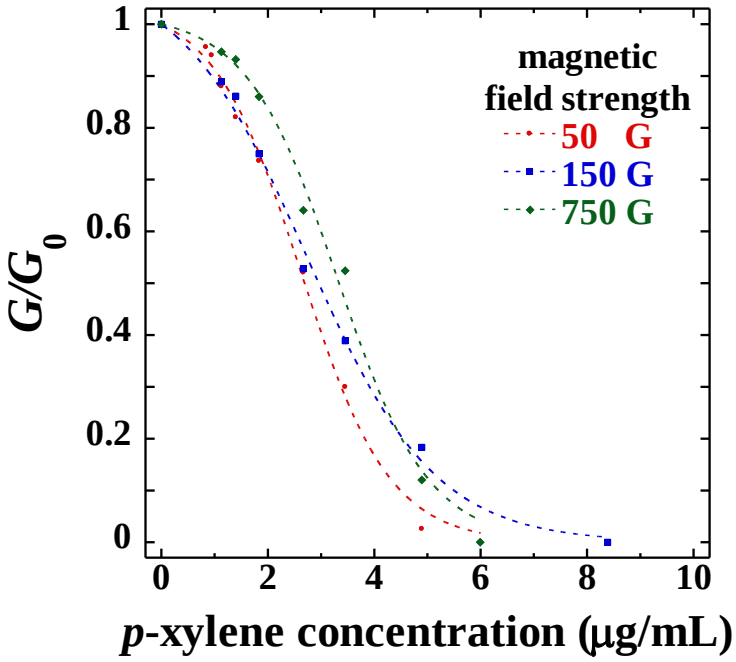

Figure 4-6. The response curves of three sensors made with varying uniaxial magnetic field strength show no discernable dependence on the magnitude of the field.

4.2. Flow Systems

This section details the apparatuses and methods used to create precisely known analyte concentrations for sensor response experiments.

4.2.1. DIFFUSION-VIAL FLOW SYSTEM

The first apparatus we will discuss relies on a temperature-controlled vial of liquid analyte as the source of analyte vapors. A schematic and pictures of this flow system are shown in Figure 4-7. This apparatus consists of a vial of analyte placed in a glass-bead-packed U-tube, which is submerged in a temperature controlled water bath. Flow from a single nitrogen source is split into two streams that are controlled with manual flow control valves and digital flow meters. The first nitrogen stream flows through the U-tube and around the vial of liquid analyte, entraining analyte vapors diffusing from the vial. This analyte-rich stream, kept at a constant flow rate, recombines with a controlled dilution stream to deliver the desired concentration of analyte to the sensor flowcell. The analyte concentration is accurately determined by weighing the vial of analyte before and after the experiment, and combining this mass change with the known nitrogen flow rate over a known time. The water bath temperature is used to control the rate of analyte evaporation and therefore the concentration of this analyte-rich stream.

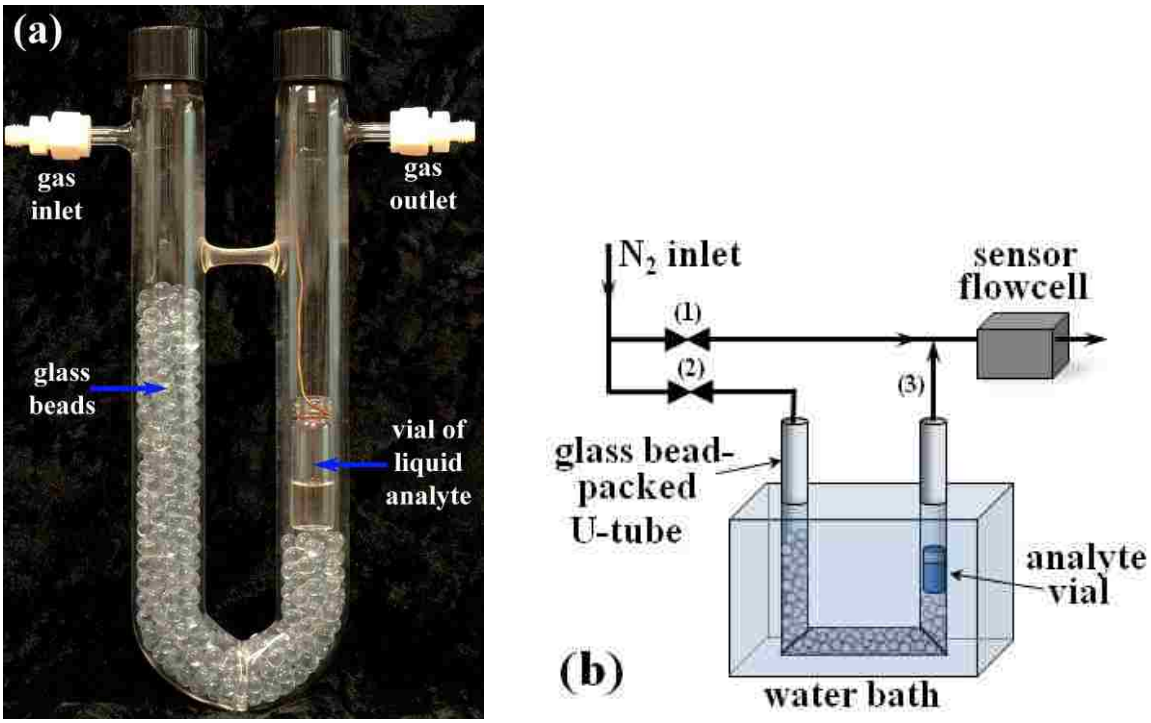

Figure 4-7. Vial system for sensor response experiments. **(a)** A picture of this flow system shows the glass-bead packed U-tube containing the vial of liquid analyte. **(b)** Schematic of the vial system, where (1) and (2) refer to the N_2 mass-flow controllers for the dilution and bubbler-inlet streams respectively. Stream (3) is the analyte-rich effluent.

4.2.2. BUBBLER FLOW SYSTEM

The second system we will discuss is a basic bubbler apparatus. A picture and a schematic of this flow system are shown in Figure 4-8. This apparatus consists of a bubbler immersed in a temperature-controlled water bath. The bubbler is fed with nitrogen from a variable 0–50 mL/min mass flow controller (MFC). The bubbler effluent is saturated with analyte vapor and joins with a nitrogen line from a 0–500 mL/min MFC. This 0–500 mL/min nitrogen line is used to dilute the analyte vapor to the desired concentration. An on/off solenoid is placed in-line after the bubbler to prevent the analyte from diffusing into the nitrogen flow when the bubbler MFC is off and the

flowcell is being purged with pure nitrogen. The concentration in the flowcell can be varied in three ways: 1) nitrogen flow rate through the bubbler; 2) dilution flow rate; and 3) bubbler temperature. The analyte concentration in the flowcell is modeled assuming that the nitrogen leaving the bubbler is fully saturated with analyte vapor. The concentration of analyte in the bubbler effluent is controlled by the water bath temperature, which is set at or below room temperature to prevent the super-saturation that can cause subsequent condensation of the analyte in the bubbler effluent tubing before it combines with the dilution flow stream. The model for the analyte bubbler is presented in Appendix C.2.

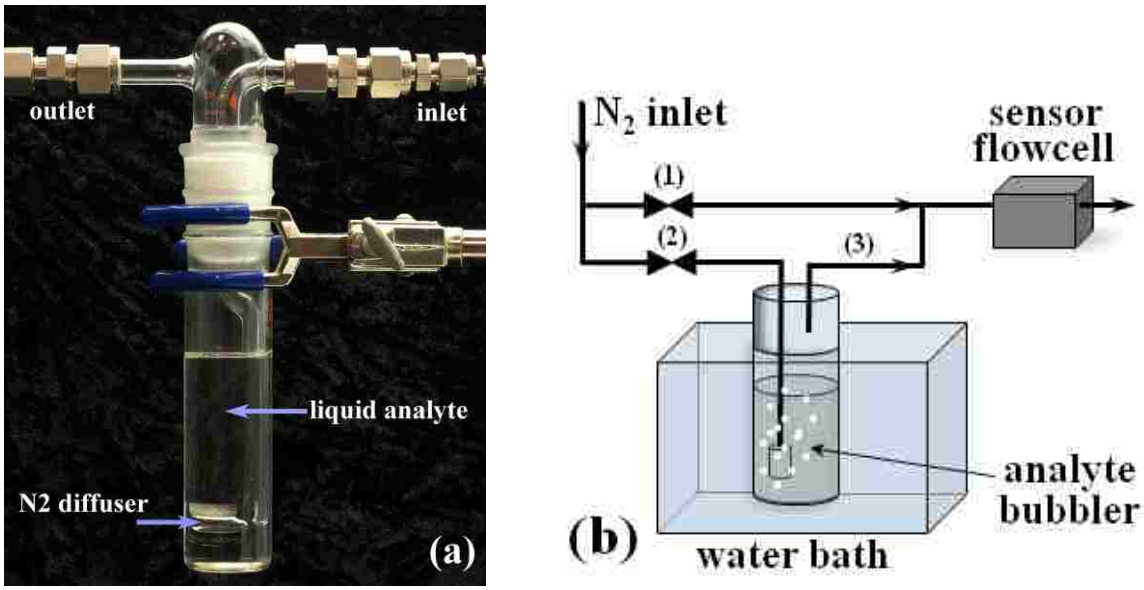

Figure 4-8. **(a)** Bubbler apparatus for analyte mass-sorption measurements. **(b)** Schematic of the bubbler system. (1) and (2) refer to the N_2 mass-flow controllers for the dilution and analyte bubbler streams respectively. Stream (3) is the analyte rich effluent.

4.2.3. BUBBLER FLOW SYSTEM CALIBRATION

The vial system was not used for all experiments because it was desired that the bubbler system be completely automated for the longer measurement (such as the mass-sortpion experiments in Chapter 10)—an impracticality with the vial system. To be able to make direct correlations between the sensor response data obtained with the vial flow system and the sorption data acquired with the bubbler flow system, the analyte concentration associated with the bubbler was calibrated to that of the vial system. To accomplish this, an extremely accurate in-house FSCR was used. Several experiments using *p*-xylene as the analyte were conducted on both systems for error analysis and the data was fit and used for the calibration yielding $a_{vial} = 1.284\, a_{bubbler}$. The multiplier of 1.284 indicates that the bubbler does not fully saturate the nitrogen stream.

4.3. Sensor Flowcell

The flowcells developed for this research have several functions: securely house the sensors, shield the sensors from electrical disturbances, maintain constant temperature, and provide the sensors with gas and electrical throughput. Figures 4-9 and 4-10 illustrate the 2nd and 3rd generation flowcells used in this research, respectively. The flowcells were designed and machined in-house. The latest (3rd) generation flowcell (Figure 4-10) holds and allows for testing an array of six sensors simultaneously. Sideways opposing pogo-pins provide electrical contact and allow for interchangeability of the sensors. Considerations were made to minimize the flowcell volume, which in turn minimizes the time required for the analyte concentration in the flowcell to reach steady-state in response to a step increase in input analyte concentration. The flowcell is

contained in an electrical shielding box, which is also filled with a large amount of solder to increase the thermal mass of flowcell environment. To reduce thermal fluctuations the shielding box is partially submerged in the same temperature controlled water bath as the analyte bubbler, which is typically kept at 20 °C. A thermocouple probe is placed in the flowcell to monitor the actual sensor temperature.

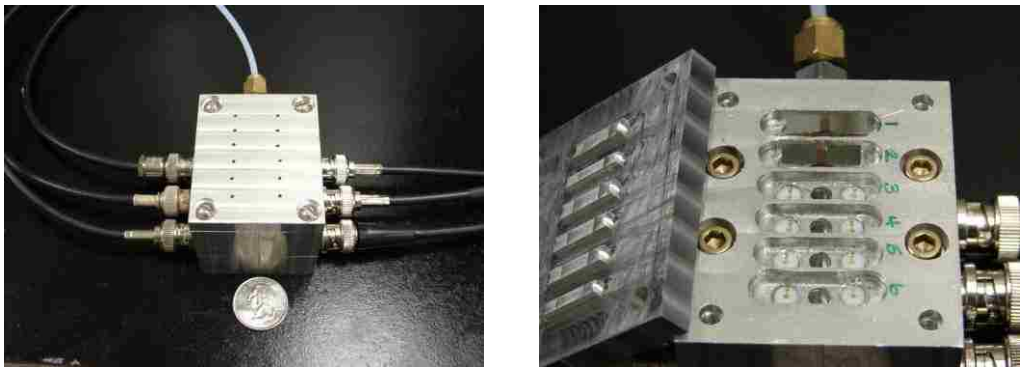

Figure 4-9. The 2nd generation flowcell houses six glass-substrate sensors pushed down against spring-loaded pogo-pins. A manifold system delivers the flow to each sensor's semi-independent chamber.

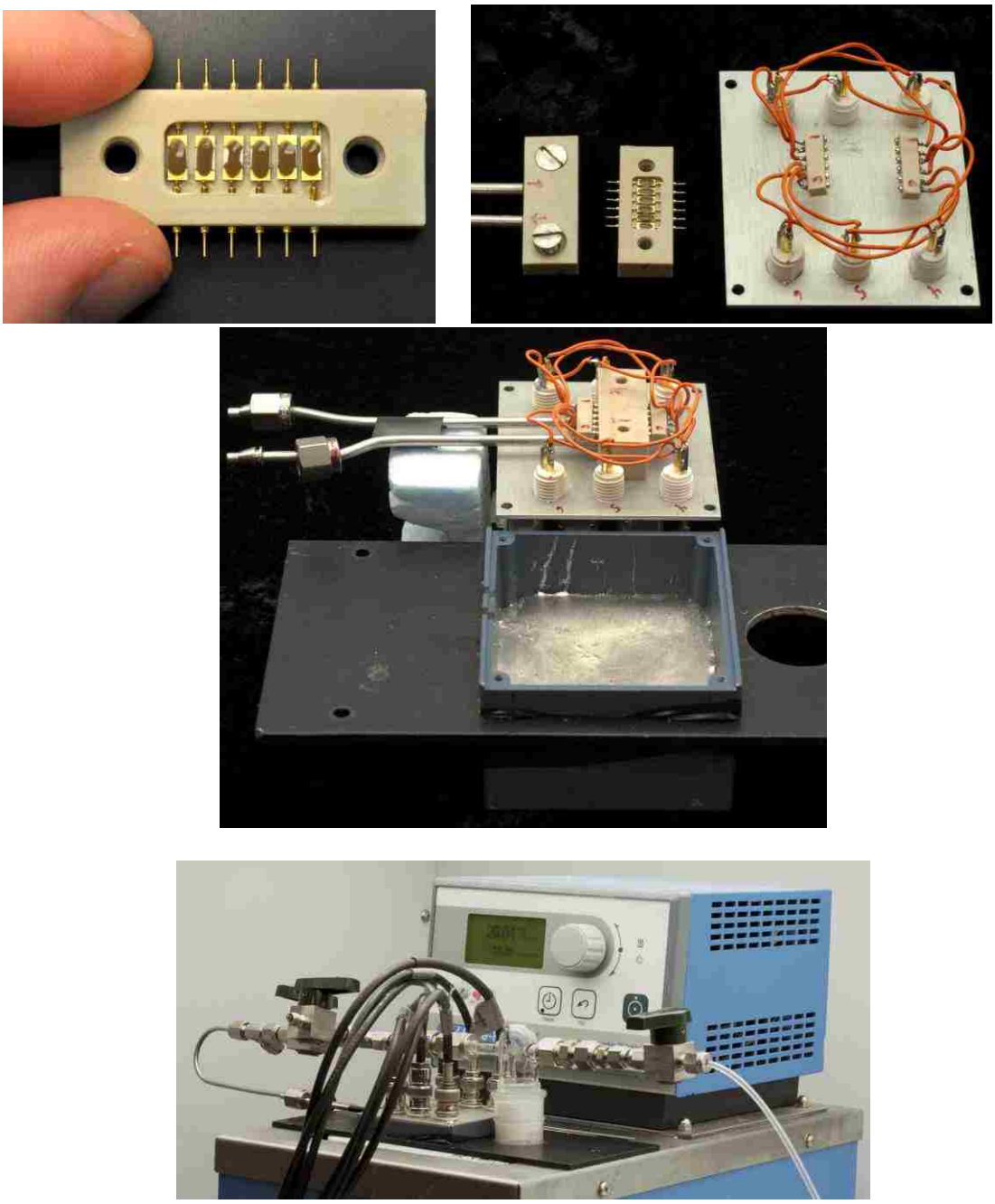

Figure 4-10. The 3rd generation flowcell **(top left)** houses six ceramic-substrate sensors held in place with opposing pogo-pins. The electrodes wrap around the substrate for contact with the pins. The flowcell snaps onto an electrical manifold for simple connectivity **(top right).** The flowcell is housed in an electrical shielding box, which contains solder for increased thermal stability **(middle)**. The entire flowcell assembly and bubbler are partially submerged in a temperature-controlled water bath **(bottom)**.

A Hewlett-Packard dc power supply (model 6552A) is used to supply 1.6 V dc to the sensor circuit. The circuit is constructed such that the single power source can be used to supply each sensor with ~10 mV, independent of the changing resistance of each other chemiresistor. During the course of the experiment the current passing through each sensor is simultaneously measured using six Keithley, Inc. picoammeters (model 6485). Figure 4-11 shows the schematic of the circuit. Kinetic data of electrical current through each FSCR from each picoammeter is graphically displayed in a LabView program and is written to a spreadsheet file.

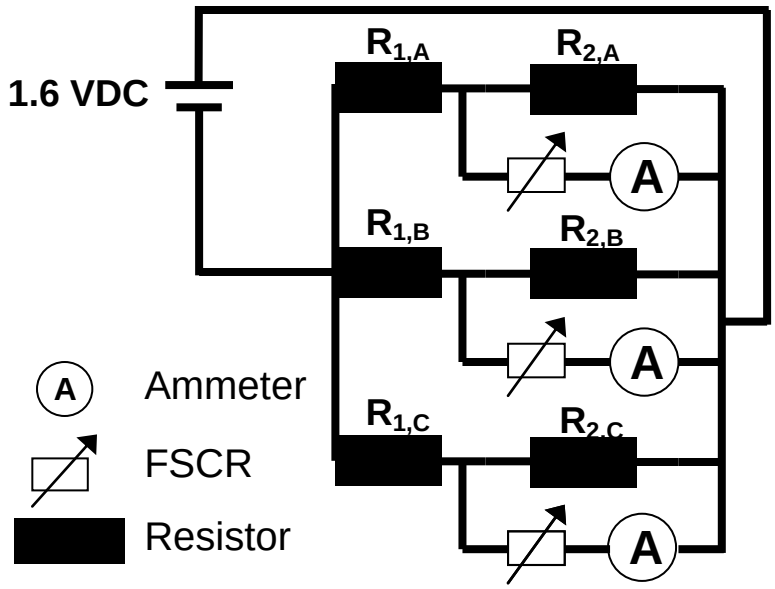

Figure 4-11. FSCR circuit schematic. Resistors R_1 are ~145 Ω and resistors R_2 are ~0.1 Ω. This circuit is designed such that the FSCRs can all be powered from the same source without their varying resistances affecting the each individual chemiresistor's supplied voltage.

4.3. Data Acquisition

Data acquisition and bubbler control for the sensor response experiments were performed with a LabView program. This program sets the desired flow rates of nitrogen and the

temperature of the water bath/bubbler, records sensor conductance, and writes the data to a spreadsheet file. The experiment is broken into three steps: baseline N_2 purge, analyte mass absorption, and final desorption purge as shown in previous Figure 3-4. The absorption and purge stages are considered to be complete when a constant conductance value achieved. The result of a typical equilibrium response cycle was shown in Figure 3-4; however, with the reversibility of the sensors proved, equilibrium response curves are determined by simply stepping up the analyte concentration for each data point until the sensor is non-conducting, at which time the flowcell is purged with nitrogen and the sensors are allowed to recover as shown in Figure 4-12 below.

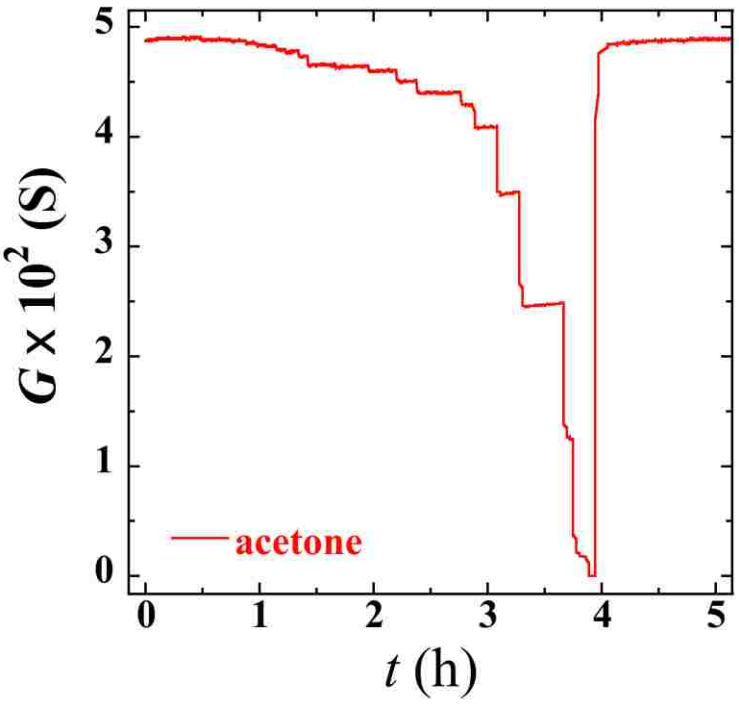

Figure 4-12. Typical kinetic data for an FSCR shows continuous step increases in analyte concentration before purging with nitrogen. Here each step is a single point on a steady-state response curve.

5. CHARGE TRANSPORT IN FSCRS

***Abstract*—**In the following we use field-structured chemiresistors to experimentally probe charge transport in field-structured composites (FSCs) and to determine how this is affected by compressive stress. We find that the bond percolation model of charge transport, which assumes that each ohmic contact between particles has either a fixed or infinite resistance, does not apply to these materials.[31,32] Rather, we adopt the point of view that all contacts have the same tunneling resistance, and that this resistance value is determined by compressive strain. This work illustrates that compressive stress in composites plays a dominant role on the composite's conductivity. In addition, other variables such as electrode gap length and varied fraction of non-conducting particles are found to affect the resistance of the composite, but have no effect on sensor response.

5.1. Evolution of Conduction in Field-Structured Composites

The percolation model is central to the current understanding of charge transport in particle composites, but there is little experimental basis for the application of this model to particle composites. The bond percolation model can be applied to charge conduction in particle composites by associating a resistor with each particle contact. In this way a composite can be thought of as a resistor network whose connectivity reflects the composite structure. If this resistor network spans the composite then the network is said to be above the percolation threshold and the composite can macroscopically transport charge. In short, in the percolation model the composite structure alone determines

charge transport, and each particle contact is assigned either some finite, similar resistance or is taken to have infinite resistance.

5.2. Electrode Gap Length Dependence

To model charge transport in FSCs, we are interested in determining the probability of a non-conducting inter-particle contact in the particle network. One such way is to determine the composite's resistance as a function of electrode gap length. In order to accomplish this, we model the structured composite as a series of parallel particle chains. We first want to know the fraction of chains in the composite that will conduct charge, P_{ch}, over a particular electrode-gap length, given a certain probability of a non-conducting, particle-particle contact, P_0. This relation is given by

$$P_{ch} = e^{-P_0 L/d}, \tag{5-1}$$

where P_{ch} is the fraction of conducting chains, P_0 is the probability of a non-conductive, inter-particle contact, L is the length of the chain (or electrode gap length), and d is the mean particle diameter, which is ~5 μm for our Au-Ni particles. The theoretical dependence of the fraction of conducting chains on chain length for various values of P_0 given by Eq. 5-1 is shown in Figure 5-1 below.

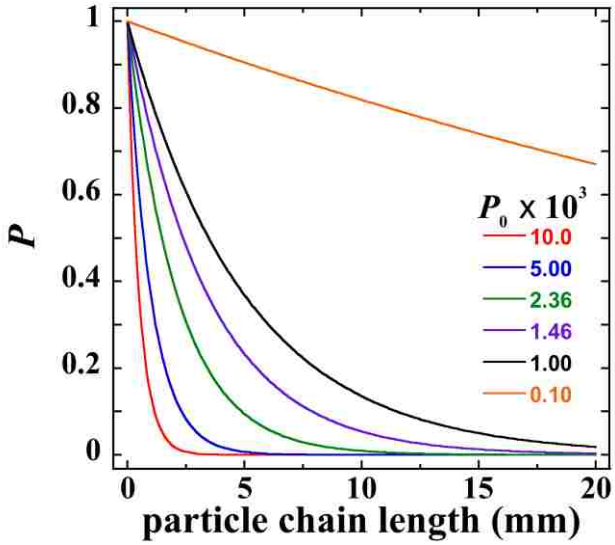

Figure 5-1. The fraction of conducting chains for varying values of the probability of a non-conducting particle contact, P_0, decreases exponentially as a function of chain length as given by the Poison distribution, Eq. 5-1. A composite with particle chains having a 1% fraction of non-conducting particle contacts is non-conducting with only a 3 mm electrode gap whereas with a P_0 of 0.1%, the composite still conducts even with a gap of ~20 mm.

We are now interested in finding how a composite's resistance depends on chain length. To do this we assume that the overall resistance of the composite is simply proportional to the total number of conducting chains. From Eq. 5-1 the expression for the composite resistance as a function of electrode-gap length is then

$$R = R_0 e^{P_0 \cdot L/d}, \qquad \textbf{(5-2)}$$

where R_0 is the resistance at the smallest electrode-gap length, which is 1 mm in this case.

To experimentally determine the value of P_0 for our field-structured composites, several sensors were made with electrode gaps varying from 1 to 10 mm. Figure 5-2a shows that, as expected, the initial resistance of these sensors, R, increases exponentially

with increasing electrode-gap length. A fit of these data to Eq. 5-2 gives a P_0 value of 1.46×10^{-3}. Therefore, from Figure 5-1, we would expect the fraction of conducting chains, and therefore the conductivity, in an actual FSC to be zero at a gap length of ~16 mm for our particular particles.

We have shown that the resistance of this composite increases with increasing electrode gap length; however, this does not affect sensor response. The response midpoint data in Figure 5-2b show that there is no dependence of sensor sensitivity on gap length by this measure. In addition, sensors were made with a constant 2 mm electrode gap with varying fractions of non-conductive Ni particles. Here the P_0 value should increase with the increasing fraction of non-conductive particles. Figure 5-3 shows the expected exponential increase in sensor resistance, however, sensor response experiments again show no effect on response. These experimental results certainly raise the question: what then *are* the important factors that affect FSCR sensitivity?

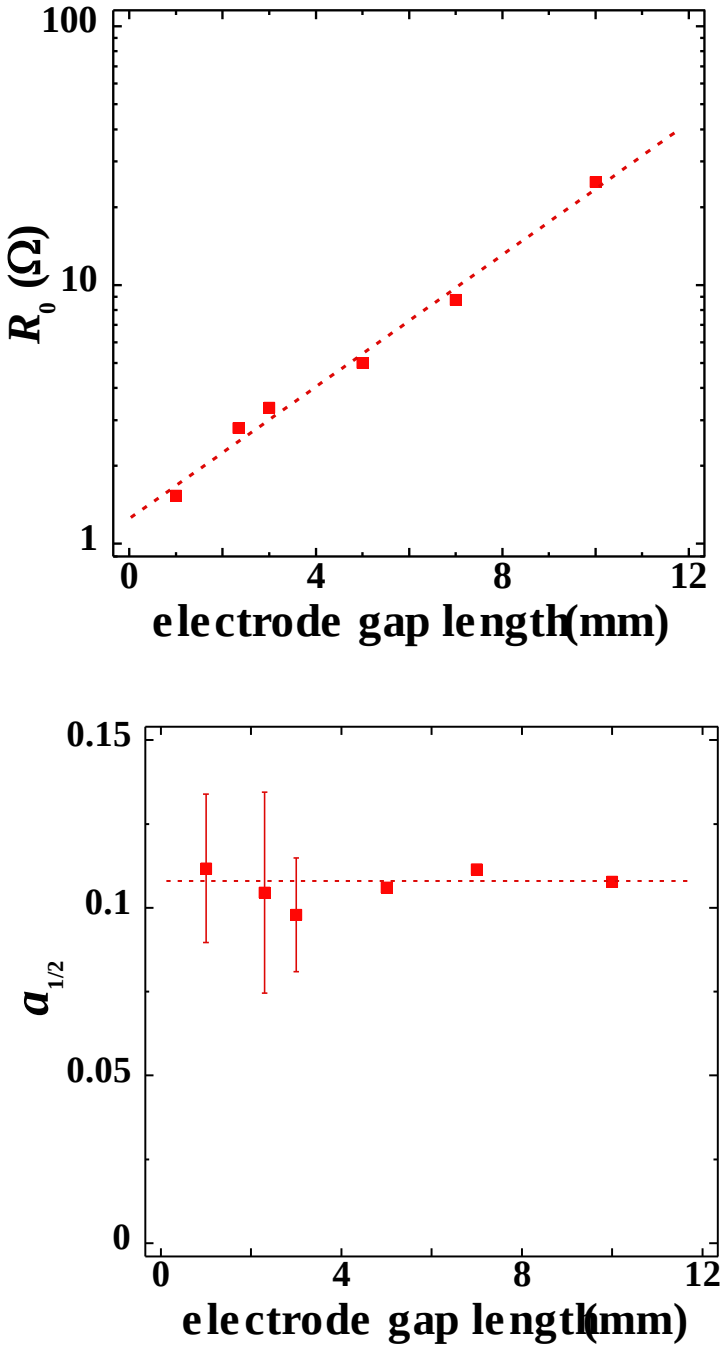

Figure 5-2. **(a)** As predicted from the Poison distrubution, the resistance of FSCRs increases exponentially with electrode gap length. A fit of these data to Eq. 5-2 gives a P_0 value of 1.46×10^{-3}. **(b)** Despite the large impact of gap length on initial resistance, there is no apparent effect on FSCR response as illustrated by the response midpoint data for *p*-xylene. The standard deviation was not calculated for the sensors with large gap length due to lack of samples.

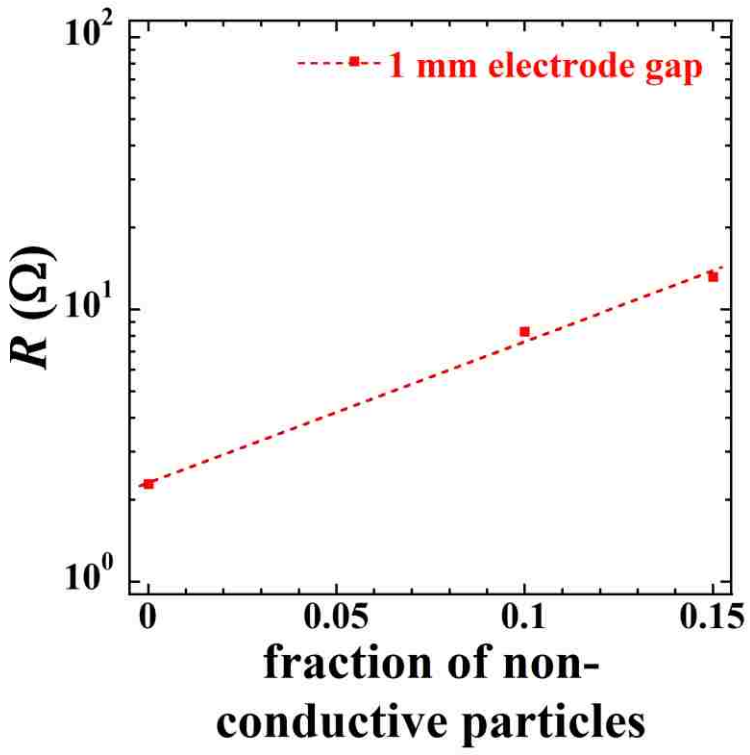

Figure 5-3. The composite resistance was determined at constant electrode gap as a function of volume fraction of non-conducting Ni particles. This plot illustrates the exponential increase in resistance, this time with increasing P_0, as expected from Eq. 5-2. Subsequent experiments, however, show that there is no effect on sensor response.

5.3. The Role of Stress on Charge Transport

Experimental work J. Martin and R. Williamson have performed shows that the polymer stress plays a dominant role in determining the composite conductivity. Figure 5-4 shows the evolution of composite conductivity during resin cure. Surprisingly, the conductivity increases 8 orders of magnitude after the gel point, even though the particles are held into contact by the applied uniaxial magnetic field. In fact, we are able to turn off the magnetic structuring field at the gel point, with absolutely no effect on the conductivity, and then observe the composite conductivity increase. Evidently, cure shrinkage causes a positive pressure on contacting particles that decreases the contact resistance and or the

inter-particle gap. We conclude that although the structure of the composite at the gel point determines the connectivity of the equivalent resistor network, it is the compressive volumetric stress that determines the resistances.

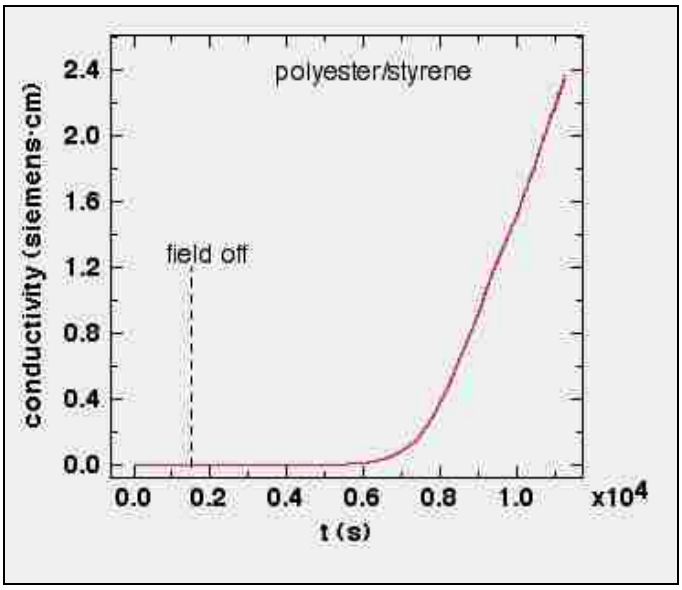

Figure 5-4. The conductivity of a field structured composite during resin cure. In this experiment the magnetic structuring field was turned off at the gel point, well before the composite showed any significant conductivity. Because the resin was gelled the particles were immobilized. As the resin cured the slight shrinkage caused the evolution of significant positive contact pressure between particles, and the composite conductivity increased 8 orders of magnitude. These data were taken by R. L. Williamson (See acknowledgements).

5.4. Does the Simple Percolation Model Apply?

The key issue in determining whether the percolation model describes charge transport in these materials is the magnitude of the resistor-to-resistor resistance variations when a strain is applied to the fully cured composite. In the percolation model either a resistor conducts with resistance R, or it doesn't conduct at all, so the resistance variations are extreme. In this view an applied strain would simply reduce the probability P_0 that a

resistor conducts. Martin et al. have developed an expression for the network resistance, which accounts for a divergence near the percolation threshold and is of the form[33]

$$R \propto \frac{1}{|P_0 - P_c|^t} \text{ for } P_0 > P_c, \quad \textbf{(5-3)}$$

where the so-called conductivity exponent, *t*, is ~2 in three dimensions. (The upper critical dimension for the percolation model—at and above which a mean field theory applies—is 6. Below this dimension the critical exponents depend on the space dimension.)

J. Martin et al. have completed carefully controlled strain experiments to determine if we can observe this critical divergence in the composite resistance, Figure 5-5 (left). These data show that the composite resistance increases exponentially with strain and then transitions to a critical divergence we cannot reliably quantify. However, Martin has developed a modified percolation model that gives this behavior as shown in Figure 5-5 (right) and is given by

$$R = R_0 + A \cdot R_0(e^{\gamma/\gamma_c} - 1). \quad \textbf{(5-4)}$$

Here γ is the strain and the constant γ_c is the characteristic strain. This model assumes that the network resistors increase exponentially with strain, and are also subject to a strain-independent *conductance variation*, A. When the strain is small the network resistances all change commensurately, because their conductance is large compared to the fixed conductance fluctuation. For large strains the conductance fluctuation becomes

comparable to the conductance of the network elements, and the system crosses over to percolation. One likely explanation for the exponential behavior is tunneling currents between the particles, which are exponential in the gap.

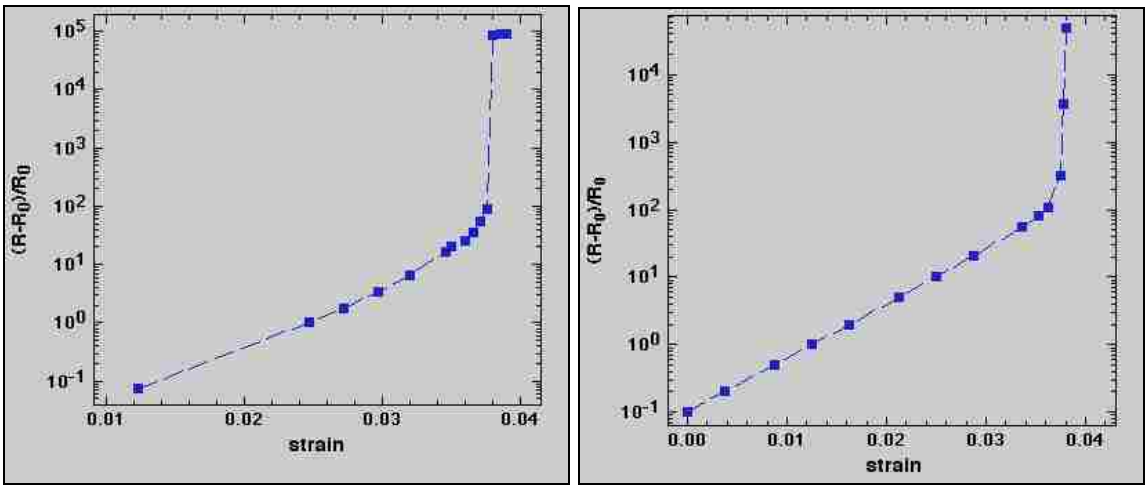

Figure 5-5. (left) The experimentally determined resistance change as a function of applied strain. (right) J. Martin's modified percolation model (Eq. 5-4) gives this behavior.

5.5. Conclusions

We have used field-structured chemiresistors to experimentally probe charge transport in field-structured composites (FSCs) and to determine how this is affected by compressive stress. This work illustrates that compressive stress in composites plays a dominant role on the composite's conductivity. We find that the bond percolation model of charge transport, which assumes that each ohmic contact between particles has either a fixed or infinite resistance, does not apply to these materials. Rather, we adopt the point of view that all contacts have the same tunneling resistance, and that this resistance value is determined by compressive strain. In the following chapters we will explore how stress also affects sensor response.

6. CONTROLLING FSCR RESPONSE THROUGH POLYMER-STRESS MANAGEMENT

***Abstract*—**In the previous chapter we offered a model and experimental data to characterize charge transport in FSCs. Despite the observed increases in composite resistance due to decreased particle-particle connectivity and increased composite length, this had no apparent effect on sensor response. Cure stress was shown to dramatically increase FSC conductance, but does *this* have an effect on response? In this chapter we develop a model for the change in sensor response as a function of stress, which *is* shown to be the dominate factor affecting sensor response. Experiments show that through volumetric stress relaxation, the response midpoint of an FSCR can be decreased by more than 6-fold. This method enables the sensitivity of a single sensor to be tuned to any desired level without a change in the polymer phase; this has never before been demonstrated for any selective polymer sensor.

6.1. INTRODUCTION

We have demonstrated through numerous experiments that the electrical conductivity of the field-structured composites we synthesize is extraordinarily sensitive to any type of strain, be it tensile, shear, or volumetric.[33] Because of this, these materials can be used to create sensors having unprecedented levels of response. Conductivity changes of 12 decades are easily observed with a volumetric swelling of just 1%. However, a plot of the conductivity versus strain is exceedingly non-linear, to the extent that these materials act as strain-induced current switches. In other words, a plot of conductivity versus strain

is sigmoidal, so that the composite has an extremely large sensitivity *only* over a narrow range of strain centered at some critical value as shown in previous Section 3.4. By understanding this behavior we should be able develop improved materials with greatly enhanced sensitivity to small strains and therefore, from the Flory-Huggins equation (Eq. 3-3), small analyte concentrations.

In the following discussion we will adopt the point of view that resistor-to-resistor variations in the contact resistances can be ignored. In other words, we will ignore the transition to percolation in the data in Figure 5-5, and will focus only on the exponential aspect of the resistivity data, which after all covers virtually the entire range of strain. In this regime the composite conductivity is controlled by the compressive stress within the composite. In the following we report on experiments intended to demonstrate how controlling this stress substantially enhances the response of these composites to small strains.

Volumetric swelling will relieve the compressive stress within a composite and can be accurately accomplished either by thermal expansion, exposing the material to a chemical vapor of known activity, or both simultaneously. Again we refer to the equation we use to model sensor response (Eq. 3-2), and by which the exponential part of the data in Figure 6-4 (left) are described:

$$\frac{G}{G_0} = \left[1 + \frac{e^{\Gamma a/a_{1/2}} - 1}{e^{\Gamma} - 1}\right]^{-1}. \qquad \textbf{(6-1)}$$

Here the response is in terms of activity instead of concentration. Recall that the fitting parameter Γ is a measure of the abruptness of the reduction of the conductivity with

increasing vapor activity and $a_{1/2}$ is the response midpoint of the sensor in terms of analyte activity. In Figure 6-1, Eq. 6-1 is plotted for a variety of values of Γ all with the same response midpoint. Typical values of Γ for our sensors are in the range of 3–7, so the conductivity changes abruptly with increased activity, and the initial sensitivity of the conductance to swelling by the vapor is low.

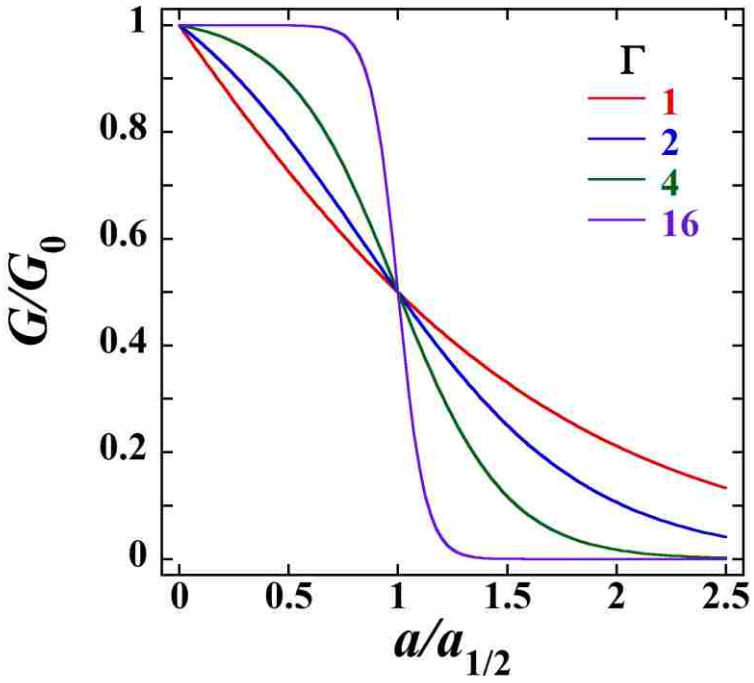

Figure 6-1. The dependence of the composite conductance on analyte activity is shown for various values of Γ.

6.2. FSCR Post-Cure Swelling Theory

If we imagine swelling the composite by exposing it to an irreversibly absorbing vapor, we hypothesize that this will alter the sensor's response to subsequent analyte exposure. To model this scenario, we renormalize the initial conductance of the sensor to that of this irreversibly swollen state. For the sake of simplicity we assume this post-cure

swelling agent has the same chemical affinity for the polymer as the analyte, that is, the same Flory parameter χ (Section 3.5). After pre-exposure to a swelling agent of activity a^*, the renormalized composite conductivity becomes

$$\frac{G}{G_0} = \left[1 + \frac{e^{\Gamma a^*/a_{1/2}} - 1}{e^{\Gamma} - 1}\right] \cdot \left[1 + \frac{e^{\Gamma (a+a^*)/a_{1/2}} - 1}{e^{\Gamma} - 1}\right]^{-1}, \qquad \textbf{(6-2)}$$

where G_0 now denotes the composite conductivity after swelling. In the limit of large post-cure swelling (large $a^*/a_{1/2}$ of the swelling agent), the magnitude of the renormalized sensor response to a given activity of the analyte is much greater, as shown in Figure 6-2. This theoretical response curve does reach a limit, however, so we expect that FSCRs have a limiting maximum sensitivity. This limiting response curve is found by taking the limit of Eq. 6-2 as $a^* \to \infty$, which gives

$$\frac{G}{G_0} = e^{-\Gamma a/a_{1/2}}. \qquad \textbf{(6-3)}$$

In this strongly swollen limit the vapor activity required to reduce the composite conductivity by half is $a_{1/2,swollen}/a_{1/2} = \ln(2)/\Gamma$, which for the typical case of $\Gamma = 4$ is 0.173. So swelling can reduce the response midpoint activity of a composite by a factor of $1/0.173 \approx 6$. In general, the response midpoint activity of the swollen sensor is given by

$$a_{1/2,swollen} = \frac{a_{1/2}}{\Gamma} \ln\left(e^{\Gamma} + 2e^{\Gamma a^*/a_{1/2}} - 2\right) - a^*, \qquad \textbf{(6-4)}$$

which is a smoothly decreasing function of the swelling agent activity, a^*.

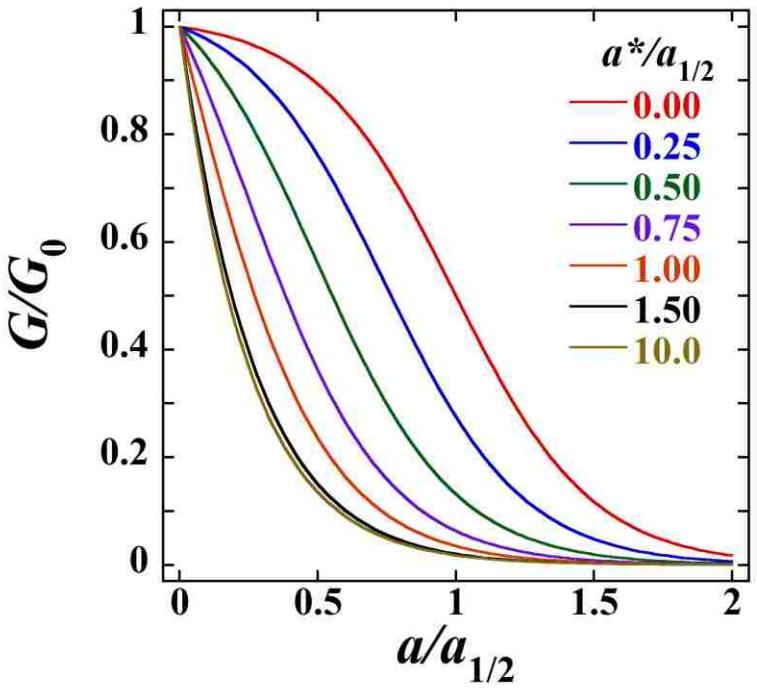

Figure 6-2. For the experimentally typical value of $\Gamma = 4$ we show the effect of post-cure swelling on the renormalized response curve. The chemical activity of the swelling agent is given in the legend, and the chemical activity of the volatile vapor is the abcissa. (recall that $a_{1/2}$ is defined as that activity which reduces the conductivity of the unswollen composite by half.)

It should be emphasized that the initial slope of the conductivity response curve is altered much more dramatically by swelling than the response midpoint, and this slope determines the sensitivity of these materials to small strains, such as those caused by very low concentrations of volatile organics. In general, it is reasonable to expect to sense a

vapor whose activity is just a few percent of the initial inverse slope. Defining $\gamma^{-1} = -\frac{1}{G_0}\frac{dG}{da}$ we obtain for the inverse initial slope

$$\gamma = \frac{a_{1/2}}{\Gamma}\frac{e^{\Gamma a^*/a_{1/2}} + e^{\Gamma} - 2}{e^{\Gamma a^*/a_{1/2}}}. \qquad \textbf{(6-5)}$$

In the absence of swelling this inverse slope is $\gamma(a^* = 0) = \frac{a_{1/2}}{\Gamma}(e^{\Gamma} - 1)$, but in the limit of large swelling this inverse slope approaches $\gamma(a^* \to \infty) = \frac{a_{1/2}}{\Gamma}$, so the sensitivity of the conductivity to small analyte-vapor activities is increased by the factor $e^{\Gamma} - 1$. For $\Gamma = 4$ this is more than a 50× sensitivity increase. The change in the initial inverse slope with swelling is shown below in Figure 6-3.

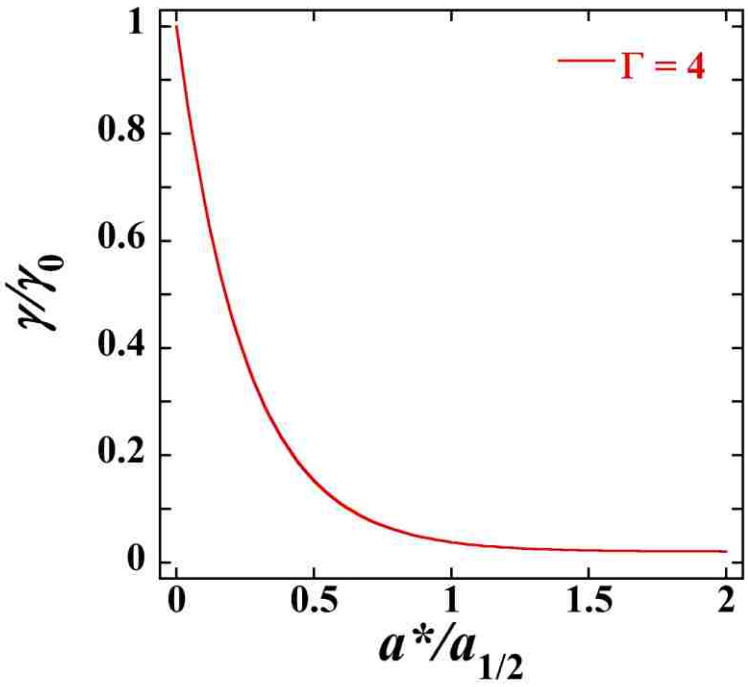

Figure 6-3. The inverse initial slope, γ, is strongly affected by post-cure swelling of the polymer. For $\Gamma = 4$ the increase in sensitivity is more than a factor of 50.

6.3. Controlling Stress with Temperature

To experimentally test the theory of post-cure swelling, we would ideally like to use an irreversibly absorbing, vapor-phase swelling agent. Swelling with an agent such as this is conceptually simple, but not so trivial experimentally, due to the inevitable conductance drift caused by slow desorption of an actual swelling agent. For this reason we first used temperature to swell the composite. Temperature induced swelling is analogous to that of a chemical in that a coefficient of thermal expansion (CTE) mismatch between the polymer and particle phase of the composite allows the matrix to swell while the volume of the particles remains constant—just as a chemical does not swell the particles.

Response curves for a single sensor were determined at several temperatures and are shown in Figure 6-4 below. These curves are quite similar to the predicted behavior

in Figure 6-2, in that the sensitivity increases with temperature-induced swelling, but only to a degree, finally reaching a limiting curve that is exponential. For each elevated temperature we can compute a *fictive activity*, a^*, that can be directly used in Eq. 6-2. This fictive activity is the activity of *p*-xylene vapor that would be required to reduce the composite conductivity at ambient temperature to the composite conductivity at the elevated temperature. The fictive activity is obtained from the ambient, un-normalized response curve (*G* versus *a*), with the result $a^* = 6.25 \times 10^{-3}(T - 25°\text{C})$.

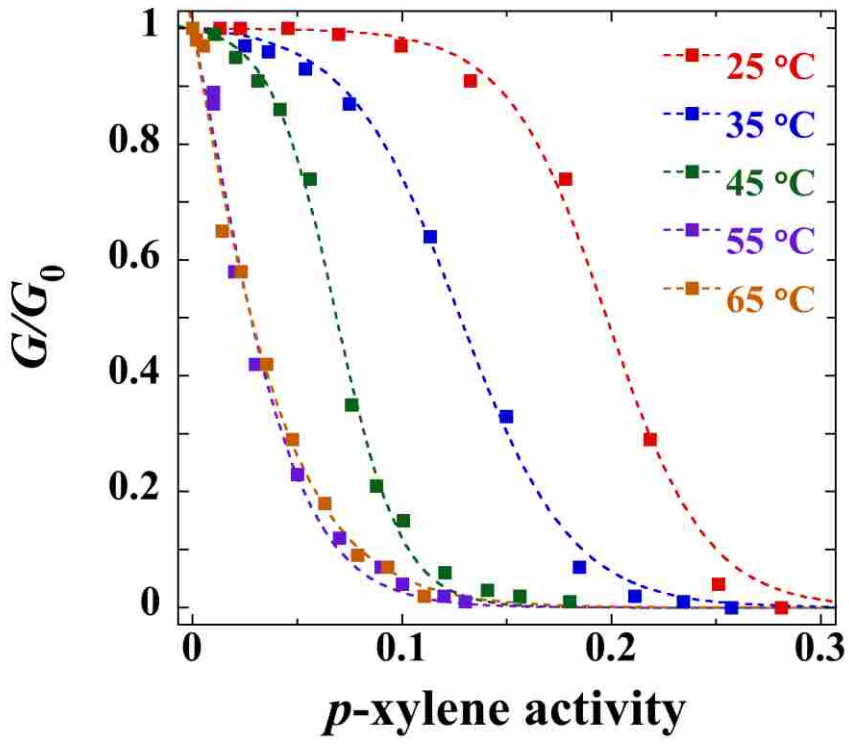

Figure 6-4. Conductance response curves of a single FSCR for temperatures ranging from 25 to 65°C show an increased sensitivity to swelling by *p*-xylene, as expected from Eq. 6-2.

Figure 6-5 is a comparison between the experimentally determined response midpoints taken from the data in Figure 6-4 to Eq. 6-4 shows that the trend is as

expected. As the composite is swollen the vapor activity required to reduce the conductivity by half goes down, but reaches a limiting value, in this case becoming roughly 6.6 times more sensitive by this measure.

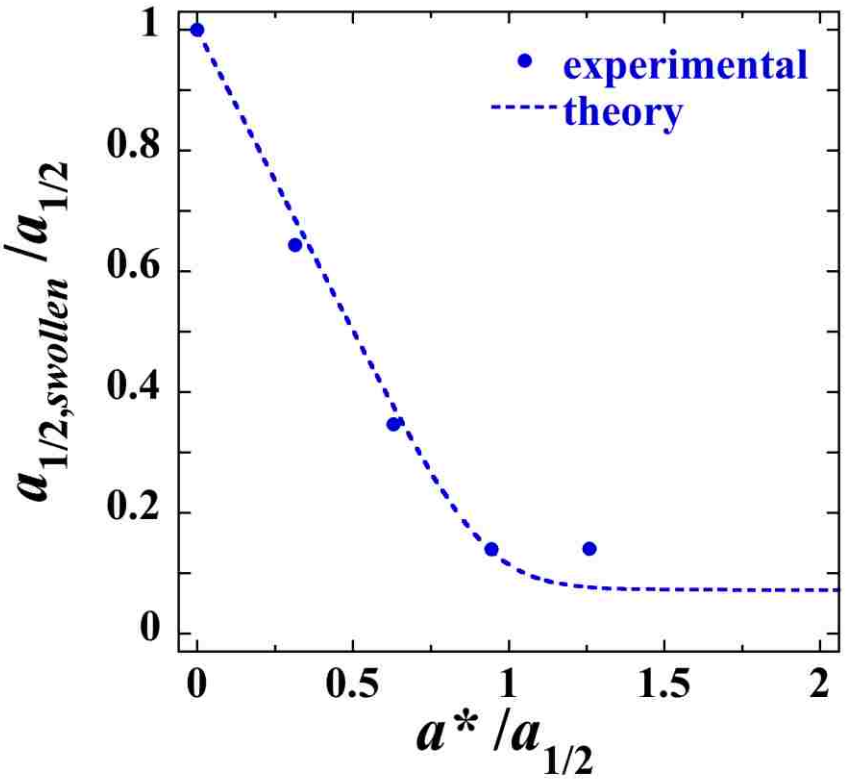

Figure 6-5. A comparison of the response midpoints of the measured curves in Figure 6-4 to theory (Eq. 6-4) shows good agreement and illustrates the value in swelling the composite. Here the response midpoint is decreased by ~7-fold.

6.4. Conclusions

In the previous chapter we adopted the point of view that all particle contacts have the same tunneling resistance, and that this resistance value is determined by compressive strain. This view leads to a specific prediction for the dependence of the composite conductivity on volumetric strain, and demonstrates how reducing the compressive stress within these materials can lead to greatly increased sensitivity. Stress reduction experiments agree with theory and demonstrate that we can dramatically increase the sensitivity of these materials (by as much as 50-fold) to low concentrations of vapor-phase VOCs. This is an important discovery for the use of these materials as sensors. The following chapters detail additional methods we have developed to control stress and thereby control FSCR response.

7. INCREASING FSCR SENSITIVITY USING CHEMICAL SWELLING AGENTS

***Abstract*—**In the previous chapter we conceptualized a fictitious chemical swelling agent to model the effect of swelling on FSCR response. Because of the practical difficulties of using an actual swelling agent, we experimentally tested the theory with thermal swelling. However for field-use, heating the sensor is antithetical to the simplistic, low-power chemiresistor concept. So the ultimate goal for the application of controlling FSCR response is to develop a method for permanently and controllably swelling a chemiresistor. To accomplish this there are two approaches: first, the use of a non-volatile chemical absorbent, and second, the use of a volatile reactant that will swell and chemically bind to the polymer matrix. In this chapter we discuss such swelling agents. It is shown that these swelling agents do indeed increase sensor sensitivity, but their practical implementation suffers from a lack of control over this sensitivity increase. Additionally, sensors treated with thiol swelling agents, which strongly adsorb to the Au-coated particles, show a temporary increase in sensor sensitivity. These data also illustrate why carbon-black particles, which adsorb organics, can cause conductance baseline fluctuations and irreversibility issues.

7.1. Low-Volatility Swelling Agent

The minimum criterion for a compatible swelling agent is that it must remain absorbed for *at least* a sufficient amount time required to detect an analyte. The use of a low-volatility swelling agent is therefore adequate as a proof of concept, however for practical

applications, absorption must be permanent. Initial experiments involved placing an FSCR in an environment saturated with hexadecane vapors. Hexadecane ($C_{16}H_{34}$) was chosen because it has a very low volatility and thus slow sorption kinetics, but can still be administered via the vapor phase. To accomplish this, an FSCR was kept in saturated hexadecane vapors until the response midpoint of the sensor was reached. The FSCR was then quickly transferred to the flowcell where the response to *p*-xylene was measured. The response curves for the sensor before and after hexadecane swelling are in Figure 7-1. The slow hexadecane desorption was characterized by a conductance baseline with a non-zero slope. These data in Figure 7-1 confirm that a chemical swelling agent that is absorbed after cure will increase the sensitivity of an FSCR, although the effect is not permanent.

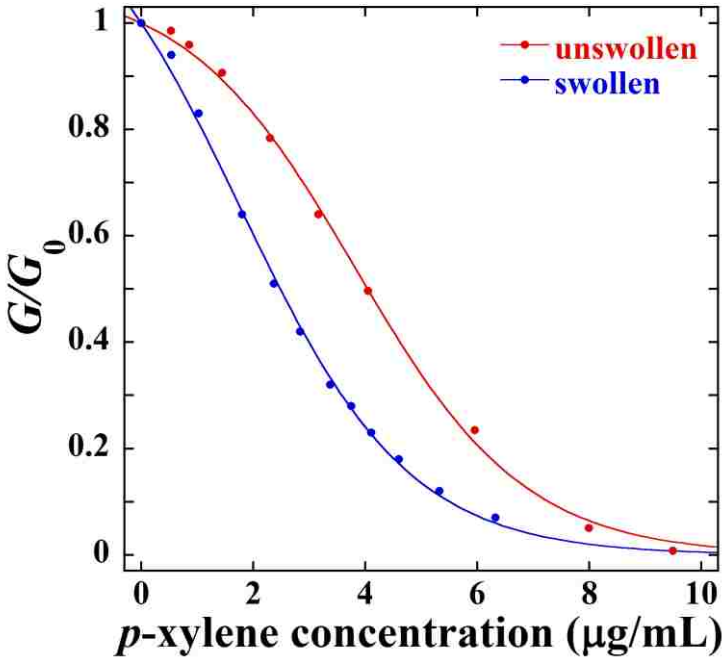

Figure 7-1. Response curves for an FSCR before and after swelling with hexadecane illustrate the feasibility of using a low-volatility swelling agent to increase sensor sensitivity. However this effect is short-lived due to the desorption of the hexadecane.

7.2. Non-Volatile Swelling Agent

We now focus on the use of a non-volatile swelling agent, which is obviously more useful, but also more difficult to controllably administer. Octadecane ($C_{18}H_{38}$) was chosen as the non-volatile swelling agent due to its miscibility with the polymer and low melting point of 28°C. Various methods were employed to swell the composite with the octadecane. The first method involves simply placing a small mass of the solid onto the composite and heating at 45°C. In this case the octadecane melts and absorbs into the composite and re-solidifies upon cooling. This method overloaded the composite and made the sensor completely non-conductive. The second method involved dissolving the $C_{18}H_{38}$ in a volatile carrier solvent mixture such as decane with pentane or hexane. A small quantity of this solution is deposited directly onto the composite using a micro-pipette. The entire volume of solution ($C_{10}/C_6/C_{18}$) deposited onto the solution was equal to 10 vol.% of the polymer phase of the composite in order to minimize damaging effects due to over-swelling the composite. The concentration of octadecane in these solutions was varied such that it would lead to a 1–4 vol.% swelling of the polymer after carrier-solvent desorption. The mean volume of polymer for these particular FSCRs was determined by weighing several FSCR composite samples. The response curves for the sensor before and after octadecane swelling are in Figure 7-2 below.

The response midpoint of the swollen sensor is nearly 5-times lower than that of the senor before swelling with octadecane, which is near the maximum decrease that can be acheived from Eq. 6-4. However, it was discovered that over the course of months, the octadecane slowly evaporates and the FSCR response returns to its original value. In addition there seemed to be little-to-no correlation between the increase in sensor

sensitivity and the volume fraction of octadecane as would be expected. Because of these practical issues it is concluded that this is still not a viable method for controllably increasing FSCR sensitivity.

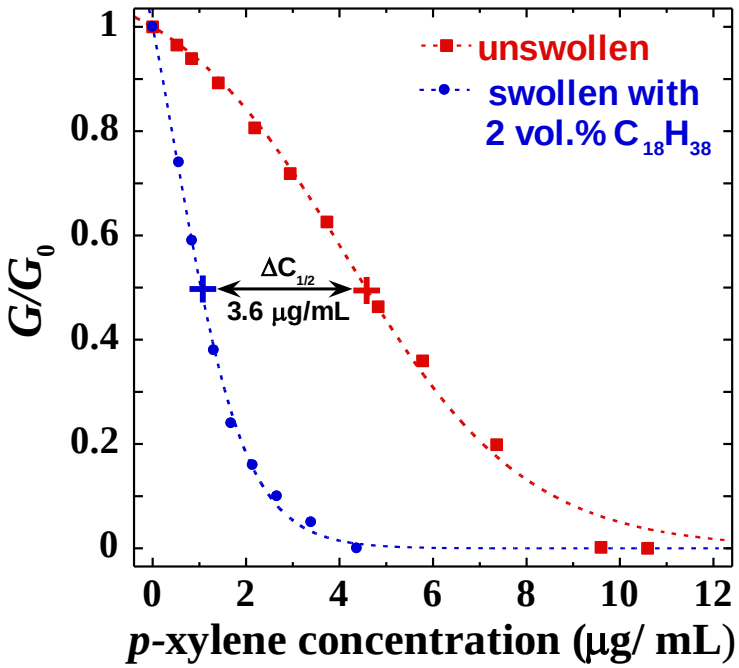

Figure 7-2. The FSCR response curve for a sensor swollen by 2 vol.% with octadecane shows a ~5-fold decrease in response midpoint compared to the sensor before treatment. The swollen sensor also displays vastly increased sensitivity in the limit of low analyte concentration. Though the desorption of octadecane is *extremely* slow, the effect is none-the-less reversible.

7.3. Volatile Reactive Swelling Agents

The problems with using a non-volatile swelling agent inevitably prevent it from being practical. The major drawbacks being that the swelling agent is difficult to controllably administer and we have yet to find a swelling agent that is permanent. For controllable swelling, it would be ideal to use a vapor-phase swelling agent. A swelling agent of this type could be administered in the same manner as an analyte, which would also allow for

in situ monitoring of the swelling. The ideal swelling agent would be have high affinity for the polymer, and upon absorption, would quickly react with, and permanently bond to, the polymer matrix. In the following we describe the use of such reactive analytes.

7.3.1. SILOXANE MONOMER SWELLING AGENT

Initial efforts were geared toward using the high-volatility monomer of the PDMS resin phase. This monomer, vinyl-terminated dimethylsiloxane (VTDMS), is shown in Figure 7-3 below. VTDMS has a molecular weight of 186 g/mol and a vapor pressure comparable to that of xylene (8.8 torr at 25°C). FSCRs were made from PDMS with a stoichiometric ten-fold excess of the crosslinker (methylhydrosiloxane /PDMS copolymer). The hypothesis being that the vinyl groups on the monomer would react with the excess methylhydrosiloxane groups in the polymer matrix by the chemical reaction in Figure 7-3 below.

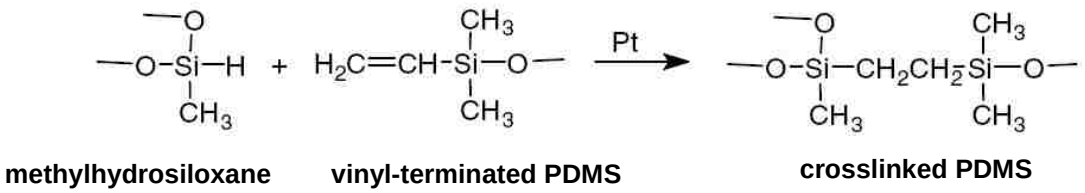

REACTIVE ANALYTE

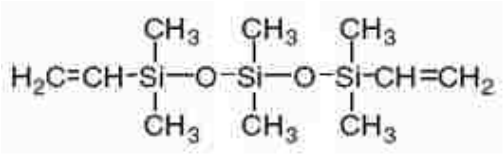

Figure 7-3. (top) the platinum-catalyzed chemical reaction between the methylhydrosiloxane-PDMS copolymer (crosslinker) and the vinyl-terminated PDMS (resin) to form the PDMS elastomer (Gelest OE 41). A stoichiometric excess of the

crosslinker should react with the low molecular weight monomer (VTDMS) **(bottom)** to permanently swell the composite.

An FSCR response experiment was performed using VTDMS as the analyte. After the response curve was completed, the concentration of VTDMS was set to elicit a response of $G/G_0 = 0.8$. The FSCR was exposed to this concentration of VTDMS for 48 hours at which time the flowcell was purged with nitrogen and any un-reacted VTDMS was allowed to desorb. Unfortunately all of the monomer desorbed and the FSCR returned to its original baseline conductivity indicating that no reaction had taken place. This experiment was repeated with saturated VTDMS vapor exposing the FSCR for as long as a two-week period with no success. Gravimetric swelling experiments with PDMS also showed negligible permanent absorption. It is therefore concluded that the reaction kinetics—even with a greatly increased catalyst concentration and an excess of crosslinker—are ultimately too slow to consider VTDMS as a worthwhile candidate as a permanent swelling agent.

7.3.2. HIGHLY-REACTIVE VOLATILE SWELLING AGENTS: ISOCYANATES

In an effort to increase the reaction kinetics between the swelling agent and the polymer phase, several options were considered. One of the most promising options involves a complete change of the elastomer system in order to have highly reactive functional groups within the polymer matrix. One such reaction is that of an amine group and an isocyanate to form a urea linkage as shown below in Figure 7-4. Isocyanates have the structure R—N==C==O and are available in a variety of forms, many of which have sufficient volatility to be used as a vapor-phase swelling agents. The first hurdle to

overcome was to formulate an elastomer that will work as the polymer phase of an FSCR, and also have a ample number of active amine groups to react with the isocyanate to sufficiently swell the FSCR. To form such an elastomer, we began by experimenting with reacting amine and epoxy terminated PDMS copolymers commercially available from Gelest, Inc.. These precursors are generally used as commercial epoxy additives to alter epoxy material properties and not as stand-alone elastomer systems. Because of this, the amount of literature on formulating an epoxy/amine curing elastomer is nil. A great deal of in-house research was dedicated to simply formulating an elastomer system, which meets the prescribed criteria of: low modulus (high elasticity), low cure stresses, no volatility, and the ability to cure with a high amine-to-epoxy ratio. This last criterion ensures sufficient excess amine groups for subsequent isocyanate reaction. The polymer phase used for the following experiment is made using 96 % wt. AMS-233 and 4 %wt. ECMS-227, which are amine and epoxy functionalized PDMS precursors offered by Gelest, Inc. The catalyst DMP-30 was added to the precursor mixture at 10 % wt and the composite was cured at 65 °C for 16 h.

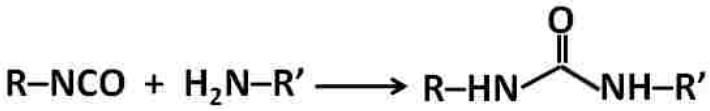

Figure 7-4. The reaction of an isocyanate (right) and an amine (left) produce a urea linkage.

The response of an amine-epoxy PDMS sensor before and after swelling with trimethylsilyl isocyanate (obtained from Acros Organics, CAS # 1118-02-1) are shown below in Figure 7-5. As with the previous swelling agents, the sensor is more sensitive

to *p*-xylene after treatment with the isocyanate, illustrating the success of using isocyanates as a post-cure swelling agent. The effect from the isocyanate, however, differs from the previously discussed swelling agents in its irreversibility—as expected. Measurements of the sensor's baseline conductance and the response over the course of several months showed no change, indicating that the swelling is permanent.

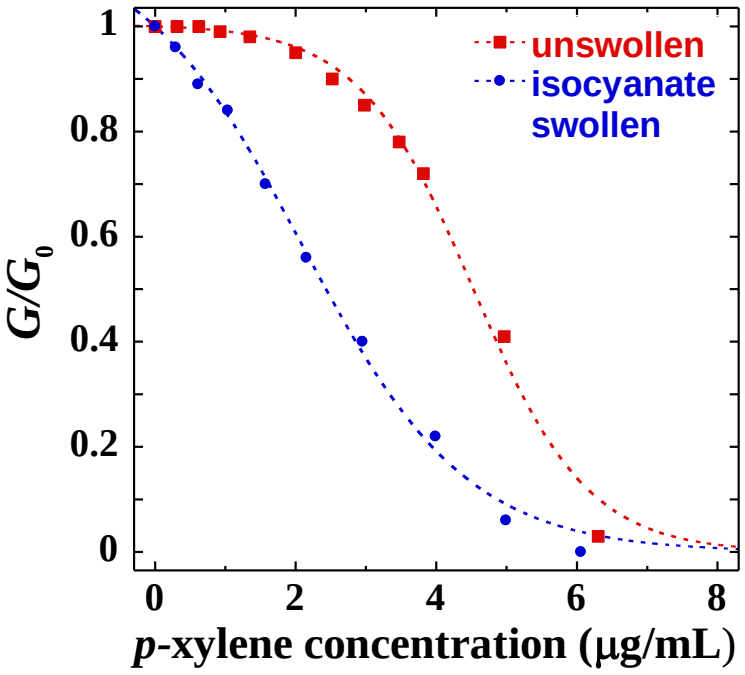

Figure 7-5. Response of an amine-functionalized PDMS FSCR before and after swelling with the reactive analyte trimethylsilyl isocyanate. The sensitivity of the sensor is increased, especially at low analyte concentrations, and the effect is permanent.

Despite the success of this demonstration, there are a few remaining issues. First, this method yet lacks control over the amount of swelling. It is assumed that all of the amine functional groups are reacted with the isocyanates. Therefore the finite amount of amine groups determines the maximum amount of swelling that can take place with a given isocyanate compound. The total amount of swelling can be varied in a few ways:

first, by controlling the amount of free amine groups; second, by varying the molar volume or molecular weight of the swelling agent per isocyanate group; and lastly, by using bifunctional isocyanates followed by a bifunctional amine swelling agent to carry out a controlled step polymerization within the composite as we describe below.

For this step polymerization, a bifunctional isocyanate such as *hexamethylene diisocyanate* (Figure 7-6 below) could be used to react with the amine functionalized PDMS. This reaction would leave an excess of un-reacted isocyanate groups, which could be further reacted with a bifunctional amine. Further swelling could then be achieved by again using the bifunctional isocyanate, and so on, by the reaction in Figure 7-7 below. This step-wise polymerization within the elastomer could be repeated until the desired swelling of the FSCR composite is reached. Work on isocyanates was not performed past the proof of concept stage (Figure 7-7) due to funding limitations.

Figure 7-6. Hexamehtylene diisocyanate is an example of a bifunctional isocyanate that could be used as a polymerizing volatile swelling agent.

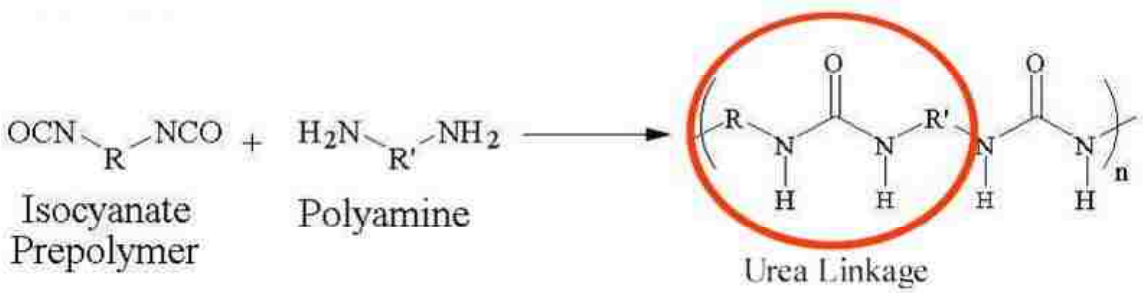

Figure 7-7. The reaction between a diisocyante and a polyamine would form polyurethane within the FSCR composite. This step-wise polymerization method could be used for the case when sufficient swelling could not be achieved by a monofunctional isocyante alone.

7.4. Particle Phase Adsorbents as Swelling Agents

In the previous section we focused on the use of isocyanates, which react with the polymer phase of the composite. We now focus on a class of swelling agents that interact with the particle phase. Thiols are molecules of the form R–SH and which are known to strongly adsorb to gold surfaces to form self-assembled monolayers (SAMs).[45] Therefore we expect that a vapor-phase alkanethiol will swell the polymer and that a fraction of these molecules will semi-permanently adsorb to the Au-coated particles and substrate electrodes. This should be characterized by a lack of total recovery of the sensor's baseline conductance upon desorption of the unbound alkanethiol.

Figure 7-8a below shows the time-dependent response of two FSCRs with disparate sensitivities to the volatile analyte 1-hexanethiol. (The origin of the disparate sensitivites, which is cure temperature, will be discussed in the following chapter.) As expected, the thiol shows typical absorption, but upon purging with nitrogen, the conductance baseline does not fully recover. The adsorbed thiol accounts for a ~10% decrease of the baseline for the less-sensitive sensor and ~25% for the more-sensitive sensor. Figure 7-8b shows the response kinetics of two sensors to two consecutive thiol exposures at the same activity. Again, after the initial exposure to the thiol, the baseline is not recovered. The subsequent exposure elicits an identical response and upon desorption the conductance returns to the same post-thiol baseline indicating that the sensor was saturated with adsorbed thiol very quickly, the first time. Figure 7-8b illustrates that the total adsorption is the same from the first to the second exposure, but of course this would appear as an increase in sensitivity if the post-thiol baseline was used as the new G_0.

Figure 7-9 illustrates the effect of a low volatility thiol as a swelling agent. For this experiment three FSCRs with varying sensitivities were exposed to 1-undecanethiol for 24 hours after which their responses to toluene were measured. The low and moderate sensitivity sensors show a large increase in sensitivity, where the most sensitive sensor was made non-conductive by the thiol exposure.

The use of thiols is yet another example of the utility of a vapor-phase swelling agent for increasing FSCR sensitivity. Though the desorption kinetics for the adsorbed thiols is extremely slow (on the order of weeks), this effect is not permanent. However, the real utility of this experiment is to illustrate the effect of an analyte that strongly adsorbs to the particle phase. The interaction between the thiols and the gold particles is analogous to the interaction that would be expected for carbon black particles and volatile organics in general. Carbon black is activated carbon with less-surface area, and activated carbon's main use is to *capture* organics other than alcohols and gylcols. These strong adsorption properties are certainly a possible explanation as to why carbon black chemiresistors have issues with irreversibility and baseline drift.

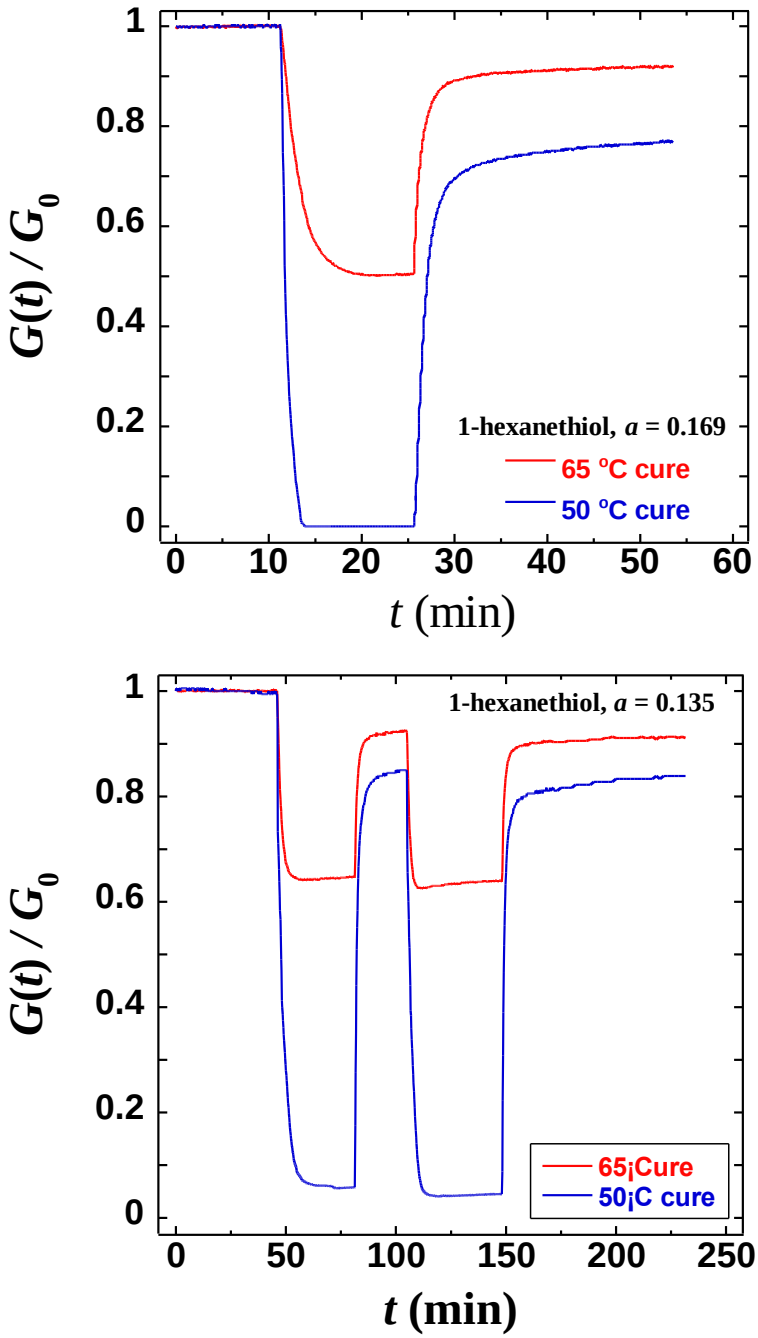

Figure 7-8. **(a)** Two sensors with disparate sensitivities are exposed to 1-hexanethiol vapors at an activity of 0.169. After puging with nitrogen the sensors' baselines are not fully recovered indicating strong adsorption of the thiol to the gold-coated particles. **(b)** Two consecutive exposures of two sensors to hexanethiol shows that the total response to the pre-thiol baseline is unchanged. The recovery of the post-thiol baseline indicates that the FSCR was saturated with adsorbed thiol after the first exposure.

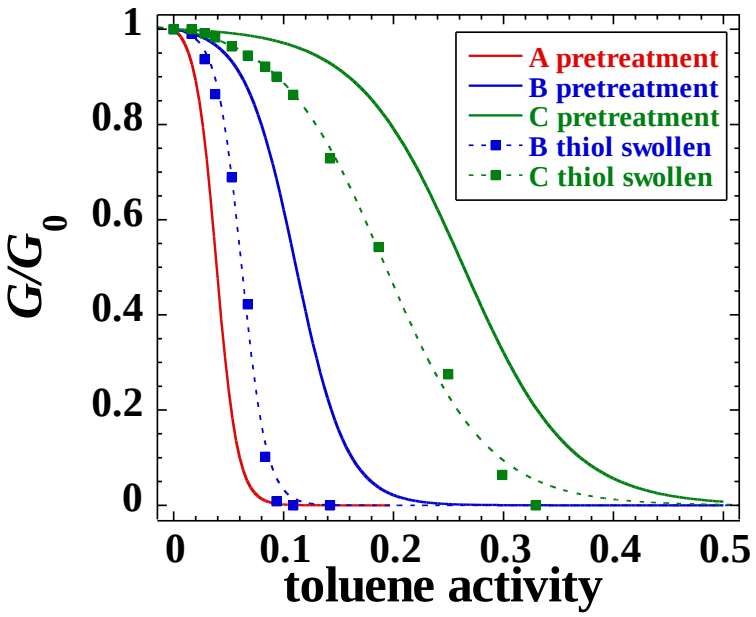

Figure 7-9. Three sensors with dissimilar sensitivites were exposed to saturated 1-undecanethiol vapors for 24 h. The response curves to toluene before and after the thiol exposure show a large increase in sensitivity. In fact sensor A was completely non-conducting after the thiol adsorption.

7.5. Conclusion

We have demonstrated, using a number of methods, that chemical swelling agents are capable of increasing sensor sensitivity to an analyte. The minimum criterion for a swelling agent is that it must remain absorbed in the polymer for at least a long-enough time for an analyte to be detected. Of course for practical implementation of this method, a swelling agent must be permanently and controllably absorbed. We have further demonstrated that reactive vapor-phase isocyanates offer a means of permanent swelling, but as of now do not lead to the *controllable* increase in sensitivity we seek. However, we proposed a method for achieving this control, which could be the subject of future research. Lastly, we showed that volatile analytes that strongly adsorb to the particle phase, such as thiols, also increase sensitivity, but due to their slow desorption, this effect

is temporary. Adopting the view of these thiols as adsorbing analytes instead of swelling agents, illustrates how using composites with strong adsorption properties can lead to irreversible sensor response and undesirable baseline offset and drift. This serves as an illustrative model as to why carbon-black chemiresistors might have these issues with all analytes—carbon black being an adsorbent of organics in general.

8. USING VOLUMETRIC COMPRESSIVE STRESS TO CONTROL FSCR RESPONSE

***Abstract*—**In the previous chapters we have shown the utility of relieving compressive stresses to increase sensitivity. In this chapter we demonstrate methods of *inducing* compressive stress to control FSCR sensitivity. One such method involves curing the composite while swollen with a miscible low-volatility chemical. This low volatility swelling agent is removed after cure, which results in a compressive stress field. We demonstrate that this stress field causes the response curve to be shifted to higher analyte concentrations while maintaining high, chemical-switch-like sensitivity. This allows for the development of *homo*-polymer chemical-switch arrays that can maintain high sensitivity over extremely large analyte concentrations. In addition, these arrays could be used to quantify an analyte's concentration with a simple logic circuit. We demonstrate another method for inducing compressive stress, which entails curing the sensor at increased temperature. This has the effect of stretching the response curve, which leads to a decrease in sensitivity, but also an increase in the sensing range.

8.1. Homopolymer Chemical Switch Arrays

8.1.1. INTRODUCTION

If sensors of a particular polymer could be fabricated with a response midpoint that could be shifted, then it would be possible to create a homopolymer array of sensors having overlapping response ranges such as those shown in Figure 8-1 below. Such an array would have high sensitivity (steep slope) over a wide concentration range—essentially an array of chemical switches with ever-increasing switching points. For this concept to be

especially useful, the chemical affinity of the polymer must be unchanged, so that various homopolymer arrays of disparate chemical affinities could eventually be combined to form a 2-d sensor array that acts as an artificial nose. One axis of this array would be sensitivity; the other would be chemical affinity. Obvious sensor variables include the particle size and concentration, and the magnetic field strength and symmetry (1-, 2-, or 3-dimensional), but these factors do not lead to the pronounced effects we seek. The compressive stress within the polymer is a less obvious variable, but it turns out that it is the key to shifting the sensor response curve while not altering its chemical affinity, as we will demonstrate.

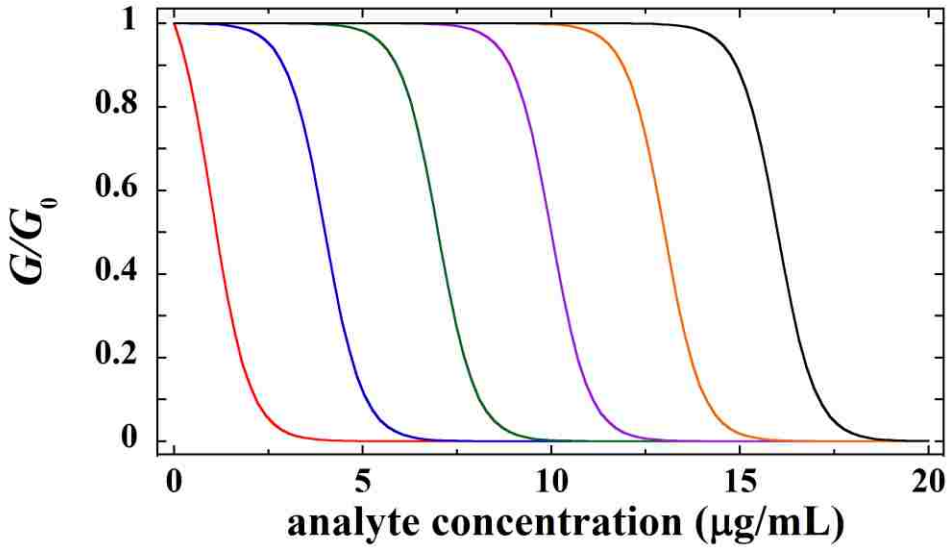

Figure 8-1. An idealized array of overlapping chemical sensors would maintain high sensitivity over a broad range of analyte concentrations.

8.1.2. USING COMPRESSIVE STRESS TO CREATE CHEMICAL SWITCH ARRAYS

To shift the response curve to higher analyte concentrations, the compressive stress field within the polymer must be increased. To accomplish this we mix the nonvolatile,

miscible liquid hexadecane into the prepolymer resin. The resin is then cured in the magnetic field without allowing the liquid to evaporate. Subsequent to cure, the hexadecane is evaporated by mild heating. As the composite deswells a compressive stress field is created that is additional to that attendant to polymer cure shrinkage. This compressive stress field shifts the sensor response to higher analyte concentrations without broadening the response range.

The success of this approach can be judged from the *p*-xylene response curves in Figure 8-2 for sensors made with 0, 1, 2, and 4 vol.% hexadecane. The response curves shift right with increasing hexadecane, finally achieving a response midpoint of 36 μg/mL, which is roughly 20 times as high as the control sensor. Higher concentrations of hexadecane shift the response curves even further: a sensor made with 20 vol.% hexadecane does not even respond to saturated *p*-xylene vapors, which are 58 μg/mL at room temperature. Our most sensitive sensor can respond to xylene concentrations of ~0.05 μg/mL, so our response range spans over three decades. Such sensors would be ideal as input for a multi-channel comparator or for use in chemical logic circuits.

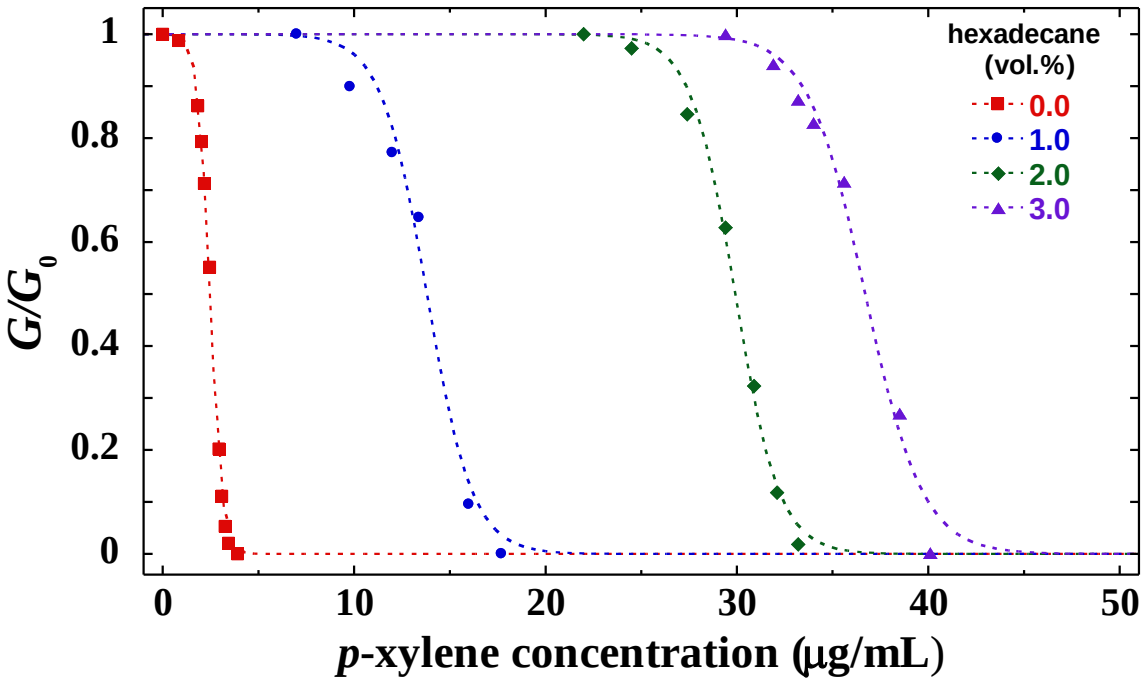

Figure 8-2. Demonstration that FSCR response can be controlled by pre-swelling with hexadecane. The shift in response midpoint is large and controllable with little-to-no effect on sensitivity. A homogeneous sensor array such as this has high sensitivity over a broad analyte concentration range.

The mechanism of the sensitivity shift, schematically illustrated in Figure 8-3, is easily understood. Mass sorption experiments show that FSCRs made *without* hexadecane become non-conducting when the analyte swells the polymer by ~1 vol.%, depending on the sensor. FSCRs swollen with hexadecane during cure require a similar amount of *additional* swelling to become non-conducting. When the hexadecane is evaporated, the required polymer swelling increases by the volume fraction of volatilized hexadecane. For example, if a sensor is made with 6 vol.% hexadecane, and all of this is evaporated, then the analyte will need to swell the polymer by ~7 vol.% for the sensor to become non-conducting. This degree of swelling requires a much larger analyte concentration.

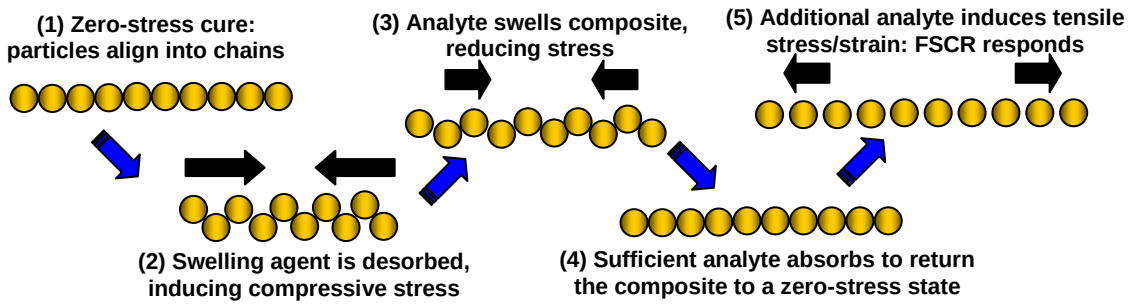

Figure 8-3. This schematic illustrates the mechanism by which the response of a sensor is changed by curing the composite in a swollen state and deswelling before analyte exposure. Here the thick black arrows represent the polymer-stress vectors. An unswollen FSCR is described by steps 1 and 5 alone.

8.3. Cure-Temperature Control

In addition to chemically deswelling the polymer, elevating the cure temperature can also be used to increase the compressive stresses within the polymer. This is due to the mismatch in the coefficient of thermal expansion (CTE) between the polymer and the magnetic particles, as we discussed in Chapter 6. Because the cure temperature is nearly a zero-stress temperature for the cured polymer, and the polymer has a larger CTE than the particles, the compressive stress is nearly proportional to difference between the device operation temperature and the cure temperature. Sensor sensitivity should therefore decrease with increasing cure temperature, and Figure 8-4a confirms this. These curves are not shifted, but are actually *stretched*, as evidenced by the fact that all of these curves have similar transition parameters, Γ. This stretching enables homo-polymer arrays to be made with just a few sensors, if greater simplicity in the sensor system circuitry is desired.

The data in Figure 8-4b show the cure temperature dependence of the sensor response midpoint. The sensor cured at room temperature (25°C) has a response midpoint of 1.6 μg/mL xylene. This midpoint value increases smoothly with increasing cure temperature until a midpoint of 16.5 μg/mL is achieved at a cure temperature of 95 °C. This ten-fold midpoint increase shows that FSCRs can be fabricated to accommodate widely varying response needs.

It is possible that the shift to lower sensitivity with increasing compressive polymer stress is due to a decrease in the swelling of the polymer at a given analyte concentration. But mass sorption experiments we have conducted show that the relationship between polymer swelling and the vapor concentration is unaltered by the levels of stress in our sensors. The additional stress must alter the device transduction curve (dependence of charge conduction on swelling) itself. These data and a detailed discussion on polymer swelling as it pertains to the transduction curve is presented in Chapter 10.

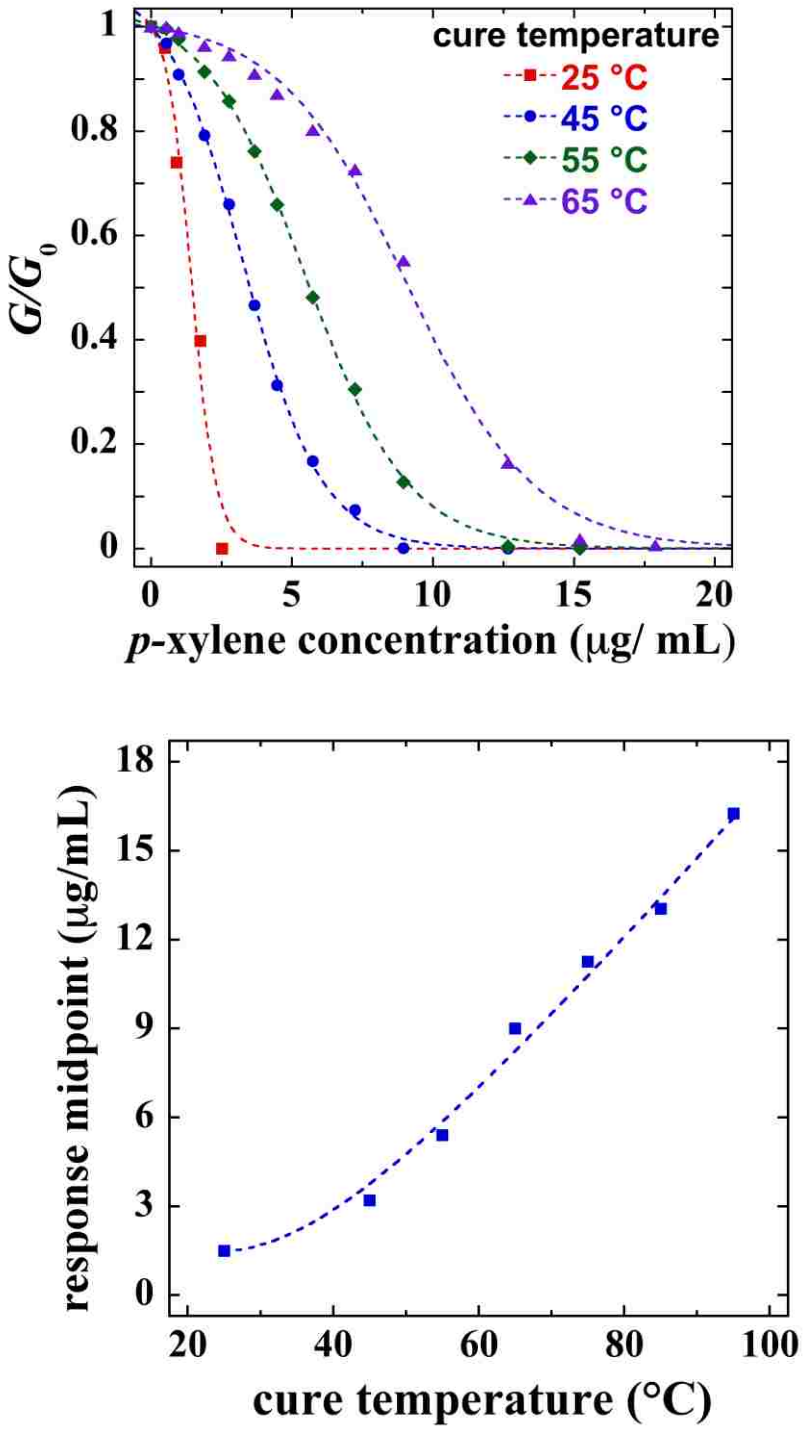

Figure 8-4. **(a)** Increasing the cure temperature increases the dynamic range and response midpoint where the transition abruptness parameter Γ is nearly unchanged. The curves from left to right represent FSCRs cured at 25, 45, 55, and 65 °C. **(b)** The response midpoint increases smoothly with increasing cure temperature with as much as a 10-fold increase.

8.4 Conclusions

We have demonstrated methods of *inducing* compressive stress to control FSCR sensitivity. We have shown that curing the composite while swollen with a miscible low-volatility chemical allows us to shift the response curve to higher analyte concentrations while maintaining high, chemical-switch-like sensitivity. This allows for the development of *homo*-polymer chemical-switch arrays that can maintain high sensitivity over extremely large analyte concentrations. In addition, these arrays could be used to quantify an analyte's concentration with a simple logic circuit. Additionally we have demonstrated a method for inducing compressive stress by curing the sensor at increased temperature. This has the effect of stretching the response curve, which leads to a decrease in sensitivity, but also an increase in the sensing range. In the following chapter we describe methods for dynamically shifting sensor response to higher sensitivity. These methods enable chemiresistor response to be controllably tailored to suit a wide variety of applications.

9. A STRAIN-TUNABLE CHEMIRESISTOR

***Abstract*—**We have developed field-structured chemiresistor whose sensitivity can be reversibly increased over a range of nearly two decades by the application of a tensile strain. We have found that applying a tensile strain increases both the sensor resistance and sensitivity, as defined by its relative resistance change. This increase in sensitivity is a smooth, continuous function of the applied strain, and the effect is fully reversible. Sensitivity tuning enables the response curve of the sensor to be dynamically tuned for sensing analytes over a wide concentration range.

9.1. Introduction

The sigmoidal response curve of a typical chemiresistor is relatively flat at the onset of the curve, so the sensor is insensitive at low analyte concentrations. We have found that applying a tensile strain to the sensor can greatly increase its sensitivity in the low-concentration regime. This effect is fully reversible and enables the development of an actuator-controlled chemiresistor that can *accurately* sense over a range of more than three decades of analyte concentration. In the following, we demonstrate such a prototype device and provide response data for a model analyte.

9.2. Background

When a chemiresistor is exposed to chemical vapors the polymer swells in proportion to the analyte concentration.[46] This volumetric strain reduces the contact pressure between particles, increasing the sensor resistance.[35] As introduced in Chapter 3, we model the typical sigmoidal response curve of an FSCR with

$$\frac{G}{G_0} = \left[1 + \frac{e^{\Gamma C/C_{1/2}} - 1}{e^{\Gamma} - 1}\right]^{-1}. \qquad \textbf{(9-1)}$$

The FSCR sensitivity is defined as the relative slope of the response curve at a specific analyte concentration, so taking the derivative of Eq. 9-1 yields the expression

$$S(C) \equiv -\frac{d(G/G_0)}{dC} = -\frac{\Gamma e^{\Gamma C/C_{1/2}}}{C_{1/2}\left(1 - e^{\Gamma}\right)}\left[1 + \frac{e^{\Gamma C/C_{1/2}} - 1}{e^{\Gamma} - 1}\right]^{-2}. \qquad \textbf{(9-2)}$$

Figure 9-1a illustrates typical equilibrium response data and Figure 9-1b shows the change in sensitivity over the sensing range. Here, the maximum sensitivity occurs at the sensor's response midpoint, whereas at the upper and lower limits of the sensing range the sensitivity is quite low. The initial sensitivity of an FSCR is the slope in the limit of zero analyte concentration,

$$S_0 \equiv \lim_{C \to 0} S = \frac{\Gamma}{C_{1/2}\left(e^{\Gamma} - 1\right)}. \qquad \textbf{(9-3)}$$

This initial sensitivity determines the sensor's *lower detection limit* (*LDL*). It is conventional to define the LDL as the concentration that gives a change in FSCR conductance three-times greater than the standard deviation of the baseline conductance, σ_{G_0},

$$\frac{G(LDL)}{G_0} \equiv 1 - \frac{3\sigma_{G_0}}{G_0}. \quad \textbf{(9-4)}$$

The LDL is then:

$$LDL = \frac{3\sigma_{G_0}}{S_0 G_0}. \quad \textbf{(9-5)}$$

In the following, we demonstrate a 55-fold decrease in the sensor's LDL by increasing the initial sensitivity, S_0, through the application of a tensile strain.

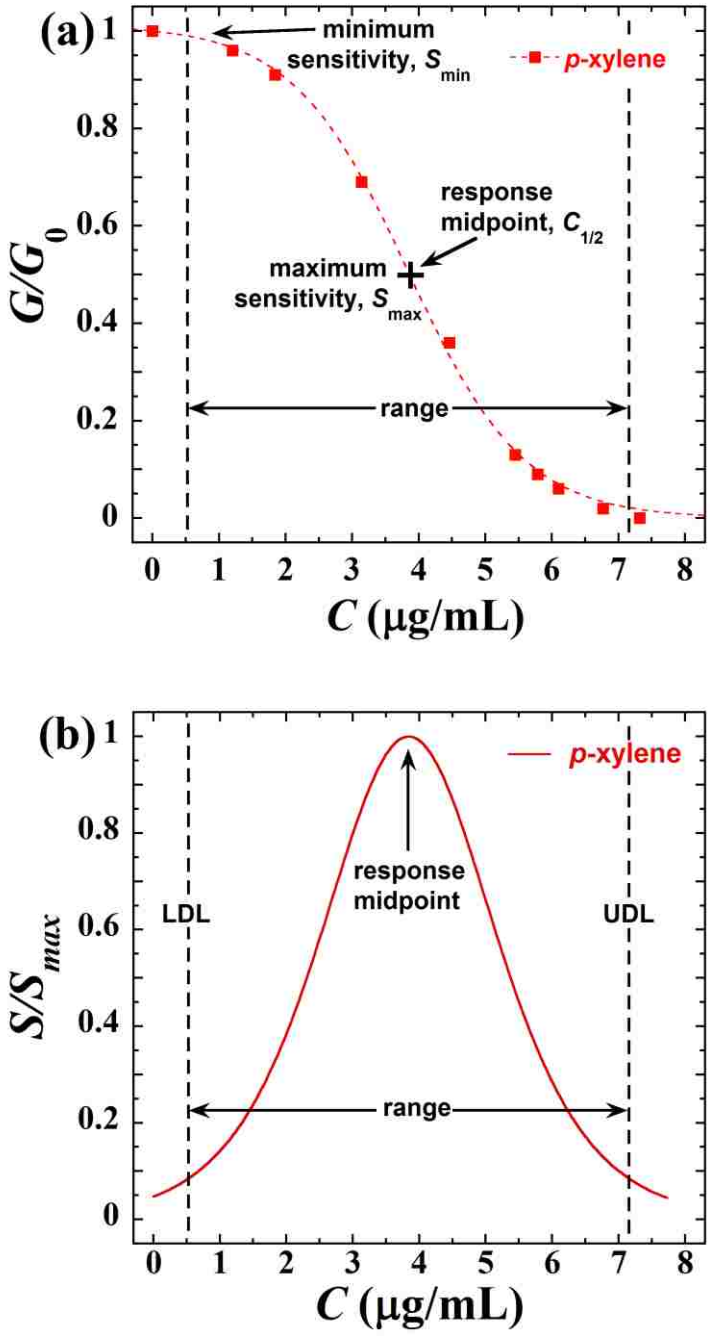

Figure 9-1. **(a)** The FSCR response curve in terms of normalized conductance, G/G_0, for the analyte *p*-xylene is sigmoidal in shape and has a *response midpoint* of ~ 4 μg/mL. **(b)** Plotting the FSCR's relative sensitivity, S/S_{max}, illustrates the dramatic change in sensitivity over the sensing range. For an unaltered sensor, such as this, the maximum sensitivity occurs at the response midpoint, whereas minimum sensitivity occurs at the lower and upper detection limits of the sensor (*LDL* and *UDL*).

9.3. Experimental

To apply a tensile strain, the sensor is formed on a flexible elastomeric substrate. The Gelest OE-41 PDMS is used for both the substrate and the polymer phase of the FSCR composite. The chemiresistor is made by mixing 15 vol.% typical gold-plated nickel particles into the viscous PDMS precursor and curing at 50 °C for four hours in a uniform 650 G magnetic field. The electrodes are made of gold mesh (Advent Research Materials Ltd., part# AU518901), and are partially encapsulated between the composite and the flexible substrate. A schematic of the mechanical strain device and the modified chemiresistor are shown in Figure 9-2.

The chemiresistor composite and gold-mesh electrodes are bonded to the substrate by placing them on the elastomeric substrate just before the substrate is fully cured (*i.e.*, just after it has reached its gel point). At this point, the substrate is still tacky to the touch, but is sufficiently solidified to be able to support the electrodes and the viscous chemiresistor composite precursor. Because the substrate is not yet fully cured, a fraction of unreacted functional groups can chemically bond with the curing chemiresistor composite. Chemical bonding of the chemiresistor to the substrate allows any strain within the substrate to be transferred directly to the chemiresistor with no slippage or delamination. This method has the added benefit of encapsulating the gold-mesh electrodes between the substrate and chemiresistor composite for robustness. Using an elastomer as the substrate and as the continuous phase of the chemiresistor composite also enables the induced strain to be reversible.

The strain apparatus and sensor are enclosed in a shielded flowcell with gas inlet and outlet ports and electrical throughputs. The tensile strain apparatus (Figure 9-2a)

consists of two abutting, but separable, surfaces to which the elastomeric chemiresistor substrate is clamped at opposing ends. These separable surfaces are held together by a compressed spring until a micrometer-calibrated screw pushes the surfaces apart, stretching the elastomeric substrate and bonded chemiresistor composite. The uniaxial *Cauchy strain* of the FSCR, e, is the ratio of the change in length of the FSCR/substrate, ΔL, to the unstrained length, L_0: $e = \Delta L / L_0$. Although this prototype relies on a screw mechanism to strain the chemiresistor, one can envision using various means of actuation, such as piezoelectric materials, pistons, solenoids, etc.[35,47–49] In the concluding section of this chapter we demonstrate the use of an applied magnetic field for straining the chemiresistor composite. This phenomenon, known as magnetostriction, is an inherent property of field-structured composites in general.

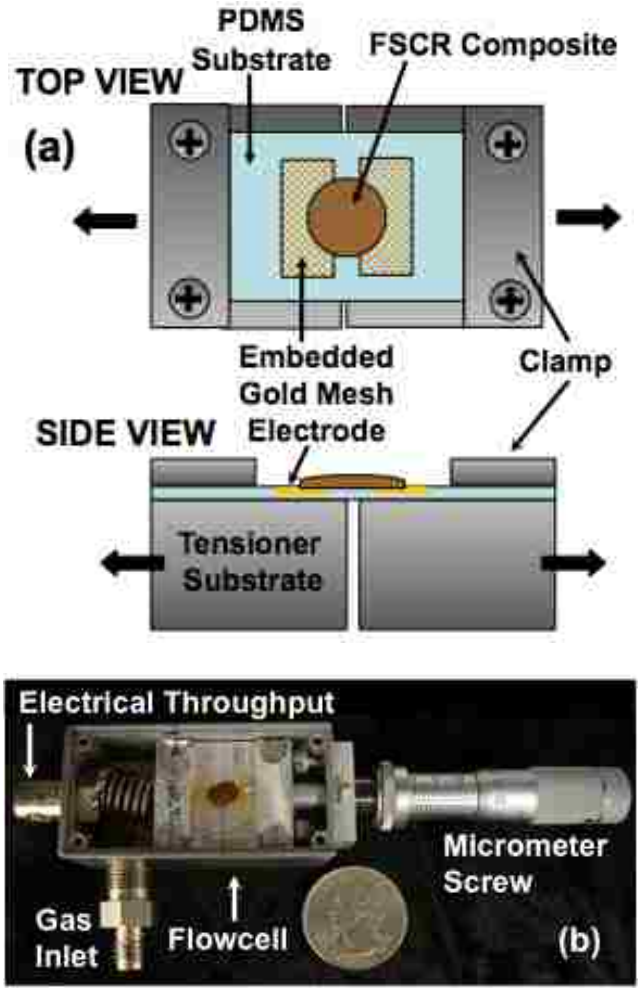

Figure 9-2. **(a)** Schematic view of the mechanical strain device and tunable chemiresistor. **(b)** The prototype mechanical strain chemiresistor tuning device and flowcell (U.S. quarter for size reference).

9.4. Results And Discussion

The dependence of the FSCR conductance on tensile strain is shown in Figure 9-3. Although a tensile strain is certainly different from a volumetric strain, the sigmoidal shape of this strain response curve is similar to that for swelling with an analyte (Figure 9-1a). Fitting the data in Figure 9-3 to Eq. 9-1 yields a response midpoint of

$e_{1/2}$ = 31.2 part-per-thousand strain. In the following, we will normalize the tensile strain values by this response midpoint value.

To determine the effect of tensile strain on FSCR chemical response, the sensor is first strained in the absence of analyte to achieve the desired baseline conductance, and then the chemical response curve is obtained.[9] Figure 9-4a shows the response of the mechanically strained sensor to toluene for various prestrains, and Figure 9-4b shows the corresponding sensitivity curves. The response curve for the unstrained sensor has the typical sigmoidal shape that gives low sensitivity at low analyte concentration. However, as the tensile strain increases there is a progressive degradation of this sigmoidal shape, and the curvature of the response curve becomes purely negative. The maximum sensitivity increases significantly with tensile strain *and* the position of this maximum shifts towards zero analyte concentration. The change in the abruptness of the conductor/insulator transition is quantitatively evident from the decreasing Γ values in Table I. This single sensor can detect toluene concentrations between 0.051 and ~ 75 μg/mL—a range spanning nearly three decades.

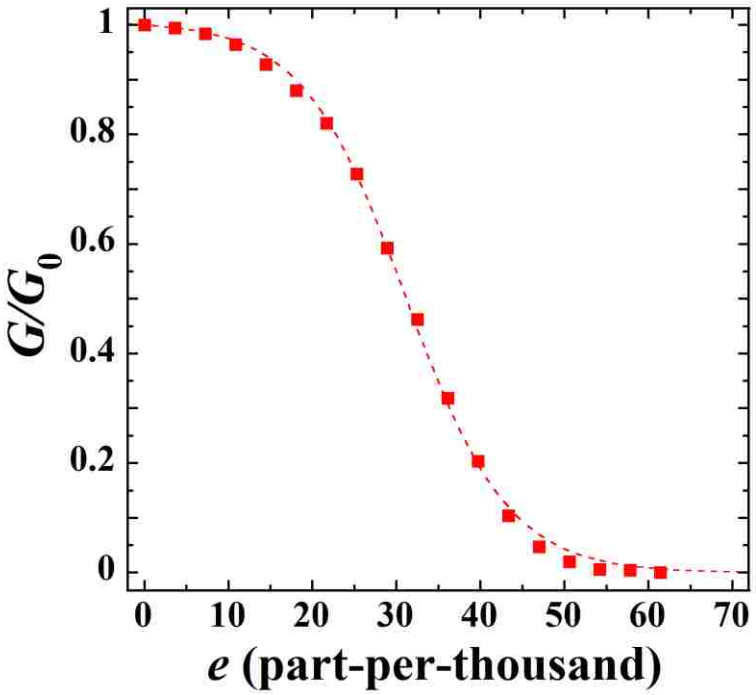

Figure 9-3. FSCR response to mechanically induced tensile strain, *e*. Although the mechanism and type of strain (uniaxial vs. volumetric) is different, FSCR response to tensile strain yields a sigmoidal curve similar to that for chemical swelling (Figure 9-1a). A fit of these data to Eq. 9-1 yields the constants: $\Gamma = 5.09$ and response midpoint, $e_{1/2} = 31.16$ part-per-thousand ($R^2 = 0.999$).

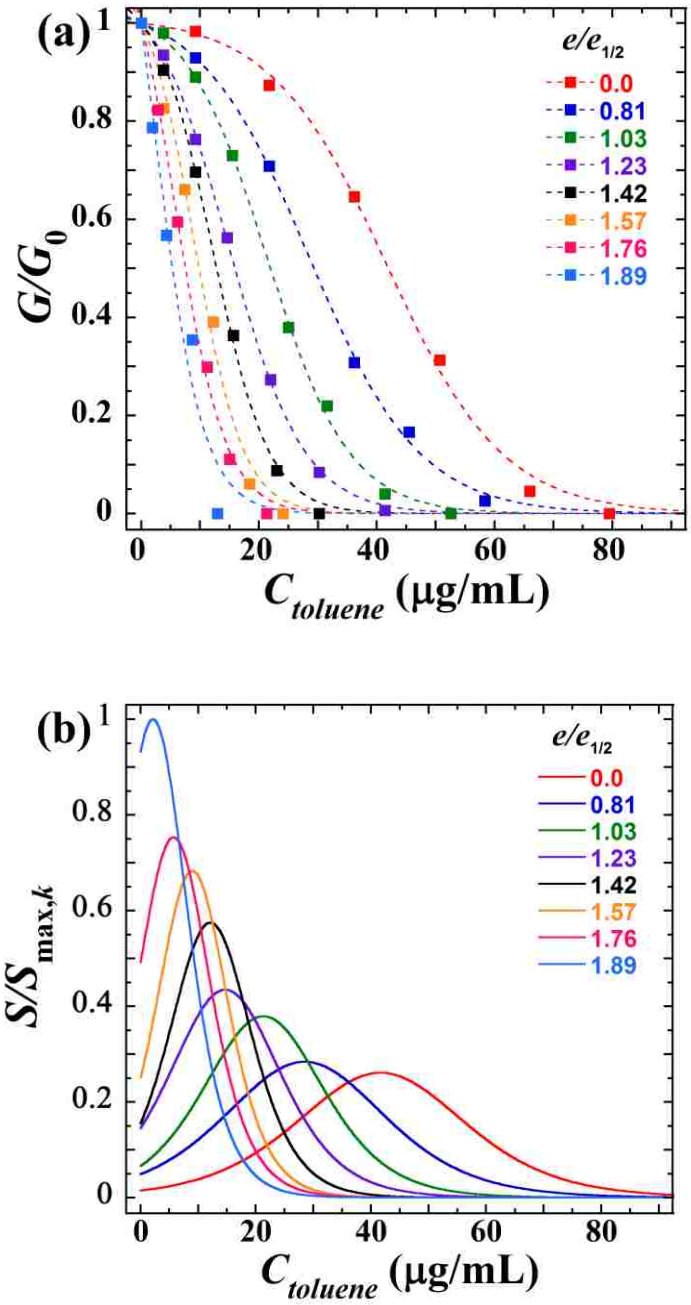

Figure 9-4. **(a)** FSCR response to toluene vapors for various prestrained states shows a dramatic increase in the sensitivity of the sensor. Here we see a detection range spanning nearly three decades. **(b)** Relative sensitivity plots for the prestrained FSCR illustrate not only the increase in sensitivity, but also the change in the shape and symmetry of the curve. For the prestrained sensors, the maximum sensitivity no longer corresponds to the midpoint response, but instead progressively shifts toward lower analyte concentrations. $S_{max,k} = 0.0985\ (\mu g/mL)^{-1}$, and represents the maximum sensitivity value for the largest prestrain, $e/e_{1/2} = 1.89$.

e (ppt)	$e/e_{1/2}$	G_0 (mS)	Γ	$C_{1/2}$ (μg/mL)	R^2	S_0 (μg/mL)$^{-1}$
0.0	0.00	181	4.256	41.971	0.998	0.0015
25.2	0.81	132	3.137	29.349	0.999	0.0049
32.0	1.03	84.6	3.133	21.969	0.999	0.0065
38.3	1.23	43.0	2.470	15.895	1.000	0.0144
44.2	1.42	19.3	2.688	12.799	0.999	0.0153
48.9	1.57	9.40	2.375	9.837	0.993	0.0248
55.0	1.76	3.60	1.768	7.503	0.997	0.0485
58.8	1.89	1.90	1.310	5.275	0.967	0.0918

Table 9-1. Processed experimental data corresponding to the response curves in Figure 9-4a.

The semi-log plot in Figure 9-5 shows that the initial sensitivity increases super-exponentially with tensile strain. Even very small tensile strains result in substantial increases in FSCR initial sensitivity—as much as 63-times that of the unstrained sensor. We evaluated the noise in the FSCR baseline conductance for both the unstrained and maximally strained ($e/e_{1/2} = 1.89$) states, and obtained standard deviations of $\sigma_{G_0}(e/e_{1/2} = 0) = 2.465 \times 10^{-4}\,\mathrm{S}$ and $\sigma_{G_0}(e/e_{1/2} = 1.89) = 2.976 \times 10^{-6}\,\mathrm{S}$. Using initial sensitivity values from Table 9-1 and Eq. 9-5, we calculate the *LDL*s as 2.80 and 0.051 μg/mL toluene respectively. This is a ~ 55-fold decrease in the FSCR's *LDL* between these strained and unstrained states. The difference between the values for the change in sensitivity versus the change in *LDL* is a result of the variation in the noise in the conductance baseline signals between the two states, which the initial sensitivity calculation does not take into account. Of course, standard noise reduction techniques

could be used to increase the sensor sensitivity (modulation of the applied dc voltage, signal averaging, etc.), but here we are only trying to convey the relative increase in sensitivity due to tensile strain.

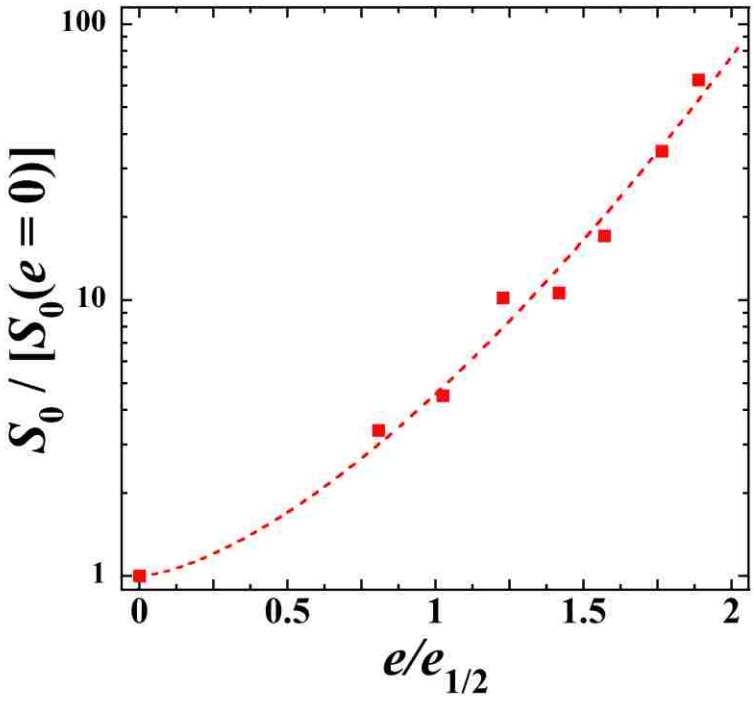

Figure 9-5. Relative initial FSCR sensitivity, $S_0 / S_0(e = 0)$, as a function of relative prestrain, $e/e_{1/2}$, where S_0 is the initial sensitivity at a particular prestrain value, $S_0(e = 0)$ is the initial sensitivity of the sensor in the unstrained state, and $e_{1/2}$ is the response midpoint strain from Figure 9-3. The semi-log plot of these data illustrates a super-exponential dependence of initial sensitivity on prestrain. The maximum prestrain value tested in this experiment yields a 63-fold increase in initial sensitivity compared to the unstrained sensor.

9.6. Magnetochemiresistance

In addition to mechanical stretching, FSCRs can also be strained by the application of a magnetic field. In a previous paper, we have demonstrated that field-structured composites exhibit significant magnetostriction—on the order of 10,000 ppm strain in a saturating field. This is on the order of five times larger than the maximum strains

achieved with Terfenol-D.[47] This property provides a way to generate a controllable compressive stress parallel to the chains, which should alter sensor sensitivity. The contraction of the particle chains in an applied field increases their contact pressure and thus increases their conduction. Subsequently, there must then be an increase in analyte induced swelling to overcome this increased contact pressure and reduce conduction. We call this effect magnetochemiresistance, since the FSCR responds to the dual inputs of a magnetic field and a chemical vapor.

The result of this experiment is shown in Figure 9-6 for an FSCR exposed to 10.8 $\mu g\ mL^{-1}$ toluene and a modest and uniform magnetic induction field of 0.12 T, produced by a Helmholtz pair. As Figure 9-6 shows, the negative magnetoresistance is quite large; here, the field increases the conductance by six orders of magnitude as the sensor reaches steady state swelling. Magnetochemiresistance could be used to dynamically control the chemical response of the sensor, or a pre-strained sensor could be used as a simple magnetic field sensor.

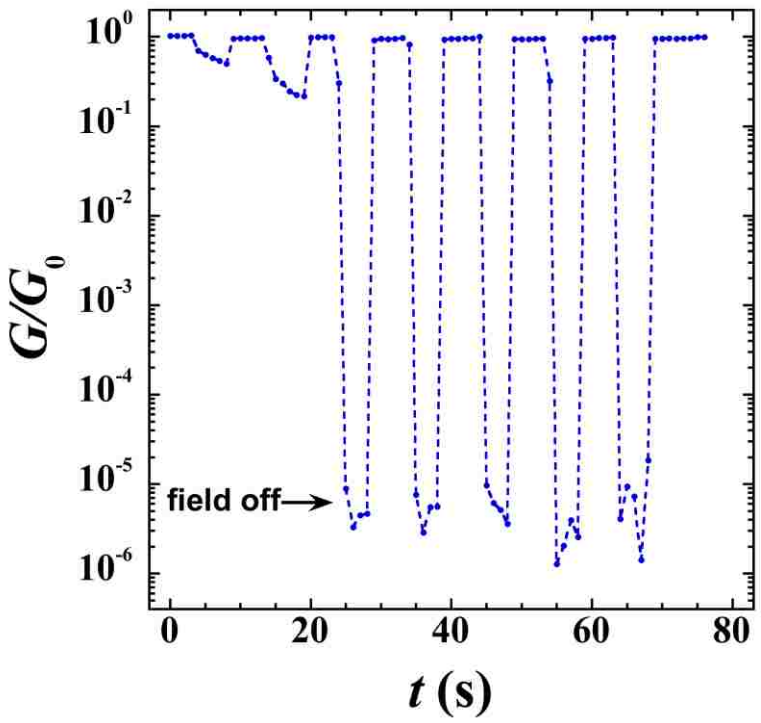

Figure 9-6. A dc magnetic field of 0.12 T is periodically applied to an FSCR exposed to 10.8 μg/mLtoluene as it approaches its steady-state swelling. As the chemiresistor conductance drops, the negative magnetoresistance becomes quite large, because the magnetic field creates dipolar interactions that draw the particles back into contact. These data were taken by G. Gulley and J. Martin.

9.7. Conclusions

We have shown that applying a tensile strain to an FSCR can significantly increase its chemical sensitivity, especially at low analyte concentrations, resulting in a ~55-fold decrease of the LDL. This technique enables the development of chemiresistors that can be dynamically tuned with an actuator to optimize their sensing range and sensitivity to the analyte concentrations to be measured. This results in a sensing system that is highly sensitive and has a wide sensing range—characteristics that are in opposition for any fixed response curve. Although chemiresistors certainly have an application niche, lack of sensitivity has previously been a major drawback to this technology.[5,6] The increased

sensitivities we have demonstrated greatly expand the usefulness of chemiresistors. Lastly we showed that an FSCR can be compressively strained by application of a magnetic field. This magnetostriction could be used as an additional means to dynamically control the response of the sensor to an analyte, or conversely a chemiresistor could be used as a simple magnetic field sensor.

10. THE MASTER TRANSDUCTION CURVE

***Abstract*—**In the presence of an analyte that is compatible with the polymer phase, the sensor conductance decreases as the analyte is absorbed, eventually reaching a steady-state value that is a measure of the analyte's concentration. The response curve, which is the relationship between steady-state conductance and analyte activity (normalized concentration), is strongly dependent on both the chemical affinity of the analyte for the polymer, *and* the stress field within the chemiresistor composite. Calibration of an individual sensor would seem to necessitate mapping out the response curve for each analyte of interest—a tedious and expensive proposition. We show that the transduction curve of any particular sensor is a function of polymer swelling *alone*, regardless of the chemical nature of the analyte. This *master transduction curve* implies that sensor calibration requires only a knowledge of the polymer mass-sorption isotherm for any set of analytes of interest—data that can be collected once and for all. Any single analyte can then be used to calibrate the response of a particular sensor as a function of analyte activity, and the response to other analytes can be predicted. As a corollary, a calibrated sensor can be used to determine the mass-sorption data for any other analyte of interest. In this chapter we provide a detailed description of the construction of the master transduction curve, show how this curve can be used to measure polymer sorption with a calibrated chemiresistor, and demonstrate the use of a single analyte to calibrate sensors of disparate sensitivities and predict their response to two other analytes.

10.1. Introduction

As we have shown in Chapters 6–9, the stability and reversibility of these sensors has enabled us to identify polymer stress as the key variable that governs chemiresistor sensitivity. An increase in the stress reduces the sensitivity, and this increase can be achieved either by elevating the polymer cure temperature or curing the polymer with a certain amount of added swelling agent that is later volatilized. A decrease in the stress increases the sensitivity, and this could be effected by swelling the cured polymer with a nonvolatile chemical that might even bond to the polymer, or as we demonstrated in the previous chapter, by applying a tensile strain to the sensor. By these means, sensor sensitivity can be altered by as much as 2–3 decades. Response tailorability makes sensor calibration an important issue and raises a critical point: Does stress *homogeneously* alter sensor sensistivity to various analytes? In other words, is any relative change in sensitivity the same for all analytes? If polymer stress alters the affinity of analytes for the polymer phase, then stress might *inhomogeneously* affect its sensitivity to various analytes. This would imply that sensors of differing sensitivities would have to be calibrated with the full set of analytes of interest. On the other hand, if polymer stress does not significantly affect chemical affinities, then it must affect *only* the relationship between polymer swelling and sensor conductance, and one would then expect stress to homogeneously alter sensor sensitivity. In fact, in this chapter we show that the response of an FSCR is a function of polymer swelling *alone*, such that a plot of conductance versus swelling makes an analyte-independent master transduction curve.

The existence of this master curve implies that any particular sensor can be calibrated with just a single analyte. From this single calibration curve the response of the sensor to

other analytes can be predicted from their relative mass-sorption data. These mass-sorption data can be collected once and for all, using either traditional gravimetric techniques, or using a calibrated FSCR.

In this paper we describe in detail the mass-sorption and sensor response measurements required to construct an accurate master transduction curve. This master curve is then used to determine the Flory parameters[40–42,50] of a variety of other analytes at high polymer concentration, using only this calibrated chemiresistor. Finally, three chemiresistors of various sensitivities are calibrated with just a single analyte, and their responses to other analytes are predicted from our measured Flory parameters. Measurements on these model analytes demonstrate the accuracy of the predictions.

10.2. Experimental

10.2.1. CHEMIRESISTOR FABRICATION.

For this experiment we use a typically fabricated FSCR with 15 %vol. Au-coated Ni encapsulated in the Gelest OE41 PDMS and structured in a 650 gauss uniaxial magnetic field and cured at 55 °C.

10.2.2. MATERIALS

The analytes studied are the aromatic, hydrophobic compounds toluene, *p*-xylene, and mesitylene and the hydrophilic compounds acetone and *n*-propanol. These analytes were obtained from Sigma-Aldrich (ReagentPlus grade). The aromatic VOCs are chemically similar (phenyl ring with 1, 2, and 3 methyl groups) and so have similar solubility

parameters. They, however, vary considerably in their volatility, as evidence by their saturation vapor pressures at 25°C (29.0, 8.8, and 2.55 Torr respectively).[53]

10.2.3. SORPTION ISOTHERMS

To determine the Flory parameter for an analyte-polymer, pair it is necessary to measure the amount of analyte absorbed into the polymer at fixed temperature and analyte activity, a. This analyte activity is defined as the ratio of the vapor pressure of the analyte to its saturation vapor pressure. To reach equilibrium in a short time it is necessary to use thin polymer films, so mass-sorption isotherms have traditionally depended on Quartz Crystal Microbalances (QCM) and Surface Acoustic Wave (SAW) devices.[7,25] These devices have in fact been used to correlate mass-sorption with various types of chemiresistor composites.[51–54] We initially resorted to a QCM, but inconsistencies between the data and theory suggested that factors other than mass-sorption were affecting the measurements for our particular system.

The Sauerbrey equation, which relates the change in frequency of the piezoelectric crystal to the change in mass deposited onto the crystal, is generally used for frequency changes of less than 2% and requires that the deposited film is uniform, rigid and thin.[55] Under these conditions QCM data can be easily interpreted to determine the absorbed mass. When these assumptions are invalid, the more complicated Z-match equation, which accounts for the film's shear modulus, must be used.[23] However, errors arise from the Z-match equation when using polymer films that exhibit strong viscoelastic behavior, such as elastomers. These errors are in turn compounded when the viscoelastic properties of the polymer change with increasing absorption of the

analyte, as they inevitably do.[56–59] The resultant sorption data are then due to both the analyte mass-sorption *and* the change in polymer viscoelasticity.

It is also uncertain if the thin polymer film needed for QCM experimentation has the same absorption properties as the bulk polymer. When considering a thin polymer film (300 nm), substrate interface interactions must be taken into account. A thin film strongly adhered to the quartz surface may have additional surface forces that retard the swelling of the polymer and interfere with crosslinking and gelation in comparison to bulk.[60] In addition, FSCRs are made of relatively thick polymer films (~150 μm) in order to fully encapsulate the particle network, therefore it is desirable to make the mass-sorption measurements on films of comparable thickness to minimize both surface effects and possible chemical differences. These measurements were made with a highly stable Mettler-Toledo ultra-microbalance (model UMX2) capable of detecting mass changes as low as 100 ng. This limiting value is less than 0.1% of the typical mass uptake we measured.

The flowcell is a capped stainless steel cylinder with an inlet for the nitrogen/analyte stream and a hole of the same diameter drilled into the side for the outlet. The flowcell sits on an O-ring and envelops the entire weigh pan assembly of the ultra-microbalance (described below). Glass fiber is placed and secured to the inlet hole to diffuse the gas stream entering the chamber in order to minimize pressure effects on the weigh pan. The ultra-micobalance and sorption flowcell are shown in Figure 10-1.
The mass-sorption measurements take much longer than those of typical sensor response. Because of this the bubbler system was used so the entire sorption cycle could be automated, which is impractical using the vial flow system. The absorption and purge

stages are considered to be complete when a constant sample mass is achieved. The result of a typical mass-sorption cycle is shown in Figure 10-2. Total flow rate is kept constant throughout all stages to prevent systematic errors caused by the slight flow pressures on the microbalance weigh pan.

Figure 10-1. The Metler UMX-2 ultramicrobalance has a resolution of 100 ng and is used to directly measure the mass of analyte absorbed into the polymer film. The flowcell is a capped stainless steal cylinder, which envelopes the weigh-pan assembly.

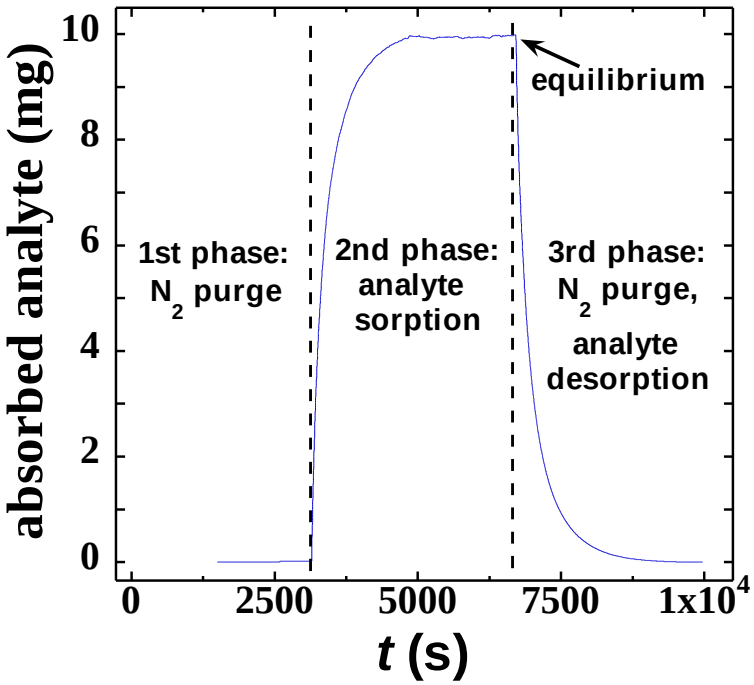

Figure 10-2. Typical kinetic gravimetric data for the mass-sorption of *p*-xylene into silicone.

10.3. Results and Discussion

10.3.1. SORPTION ISOTHERMS

Mass-sorption isotherms for each of the five analytes are shown in Figure 10-3. These isotherms can be interpreted in terms of the Flory–Huggins theory, which we recall relates the swelling of a polymer to analyte activity:[40–42]

$$\ln a = \ln \phi + (1-\phi) + \chi(1-\phi)^2. \qquad \textbf{(10-1)}$$

Here ϕ is the volume fraction of absorbed analyte and χ is the Flory parameter, which is the interaction energy for the particular polymer-solvent system. In the regime where

both ϕ and the analyte activity are small, the Flory–Huggins equation reduces to the linear equation, $\phi = a/e^{\chi+1}$, so large values of χ give low swelling. Literature values of χ are available for many polymer-solvent systems, and can even be roughly estimated from the Laar–Hildebrand equation.[50] But these values generally apply to dilute polymer solutions,[61] so we have measured our χ-values.

The homologous, hydrophobic aromatics are found to have similar χ-values, in the range of 1.25–1.42. The hydrophilic analytes, however, have much less affinity for the polymer and have much higher χ-values, such as 3.37 propanol. Table 10-1 contains the slopes from the linear fits to the data in Figure 10-3, as well as the calculated χ parameters. All of these χ-values are much larger than 0.5, which is the value associated with the so-called *theta solvent*, where the solvent-mediated steric repulsion and van der Waals attractions between monomers cancel. In so-called *poor solvents* the van der Waals attractions dominate and χ-values are larger than 0.5. Poor solvents can cause phase separation for polymer solutions at concentrations near the critical concentration, which is generally quite low as it is inversely dependent on the polymer molecular weight. However, these issues are not a concern here, as the high χ-values do not induce phase separation, but simply limit swelling of the cross-linked polymer. For large values of χ the maximum swelling is approximately $\phi_{max} = 1/e^{1+\chi}$, so for $\chi = 3$ this is about 2 vol.%.

The χ parameter can be strongly dependent on polymer concentration—an inconvenient fact that undermines the utility of χ. For example, Errede reports that for poly (dimethylsiloxane) the χ-value for benzene increases linearly with polymer volume

fraction from a low of 0.5, indicative of a theta solvent, to a high of 0.85, a poor solvent.[61] Values for toluene are similar. The high χ-values we report do not therefore necessarily imply that the solvents we test are poor solvents for the dilute polymer. In fact, Errede shows that for poly(isopropene) the χ-value for methyl ethyl ketone increases from 0.4 (a good solvent) in the dilute polymer limit to 1.5 at high polymer concentration.

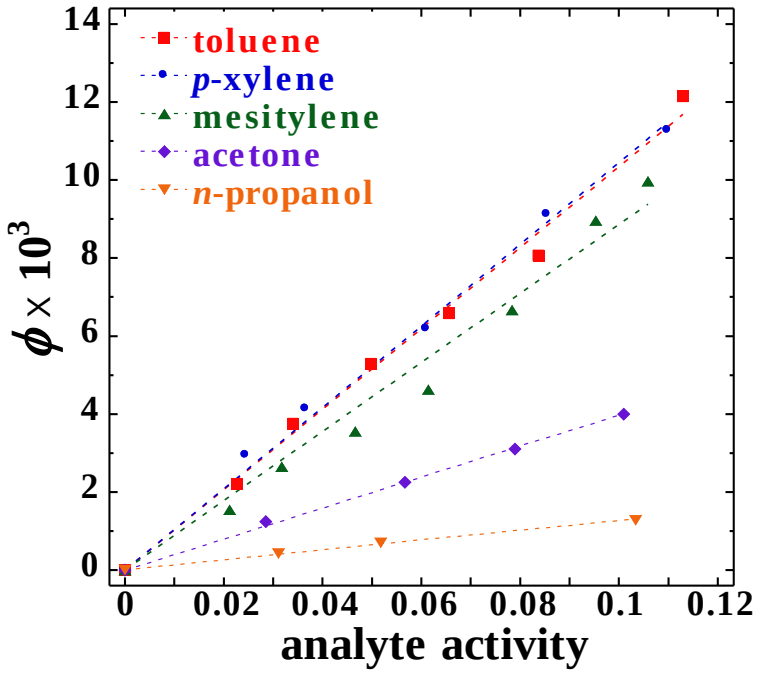

Figure 10-3. The Flory–Huggins sorption isotherms demonstrate a linear relationship between volume fraction of absorbed analyte, ϕ, and analyte activity, a. These data are fit with $\phi = k\,a$, the results for which are in Table 10-1.

Table 10-1. Flory parameters from mass-sorption isotherms in Figure 10-3.

analyte	***k***	R^2	χ
toluene	0.104	0.993	1.26
p-xylene	0.105	0.996	1.25
mesitylene	0.089	0.979	1.42
acetone	0.040	0.999	2.22
n-propanol	0.013	0.996	3.37

Although, for simplicity, we use the Flory-Huggins equation (FHE) to determine the χ parameters from experimental mass-sorption data, this equation does not take into account the entropy change due to swelling a crosslinked polymer. The Flory-Rehner equation (FRE) is essentially the Flory-Huggins equation with this additional term and is written as

$$\ln a = \ln \phi + (1-\phi) + \chi(1-\phi)^2 + V_s \cdot \nu_c \left[(1-\phi)^{1/3} - (1-\phi)/2\right] \qquad \textbf{(2)}$$

where V_s is the analyte molar volume and ν_c is the crosslink density. The young's modulus for our elastomer is ~0.8 MPa, which corresponds to a crosslink density of 3.23 x 10^{-4} mol/mL. Figure 10-4a below compares a mass-sorption curve calculated from the Flory-Rehner equation to that calculated from the Flory-Huggins equation using a χ value of 1.25 (that for xylene). Here we see a small departure between the two curves at high analyte concentration, but in the activity range where FSCRs typically operate these two curves are nearly indistinguishable. Figure 10-4b below shows that the mass-sorption curve calculated from the FRE with a χ of 1.23 matches that calculated from the FHE and

a χ of 1.23. The difference in these χ values is 1.6%. Although this small error is not troublesome for our analytes and polymer system, it may be necessary to use the Flory-Rehner equation when considering a polymer with a high crosslink density.

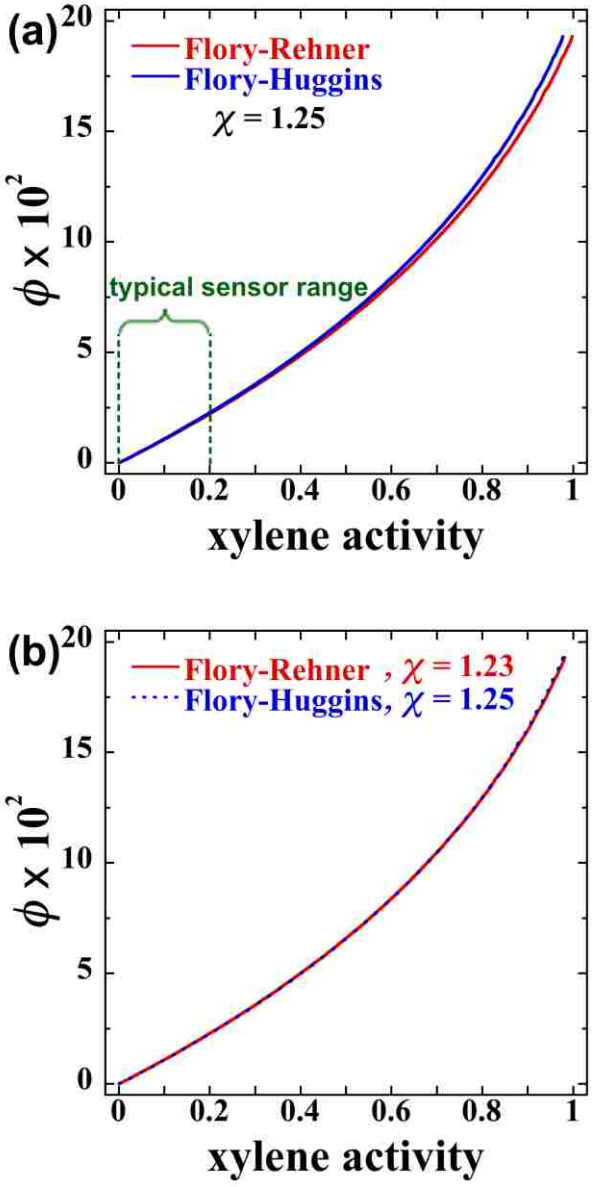

Figure 10-4. (a) The comparison between a mass-sorption curve calculated from the Flory-Rehner equation and that calculated from the Flory-Huggins equation using a χ value of 1.25 shows a small departure between the two curves at high analyte activity. However, in the activity range where FSCRs typically operate these two curves are nearly indistinguishable. **(b)** The mass-sorption curve calculated from the FRE with a χ of 1.23 matches that calculated from the FHE and a χ of 1.23, which corresponds to 1.6% error.

10.3.2. SENSOR RESPONSE

Many detectors have a linear, or proportional, relationship between the analyte concentration and the steady-state response.[51] FSCRs have a super-linear relationship that makes them function more like chemical switches, changing from charge conductors to insulators over a narrow range of analyte concentration. Before presenting the response data that we collected for the series of five analytes, it is helpful to revisit the form of the FSCR response.

Again and for continuity, the response curve for our sensors is given by

$$\frac{G}{G_0} = \left[1 + \frac{e^{\Gamma a / a_{1/2}} - 1}{e^{\Gamma} - 1}\right]^{-1}. \qquad \textbf{(10-3)}$$

where Γ is a fitting parameter whose value (typically 2–7) is determined by the abruptness of the conductor-insulator transition, and $a_{1/2}$ is the *response midpoint*, which is the activity that reduces sensor conductance by half.

Measurements of the response of an individual PDMS-based field-structured chemiresistor are shown in Figure 10-5 for each analyte. This sensor has high sensitivity to the hydrophobic compounds, lower sensitivity to acetone and still lower sensitivity to *n*-propanol. Figure 10-5 contains the constants, Γ and $a_{1/2}$, obtained by fitting the response data to Eq. 10-3.

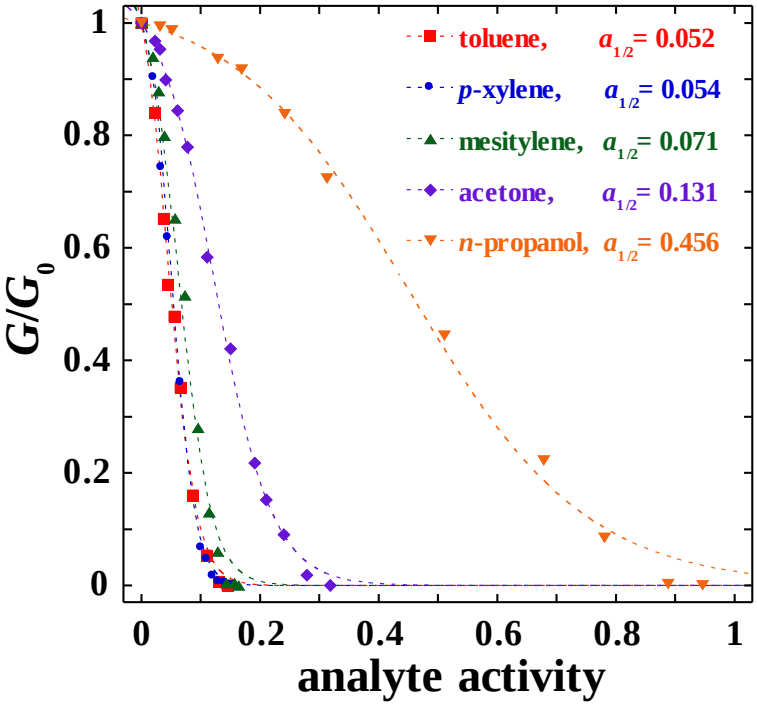

Figure 10-5. Response curves for a single PDMS-based FSCR exposed to the various analytes. The sensor has high-sensitivity to the hydrophobic aromatic analytes and has lower sensitivity for the more hydrophilic compounds, acetone and *n*-propanol. Here, the sensor covers nearly the entire range of *n*-propanol activity, but at the cost of reduced sensitivity. The legend contains the response midpoint for each analyte from the fit of these data to Eq. 10-2.

10.3.3. THE MASTER TRANSDUCTION CURVE.

Polymer swelling is related to activity via the mass-sorption isotherms and the linearized Flory–Huggins equation, $\phi = a/e^{1+\chi}$. In terms of the analyte volume fraction in the polymer, the response curve is simply

$$\frac{G}{G_o} = \left[1 + \frac{e^{\Gamma \cdot \phi/\phi_{1/2}} - 1}{e^{\Gamma} - 1}\right]^{-1}, \qquad \textbf{(10-4)}$$

where $\phi_{1/2} = a_{1/2}/e^{1+\chi}$. In this form the response data for all analytes fall onto the master curve in Figure 10-6, demonstrating that the response of any individual FSCR is a function of polymer swelling alone. This data collapse is physically reasonable for analytes that do not interact with the Au-passivating layer on the magnetic particles, but such ideal behavior would not be expected for thiols, tertiary amines, or other ligands that bind strongly to Au as we have previously demonstrated in Section 7.4. Likewise, a master transduction curve would not be expected for carbon black chemiresistors, due to the generally strong adsorption of organics to carbon black.

Because this master curve is analyte independent, it can be determined by any single analyte having a known χ parameter. The response to any other analyte can then be predicted from this experimentally determined transduction curve and *its* χ parameter. This χ parameter might be tabulated in the literature, or it can be determined once and for all from either mass-sorption measurements, or from a calibrated sensor, as we demonstrate below.

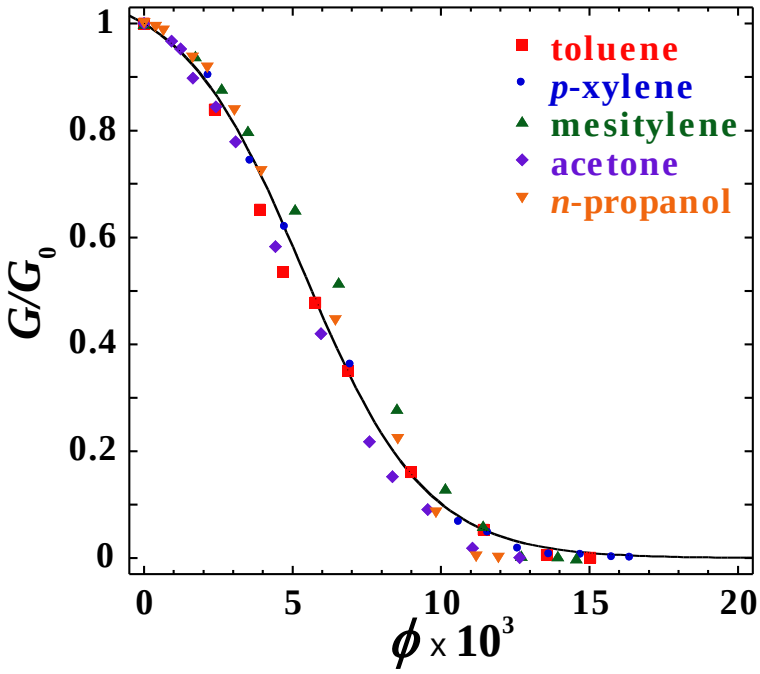

Figure 10-6. Sensor response, G/G_0, is shown to be a universal function of volume fraction of absorbed analyte, ϕ. The fit of these data to Equation 3 with $\Gamma = 2.75$ yields the swelling response midpoint of $\phi_{1/2} = 5.644\times10^{-3}$ with $R^2 = 0.991$.

10.3.4. ROLE OF STRESS

To demonstrate the role of stress in sensor response, we fabricated sensors at cure temperatures of 25 and 85°C. The data in Figure 10-7a show that the sensor made at 25°C has about ten-times the sensitivity of the sensor cured at the higher temperature. As stated in Section 8.3., this is due to the polymer's coefficient of thermal expansion (CTE) being substantially larger than that of the particles, resulting in large compressive stresses upon cooling the 85°C cured sensor.[2,3] We recall from above that there are two possible origins for this stress effect: a change in the mass-sorption isotherm, or a change in the transduction curve. Mass-sorption measurements on polymer films cured at these two temperatures, Figure 10-7b, demonstrate that these CTE stresses have no measurable

impact on mass-sorption, and thus χ. Therefore, compressive polymer stress actually alters the transduction curve itself, by increasing the contact pressure between the particles. Increased polymer swelling is then required to reduce this pressure to the point where the contact resistance increases. In fact, as we have shown in Chapters 4–9, alleviating these compressive stresses can increase sensor sensitivity by as much as 60-fold.

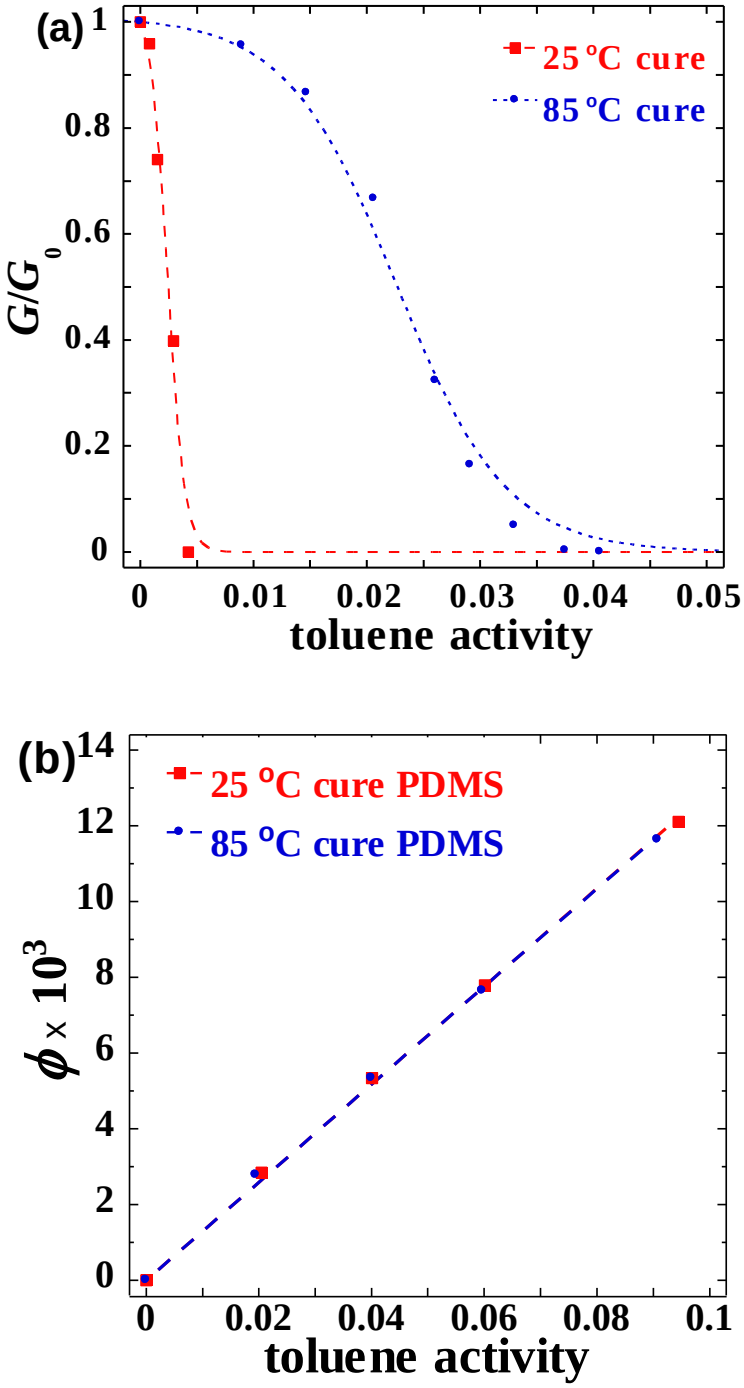

Figure 10-7. **(a)** Response curves for two FSCRs cured at different temperatures illustrate the effect of compressive stresses within the composite. The polymer cured at higher temperature has significant cool-down stresses, due to the large mismatch in the CTEs of the polymer and particle phases. **(b)** Mass-sorption experiments show that stress does not change the mass-sorption isotherm, implying that stress alters the transduction curve of the sensor without altering its affinity for the analyte.

10.3.5. MEASURING THE FLORY PARAMETER WITH AN FSCR

Although mass-sorption measurements are traditionally used to determine χ, it is also possible to use a calibrated FSCR for this task, which is actually a faster and simpler approach. To do this we calibrated a newly fabricated sensor with analytes for which we measured χ gravimetrically (i.e. toluene, *p*-xylene, mesitylene, and acetone). The resultant transduction curve is the solid line in Figure 10-8. We then determined the response of this sensor to the pentane, octane, decane, undecane, 4-tert-butyltoluene, and trimethyl phosphate, for which the χ-values are unknown. These response curves were then collapsed onto the transduction curve using the relation $\phi_{1/2} = a_{1/2}/e^{1+\chi}$. The resulting χ-values in Table 10-2 show a relatively low value of 0.77 for pentane, similar values for the other alkanes, and a very large value of 3.24 for the phosphate. The low value for pentane was subsequently confirmed in direct mass-sorption measurements. The characterization of a response curve can take as little as 1–2 hours (and ~15 minutes for a single point), so this is an efficient method for determining χ that negates the need for an expensive microbalance or QCM.

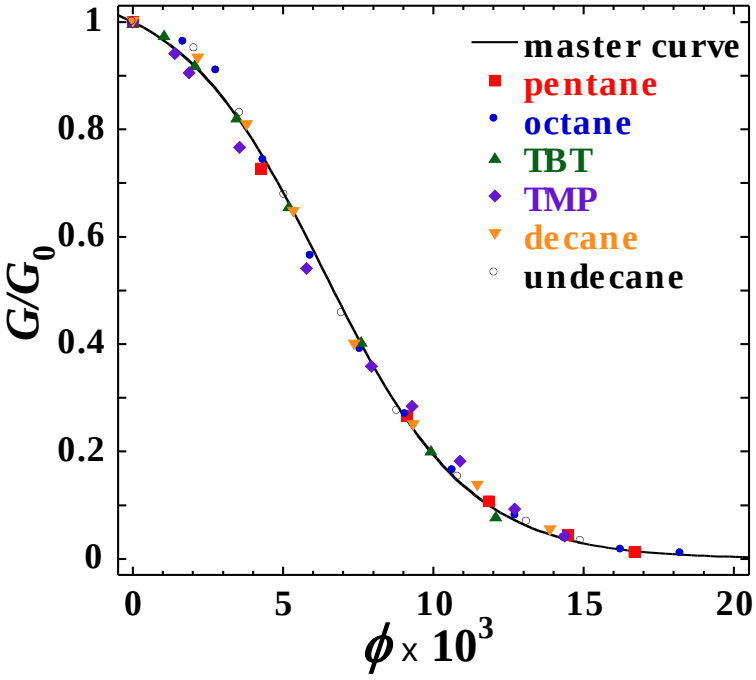

Figure 10-8. The master curve for a newly fabricated FSCR was formed using response and mass-sorption data for toluene, *p*-xylene, mesitylene, and acetone. For this sensor, $\phi_{1/2} = 6.68\times10^{-3}$ and $\Gamma = 2.77$. The response of this sensor to several analytes was subsequently determined and χ-values (reported in Table 9-2) were calculated from $\chi = \ln a_{1/2} - \ln \phi_{1/2} - 1$.

analyte	$a_{1/2}$	χ
pentane	0.039	0.77
octane	0.059	1.17
decane	0.055	1.11
undec	0.060	1.19
4-tert-butyltoluene	0.072	1.38
trimethyl phosphate	0.464	3.24

Table 10-2. Midpoint response and χ values obtained from the sensor response data in Figure 10-7.

10.3.6. SINGLE ANALYTE CALIBRATION

To demonstrate the calibration of sensors of significantly different sensitivities with a single analyte, we fabricated three sensors at cure temperatures of 40, 50 and 90 °C. The response of each of these sensors to acetone was determined and their master curves computed using the measured χ-value of 2.22 (see Table 10-1). These master curves show that the response midpoint of the sensor cured at 90 °C occurred at a volumetric swelling of 2.30%, whereas the values for the 50 and 40 °C sensors were 0.97 and 0.47%, respectively.

For each of these three sensors the response curve for toluene ($\chi = 1.26$) and trimethyl phosphate ($\chi = 3.24$) were predicted from the master curve, with the results shown in Figures 10-9(a–c) and Table 10-3. The actual measurements of the response to these analytes are compared to these predictions, and the agreement is sufficiently good to illustrate the single-analyte calibration principle. Of course, the agreement might be better if the master curve was constructed with more than a single analyte, to reduce uncertainties in the data.

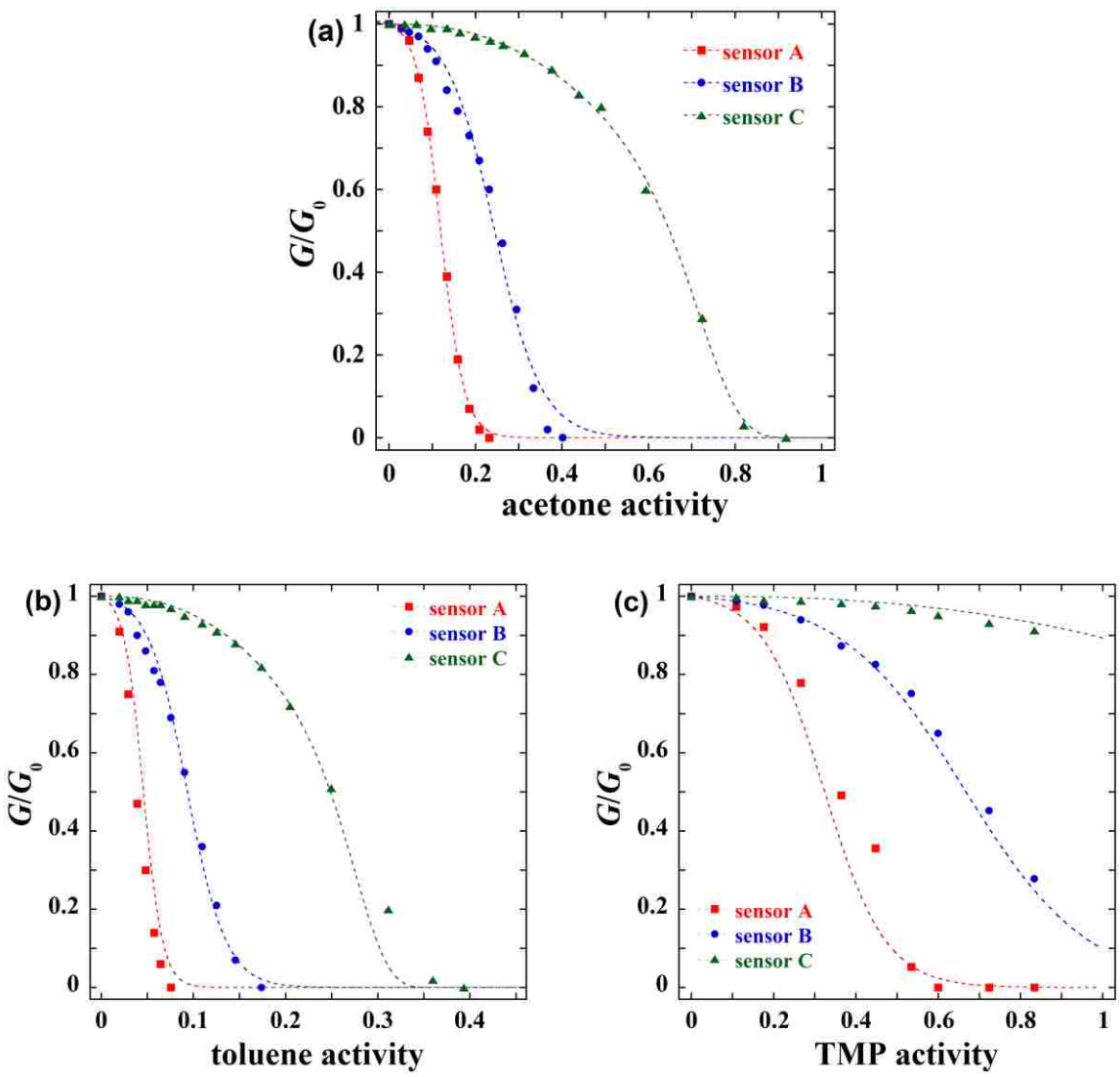

Figure 10-9. (a) Three FSCRs (A,B, and C) were cured at 40, 50, and 90 °C, respectively, which results in a range of sensitivities. Sensor response to acetone was determined and fit to Eq.10-3 (dashed curves). The resultant parameters Γ and $a_{1/2}$ and the experimental χ-value of 2.22 for acetone (Table 10-1) were used to construct the master transduction curve for each sensor. **(b)** The predicted response of the sensors to toluene (dashed curves) is calculated using the acetone-calibrated master curves and the χ-value of 1.26 for toluene. Co-plotting these predicted curves and actual response data to toluene shows excellent agreement. **(c)** Sensor response is now predicted for trimethyl phosphate (TMP) (dashed curves) using the master curves and the χ-value for TMP of 3.24 from Table 10-2. Recall that the sorption isotherm for TMP is not directly measured, but is instead calculated from the master curve and the TMP response data in Figure 10-9. However, this indirect method for obtaining χ, yields excellent prediction of FSCR response. Values for response characterization of the sensors are reported in Table 10-3.

sensor	T_{cure} (°C)	Γ	$a_{1/2}$ acetone	$\phi_{1/2}$	$a_{1/2}$ toluene	$a_{1/2}$ TMP
A	40	4.413	0.119	0.00474	0.046	0.329
B	50	4.455	0.244	0.00969	0.094	0.672
C	90	6.291	0.649	0.02292	0.249	1.546

Table 10-3. Response curve constants for the three sensors shown in Figure 10-8 were determined using acetone and were calculated to predict the response to toluene and TMP.

10.3.7. LAAR-HILDEBRAND THEORY

When χ cannot be directly obtained from literature it can be estimated using a semi-empirical method such as the van Laar-Hildebrand equation:

$$\chi = \chi_s + \frac{V_1}{RT} \cdot (\delta_1 - \delta_2)^2. \qquad \textbf{(10-5)}$$

Here δ_1 and δ_2 are the Hildebrand solubility parameters for the analyte and polymer phases, and V_1 is the analyte molar volume. χ_s is the entropic contribution to the Flory parameter, which is usually between 0.3–0.5 and Bueche finds is 0.39 for PDMS. Hildebrand solubility parameters are tabulated for many solvents and polymers,[50] so this equation is useful for roughly estimating χ, but we find it is not a direct substitute for a mass-sorption measurement.

10.4. CONCLUSIONS

Through mass-sorption and sensor response measurements it can be shown that FSCR response is a universal function of polymer swelling alone. A master transduction curve (conductance versus swelling) for an individual sensor can thus be determined from experiments with a single analyte, and this curve can then be used to predict the response

curve (conductance versus analyte activity) for any other analyte, provided its relative affinity for the polymer is known. This relative affinity can be determined once and for all from mass-sorption measurements, measured either gravimetrically or by the sensor itself. The calibration of FSCRs is greatly simplified in this way, since any individual sensor can be calibrated with a single analyte. Finally, we have made sensors of disparate sensitivities by curing at three different temperatures. These sensors were calibrated with acetone and their response to toluene and trimethyl phosphate were determined. The measured response to these analytes was found to be in agreement with the predictions.

11. ANALYTE DISCRIMINATION FROM FSCR RESPONSE KINETICS

***Abstract*—**Like other polymer-based gas sensors that function through sorption, chemiresistors are selective for analytes based on the affinity of the analyte for the polymer. However, a single sensor cannot, in and of itself, discriminate between analytes, since a small concentration of an analyte that has a high affinity for the polymer might give the same response as a high concentration of another analyte with a low affinity. In this chapter we use field-structured chemiresistors to demonstrate that their response kinetics can be used to discriminate between analytes, even between those that have identical chemical affinities for the polymer phase of the sensor. The response kinetics is shown to be independent of the analyte concentration, and thus the magnitude of the sensor response, but is found to vary inversely with the analyte's saturation vapor pressure. Saturation vapor pressures often vary greatly from analyte to analyte, so analysis of the response kinetics offers a powerful method for obtaining analyte discrimination from a single sensor.

11.1. INTRODUCTION

Polymer sorption is the basis of most simple methods of sensing vapors of volatile organic compounds. Such devices (detailed in Chapter 2) include quartz crystal microbalances and surface acoustical wave sensors that transduce mass sorption into a frequency change, and sensors that transduce mass uptake into a resistance or capacitance change, such as chemiresistors, chemicapacitors and CHEMFETs. Regardless of the

sensing mechanism, each individual sensor, being comprised of a single polymer, cannot discriminate between analytes if only the equilibrium mass uptake is used, unless somehow the partial pressure of the analyte is either known or measured. For these polymer-based sensors, analyte discrimination is currently based on the artificial nose concept (see Section 2.3.2), wherein arrays of sensors having differentiating chemical affinities are exposed to the vapor. Any analyte will then give a more-or-less unique relative equilibrium mass uptake to the array elements, generating a response fingerprint. This equilibrium approach can enable the discrimination of analytes having disparate chemical affinities, but will not be as useful for distinguishing homologous analytes, such as octane from decane, or xylene from mesitylene. The ability to distinguish between homologous analytes requires nonequilibrium information.

In this paper we use field-structured chemiresistors to show that polymer sorption kinetics enables discrimination between even homologous analytes. In the previous chapter we showed that the basis for this discrimination derives from Flory-Huggins theory, which states that for analytes having the same chemical affinity for a particular polymer, the analyte's equilibrium mass sorption is determined by the analyte activity alone.[40–42] We recall that this chemical affinity is quantified by Flory-Huggins parameter, χ, and activity is defined as the ratio of the analyte vapor pressure to its saturation vapor pressure, or $a = p/p^*$. For linear alkanes the saturation vapor pressure decreases by about a factor of three for every additional carbon, so at the same activity octane vapor will have roughly ten times the number density of molecules as decane, yet will lead to about the same equilibrium polymer swelling. The flux of the analyte into the polymer is proportional to its diffusivity times its number density, so swelling will be

roughly ten times faster for octane than for decane, provided their diffusivities are similar. To first approximation, the characteristic swelling rate should simply be proportional to the analyte's saturation vapor pressure.

This swelling time is expected to be independent of the analyte's concentration. This is because when in the linear swelling regime (a valid assumption for most vapor detection applications), twice the analyte vapor pressure gives twice the swelling, yet also gives twice the number density of analyte molecules, and thus twice the diffusive flux. A swelling time that is independent of the analyte concentration is highly desirable, since it would simplify the interpretation of kinetic data. In fact, the raw data we collect are sensor response versus time, so the response must be converted to polymer swelling before the swelling time can be computed. This is accomplished using the transduction curve of the particular chemiresistor, which is the relation between its change in conductance and equilibrium swelling. In the previous Chapter 10 we have shown that this transduction curve is analyte independent, and so can be determined from testing the chemiresistor with any particular analyte, regardless of its affinity for the polymer.

11.2. Background

11.2.1. TRANSDUCTION CURVE

In the previous chapter we have shown that the response of a FSCR is a universal function of polymer swelling, regardless of the chemical nature of the analyte. The response curves in Figure 11-1 can thus be thought of as a combination of a solely device-dependent transduction curve **(**conductance as a function of swelling**)** and the solely analyte-dependent mass-sorption curve that relates swelling to the vapor

concentration. The transduction curve for a typical sensor is shown in Figure 11-2, with the volume fraction of absorbed analyte determined gravimetrically. Again, this curve is given by

$$\frac{G}{G_0} = \left[1 + \frac{e^{\Gamma\phi/\phi_{1/2}} - 1}{e^{\Gamma} - 1}\right]^{-1}, \qquad \textbf{(11-1)}$$

where ϕ is the volume fraction of absorbed analyte and $\phi_{1/2}$ is the response midpoint. The transduction curve is parameterized by $\phi_{1/2}$ and Γ and as we have shown in Chapters 6–8, these are strongly dependent on the fabrication process used to make the sensor. To a good approximation the equilibrium sorption is proportional to analyte activity a and is given by the linearized Flory-Huggins equation,

$$\phi = ae^{-(\chi+1)}. \qquad \textbf{(11-2)}$$

This transduction curve is of great importance in this chapter, as we will use it to convert non-equilibrium response curves such as that in Figure 11-3 into the non-equilibrium sorption curves from which we obtain kinetics data.

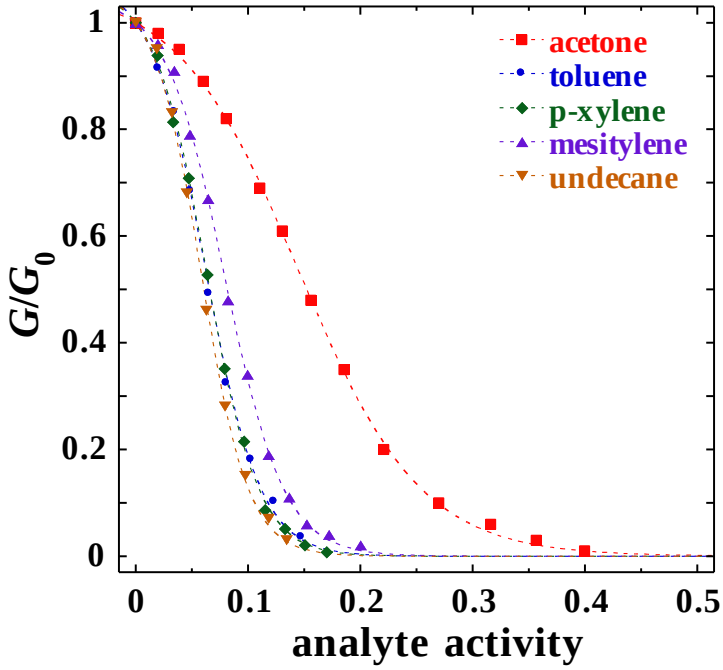

Figure 11-1. Response curves for a single FSCR exposed to various analytes illustrates selectivity for more hydrophobic analytes. These equilibrium data do not discriminate between chemically similar analytes.

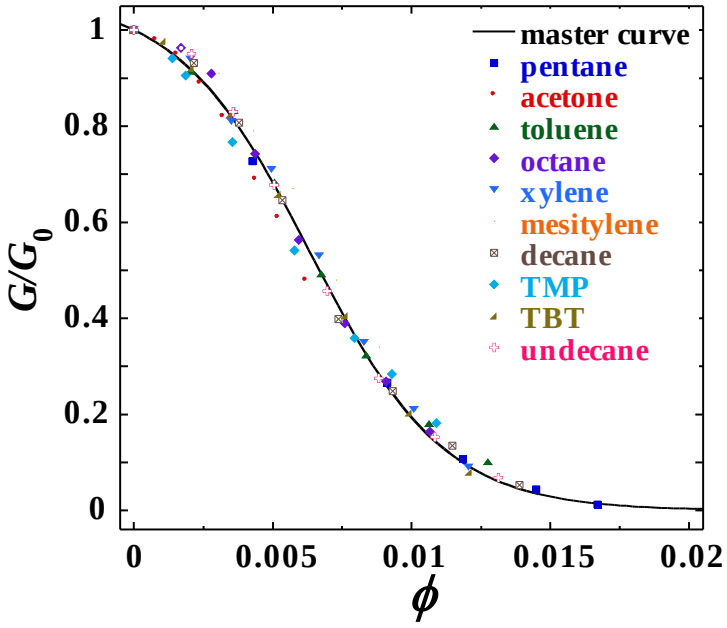

Figure 11-2. When the equilibrium response is plotted as a function of volume fraction of absorbed analyte, the result is master transduction curve that is dependent on the characteristics of the particular sensor.

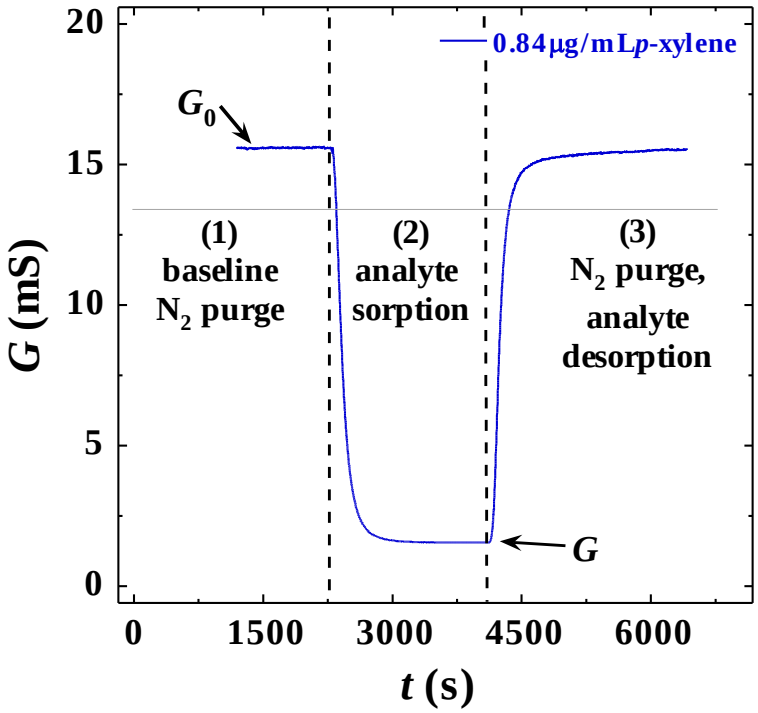

Figure 11-3. Response of an FSCR to a 2000 s exposure of 0.84 μg/mL *p*-xylene illustrates typical sensor response kinetics. The conductance drops quasi-exponentially, then recovers on the same timescale during the nitrogen purge.

11.3. EXPERIMENTAL

11.3.1. CHEMIRESISTOR FABRICATION

The chemiresistors used in this research consist of five identically fabricated FSCRs. The FSCR composite is typical and is composed of 15 vol.% 3–7 μm gold-plated nickel particles encapsulated in the Gelest OE-41 PDMS. In this case, the particles are mixed in the PDMS precursors and a volume of hexane equal to the volume of PDMS is then added to thin the viscous composite precursor. The sensors were cured at 40 °C for 24 h in a ~750 G uniaxial magnetic field yielding the chain-like particle network structure.

11.3.2. ANALYTES

The model analytes used in this research are acetone, toluene, p-xylene, mesitylene, and

undecane. All of the analytes are from either Fisher Chemicals (A.C.S. certified reagent grade) or Aldrich Chemicals (ReagentPlus grade). Pertinent physical data for the analytes (saturation vapor pressures and χ parameters) are included in Table 11-1. The aromatic compounds toluene, xylene, and mesitylene and undecane were chosen for use as analytes due to their similar χ parameters with PDMS and dissimilar vapor pressures.

analyte	***P**(25 °C) (Torr)**	χ
toluene	28.97	1.2682
p-xylene	8.80	1.2576
mesitylene	2.55	1.4236
acetone	228.19	2.2264
undecane	0.39	1.1257

Table 11-1. Room temperature saturation vapor pressures, and χ parameters for the analytes.[53]

11.3.3. SORPTION KINETICS

To study diffusion it is necessary to determine analyte mass-sorption as a function of time. This is accomplished by using the transduction curve in Eq. 11-1 to transform the FSCR response curves, such as that in Figure 11-3, into volume fraction of absorbed analyte. Solving Eq. 11-1 for ϕ(t) gives

$$\phi(t) = \frac{\phi_{1/2}}{\Gamma} \ln\left[1 + \left(e^{\Gamma} - 1\right)\frac{G_0 - G(t)}{G(t)}\right]. \qquad \textbf{(11-3)}$$

Using the equilibrium transduction curve to relate the non-equilibrium response to the non-equilibrium sorption is clearly an approximation, since it is an unproven assumption

that the sensor conductance depends only on the total mass sorption, and is insensitive to the swelling gradients that accompany diffusion. The utility of this approximation can only be judged by the quality of the final results shown below.

Figure 11-4 illustrates a time-dependent mass-sorption curve obtained from the sensor response. Diffusion into a finite slab is a mathematically complex problem, but for practical purposes the kinetic data can be fit by the simple exponential expression

$$\phi(t) = \phi_\infty(1 - e^{-t/\tau_{meas}}). \qquad \textbf{(11-4)}$$

Here t is time and τ_{meas} is the measured response time of the chemiresistor to the analyte in question. Fitting to this form will prove useful in correcting the observed kinetics data for the time it takes for the analyte concentration to reach steady state in the flowcell. Despite this we can actually obtain the response time in a model-independent fashion. To do so we simply plot the integral $A = \int_0^t \Delta\phi(s)/\phi_\infty ds$ against $B = \Delta\phi(t)/\phi_\infty$, where $\Delta\phi(t) \equiv \phi_\infty - \phi(t)$. We can operationally define τ_{meas} as the y-intercept of this curve in the limit as $\Delta\phi(t) \to 0$, but if Eq. 11-4 is a reasonable fit, the result will be a straight line whose y-intercept is easily obtained. The data in Figure 11-5 are indeed linear, so Eq. 11-4 is actually quite a good description of the raw kinetics data.

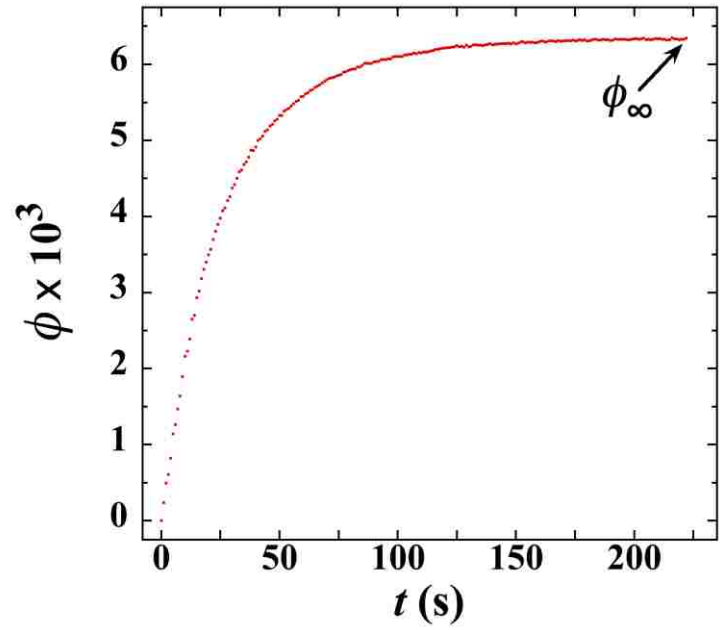

Figure 11-4. The volume fraction of absorbed analyte, ϕ, approaches its asymptotic value exponentially upon exposure to an analyte, in this case *p*-xylene vapors at an activity of 0.054.

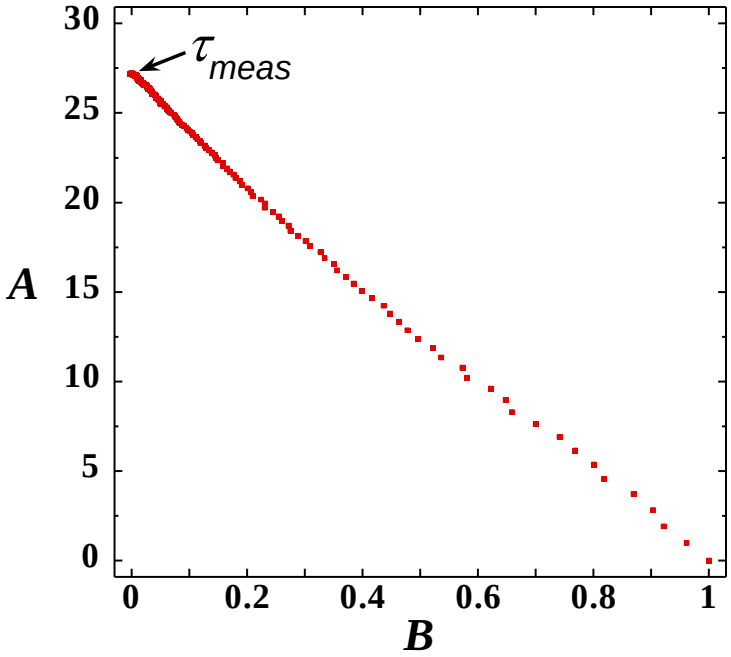

Figure 11-5. The measured characteristic response time, τ_{meas}, is the *y*-intercept of the line obtained by plotting $A = \int_0^t \Delta\phi(s)/\phi_\infty ds$ as a function of $B = \Delta\phi(t) = \phi_\infty - \phi(t)$.

11.4. RESULTS

In the following we give the theoretical expression for the true sorption kinetics, which is shown to be independent of analyte activity. We then develop an expression for the measured sorption kinetics, which is a convolution of the true sorption kinetics and the kinetics of filling the flowcell. We then show how the flowcell fill kinetics can be determined from the measured sorption kinetics, and how the fill time can be used to extract the true sorption time from the measured time. Both the measured and true sorption kinetics are shown to be independent of activity, but strongly dependent on the analyte saturation vapor pressure.

11.4.1. PREDICTED SORPTION TIME

From Raoult's Law the partial pressure of a chemical species, p, in a gas is equal to its volume fraction, ϕ_{vap}, times the total pressure, or $\phi_{vap} \equiv V / V_{tot} = p / p_{tot}$. Recall that the analyte activity is $a = p / p^*$, therefore $a = \phi_{vap} / \phi^*_{vap}$, where ϕ^*_{vap} is the volume fraction of analyte vapor at saturation. From the linearized form of Flory-Huggins equation (Eq. 11-2), $\phi = a / e^{1+\chi}$, the partition coefficient, K, is then

$$K \equiv \frac{\phi}{\phi_{vap}} = \frac{1}{\phi^*_{vap} e^{1+\chi}}. \qquad \textbf{(11-5)}$$

At high inlet stream fluxes the response time of an FSCR is diffusion limited, and the sensor's response time can be expressed as [62]

$$\tau_d \propto K\frac{d^2}{D_t} = \frac{1}{D_t \phi^*_{vap} e^{1+\chi}} d^2, \qquad \textbf{(11-6a)}$$

where d is the thickness of the composite and D_t is the diffusion coefficient of the analyte into the silicone. Note that even for analytes of identical chemical affinity there is discrimination based on sorption kinetics, due to variations in their diffusivity and saturation volume fraction. The saturation vapor pressure is given by $P^* = \rho\phi^*_{vap}RT/M_w$, so the sorption time can also be written as

$$\tau_d \propto \frac{RT}{P^*} \times \frac{\rho}{M_w D_t e^{1+\chi}} d^2. \qquad \textbf{(11-6b)}$$

The saturation vapor pressure varies over a wide range, so the sorption kinetics can be a very useful method of discrimination.

11.4.2. MEASURED SORPTION TIME

The goal is to determine the true sorption time, including any dependence this time might have on analyte activity. Unfortunately, the measured sorption time is a convolution of two factors: the time it takes for the analyte activity in the flowcell to reach its steady-state value (flowcell fill time), and the true mass-sorption time. In a constant flow rate apparatus, and for any particular analyte, neither of these factors should be dependent on analyte activity, so the measured sorption time should be independent of analyte activity. The data in Figure 11-6 show that this is indeed the case, and also show significant differences in the sorption kinetics for different analytes, as expected.

The data in Figure 11-6 are an average for five sensors, each tested simultaneously in the same flowcell. Because of sensor-to-sensor variations in polymer thickness, each chemiresistor had a somewhat different response time. To account for these thickness variations we normalized the response time of each sensor to agree with that of an arbitrarily chosen reference sensor, by exposing the sensors to a mesitylene activity of 0.058, which resulted in a swelling of 0.005. These renormalized timescales were then used to determine both the average response time to an analyte and the associated measurement error in terms of standard deviation. The dimensionless correction factors ranged from 0.6 to 1.3.

An accurate determination of the sorption kinetics ideally requires that the flowcell fill time is fast compared to the sorption kinetics. In the following we will determine this fill time from the measured sorption kinetics and use this value to extract the true sorption kinetics from the measured values. The true sorption time can then be compared to the flowcell fill time to determine whether this fast fill time condition is met in our experiments.

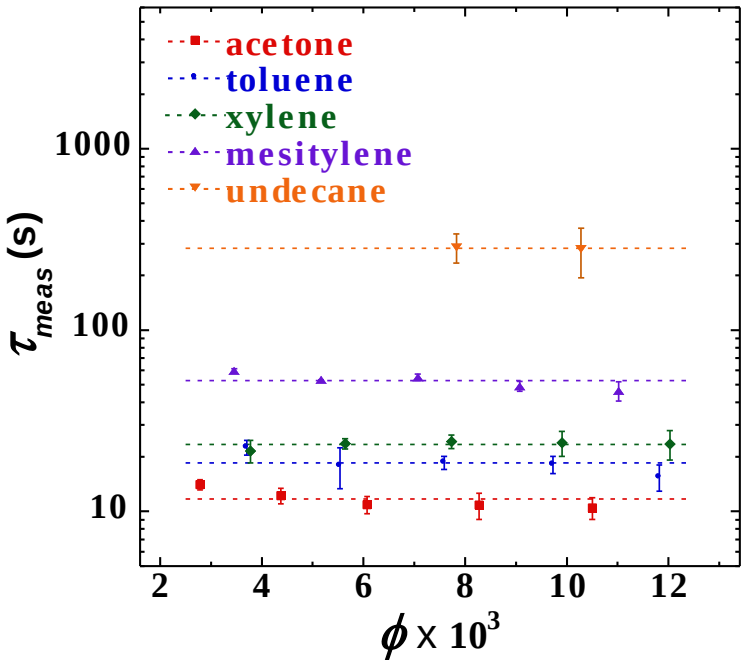

Figure 11-6. The average measured response time is independent of the volume fraction of absorbed analyte, ϕ, and thus the analyte activity, but is strongly analyte dependent, easily discriminating between those having nearly identical chemical affinities.

11.4.3. FLOWCELL FILL TIME

After the inlet stream starts to deliver an analyte of fixed activity to the flowcell, the analyte activity rises continuously, due to the finite volume of pure nitrogen that must be displaced. The transient analyte activity can be obtained by modeling the flowcell as a continuously stirred tank, and is of the form:

$$a(t) = a_{\infty}(1 - e^{-t/\tau_f}). \qquad \textbf{(11-7a)}$$

In terms of the volume fraction of the vapor this is

$$\phi_{vap}(t) = \phi_{vap}(\infty)(1 - e^{-t/\tau_f}). \qquad \textbf{(11-7b)}$$

The characteristic time for the flowcell to reach a steady-state concentration is given by $\tau_f = V_f / F$, where V_f is the volume of the flowcell and F is the volumetric flow rate of nitrogen from the inlet stream.

11.4.4. CONVOLUTION OF TIME SCALES

The measured composite swelling in Figure 11-4 is a convolution of the increase in the analyte vapor activity in the flowcell and the diffusive kinetics, which for simplicity we take to be of the form $\phi(t) = \phi_\infty(1 - e^{-t/\tau_d})$ for a step increase in the analyte activity at $t = 0$. Using Eq. 11-5, the expression is

$$\phi(t) = K \int_0^t \left. \frac{d\phi_{vap}(t)}{dt} \right|_{t=s} \times \left[1 - e^{-(t-s)/\tau_d}\right] ds. \qquad \textbf{(11-8)}$$

Using Eq. 11-6a to evaluate the derivative gives

$$\phi(t) = \frac{K\phi_{vap}(\infty)}{\tau_f} \int_0^t e^{-s/\tau_f} \left[1 - e^{-(t-s)/\tau_d}\right] ds. \qquad \textbf{(11-9)}$$

A straightforward integration leads to the final expression for the sorption kinetics,

$$\phi(t) = A\phi_{vap}(\infty)\left[1 - \frac{\tau_d}{\tau_d - \tau_f} e^{-t/\tau_d} + \frac{\tau_f}{\tau_d - \tau_f} e^{-t/\tau_f}\right]. \qquad \textbf{(11-10)}$$

The measured timescale can then be computed from this equation, and the surprisingly simple result is

$$\tau_{meas} = \frac{1}{\phi_\infty} \int_0^\infty [1 - \phi(t)] dt = \tau_d + \tau_f . \qquad \textbf{(11-11)}$$

The true diffusion time can thus be obtained from the measured time by $\tau_d = \tau_{meas} - \tau_f$. (The case where $\tau_d = \tau_f$ leads to division by zero in Eq. 11-10. This division looks troublesome, but can be handled by defining $\tau_d = \tau_f (1+\varepsilon)$ and carefully taking the limit as $\varepsilon \to 0$.)

11.4.5. CORRECTED SORPTION TIMES

The correction of the measured sorption times for the flowcell fill time requires a determination of the fill time. The fill time can be extracted from the measured sorption times themselves, through a limiting process, as we will now describe. To obtain accurate measured sorption times we first average these measured times over all analyte activities, to obtain a mean response time we call $\bar{\tau}_{meas}$. This averaging is valid, because the measured sorption time is independent of analyte activity as demonstrated in Figure 11-6. A plot of this average time versus the inverse analyte saturation vapor pressure results in a straight line with a non-zero *y*-intercept, as seen in Figure 11-7. Of course, at infinite saturation vapor pressure the sorption time τ_d must be zero since the diffusive flux is infinite. Therefore, this finite intercept of 13.8 s corresponds to the fill time of the

flowcell and can be used to produce the corrected sorption times, τ_d, in Figure 11-7. This measured flowcell fill time is in good agreement with the theoretical prediction, using V_f / F.

Figure 11-7 shows a nearly perfect proportionality between the sorption time, τ_d, and the analyte saturation vapor pressure, p^*. Eq. 11-6b shows that other analyte parameters, such as the diffusivity, also determine this sorption time, but apparently these combined factors are more-or-less constant for the analytes we tested. Also, the saturation vapor pressure varies strongly from analyte to analyte. The homologous series of aromatic analytes, all of which have nearly identical Flory parameters, and thus identical equilibrium chemiresistor response as a function of activity, are now easily distinguished. For toluene, *p*-xylene, and mesitylene the sorption times are 3.7, 10.0, and 37.0 s, respectively, which is in good agreement with their relative reciprocal saturation vapor pressures, 3.45, 11.4, 39.2 ($\times 10^{-2}$ Torr^{-1}). These sorption time differences are large compared to the errors associated with our measurements, even though the sorption time of toluene is much faster than the fill time of 13.8 s. To measure faster sorption times is possible, but would require either higher flow rates and a smaller flowcell volume, so that the fill time is faster, or thicker sensors, to increase the sorption time.

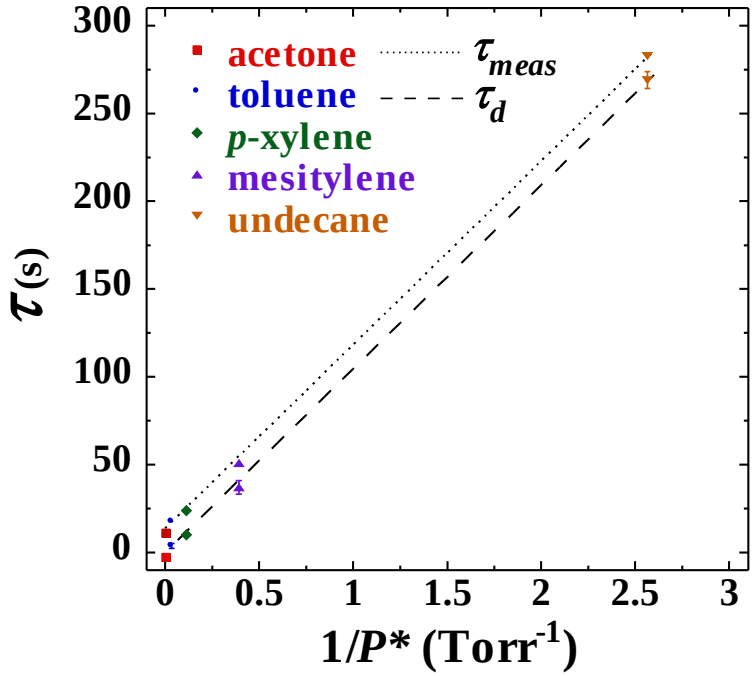

Figure 11-7. The measured sorption time, τ_{meas}, is proportional to the inverse saturation vapor pressure. The non-zero *y*-intercept of 13.8 s is the flowcell fill time, which when subtracted from the measured sorption time gives the true sorption time, τ_d. The sorption time of undecane is nearly two orders of magnitude larger than that of toluene despite their equilibrium response curves being nearly identical as in Figure 11-1.

11.5. Conclusion

We have used a field-structured chemiresistor to demonstrate that response kinetics can be used to discriminate between analytes, even between those that have identical chemical affinities for the polymer phase of the sensor. To do this, we have used the analyte-independent transduction curve (conductance versus polymer swelling) to transform the time-dependent sensor conductance into a time-dependent polymer swelling. From these swelling data we can determine the measured sorption time, which is a combination of the true sorption kinetics and the fill time of the flowcell. The true sorption kinetics is obtained by correcting for the fill time, and we find that the sorption kinetics is independent of the analyte activity, but inversely proportional to the saturation

vapor pressure of the analyte. Saturation vapor pressures vary greatly from analyte to analyte, making response kinetics a powerful method of analyte discrimination, even with a single sensor. Finally, we suggest that when the sensing environment presents fluctuations in the analyte activity, an analysis of the fluctuations in the sensor response fluctuations can be used to extract the sorption kinetics. This approach would obviate the need for an engineered flow system that can deliver an analyte pulse, and will be the focus of our future work.

12. FSCR RESPONSE AS A FUNCTION OF PARTICLE SHAPE

***Abstract*—** In this chapter we examine the effect of particle shape on FSCR response. Unlike agglomerated spheroid particles, it is found that Au-coated Ni platelets fail to form anisotropic chain-like structures when subjected to uniaxial magnetic fields. Sensors made with these platelet particles exhibit decreased sensitivity when compared to those made with the typical spheroid particles. This observed decrease in sensitivity is attributed to the lack of a low-dimensionality structure and the failure of the particles to form a network that is *just* at the conductivity critical point. In addition, FSCRs made with Ag-coated particles, which are more spherical and smoother, show an increase in sensitivity. This might be attributed to the lower conductivity of the Ag coating, which is found to increase the composite's initial resistance. However, FSCRs made with varying Au-shell thickness show an expected increase in the initial resistance, but with no effect on sensor response. The observed increase in sensitivity with the Ag-particle sensors is therefore attributed to the morphology of the particles and not the increased contact resistance. Lastly, sensors made with Au-coated particles that are smooth and spherical show a dramatic increase in sensitivity over the agglomerated Au-coated particles with high surface roughness—further reinforcing the hypothesis that particle morphology, not particle-shell resistivity, is a major factor in determining sensor sensitivity.

12.1. Introduction

In the background chapter the unusual and extreme response of these sensors was attributed to the low-dimensionality structure of the particle phase, which leads to a particle network at the conductivity critical point. Particle morphology is the key factor for the magnetic properties such as the demagnetizing factor and particle dipole-dipole interactions for a given magnetic material. In this chapter we discuss how particle shape can affect both the network structure and the inter-particle contact, and how these in turn affect sensor response.

12.2. Experimental

The FSCRs studied in this experiment differ only in their particle phase and are fabricated identically in all other regards (described in the experimental chapter). The morphologies of the particles are determined by the SEM images shown in Figure 12-1 below. The control sensors contain the typical Au-coated, agglomerated spheroid Ni particles obtained from Goodfellow. The platelet sensors employ 20 μm, ~.3 μm thick nickel flakes coated with MgF_2, which are additionally gold-coated in-house with the Enthone plating solutions (Appendix E.1.). The Ag-Ni particles obtained from Novamet (standard grade) are 30–40 μm in diameter and display mild agglomeration with a comparatively smooth surface. The platelet FSCRs and their respective control sensors were cured at 65ºC whereas the Ag-Ni sensors and their respective control sensors were cured at 50ºC. All sensors were cured in a 650 gauss uniaxial magnetic field.

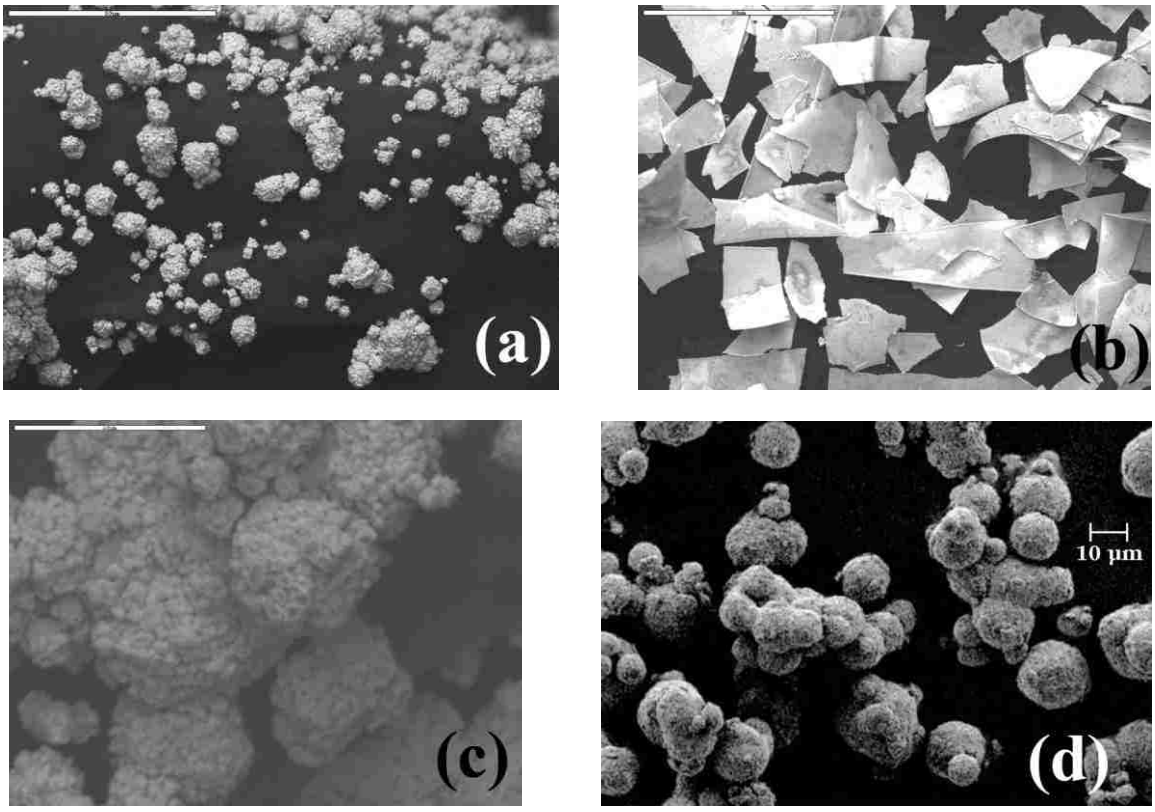

Figure 12-1. SEM micrographs illustrate the various particle morphologies. **(a)** The 3–7 µm Ni spheroid particles are agglomerated and have a popcorn-like morphology. **(b)** The 20 × 3 µm Ni platelets will have radically different magnetic properties . **(c)** Higher magnification of the 3–7 µm Ni shows high surface roughness. **(d)** The 30–40 µm Ag-coated Ni particles appear smoother and are more spherical (image reprinted from Novamet, www.incosp.com). The scale bars are 50 µm for (a) and (b), and 5 and 10 µm for (c) and (d) respectively.

12.3. Results and Discussion

The micrographs in Figure 12-2 show the composite network structures resulting from the uniaxial magnetic field for the Goodfellow spheroid and platelet FSCRs. The spheroid particles form chains where there is no discernable structure from the platelets. The chain-like structure is caused by complex yet well-understood attractive dipole-

dipole interactions of spherical particles in uniaxial field.[37,63] The magnetic interactions between the platelet particles are extremely complex and are not yet understood. However, it is known that a single platelet will align along its long axis parallel to the applied field in order to minimize its demagnetizing factor, which is a measure of the magnetostatic energy. For example the demagnetizing factor for an infinite sheet of magnetic material will be unity when perpendicular to the field and zero when parallel to the field. The values for a semi-infinite rod in these configurations are one-half and zero, respectively, and a sphere will always have a value of one-third due to its symmetry. Though a platelet will align in the field, there is no cost in energy to rotate about its long axis. There is not sufficient resolution in Figure 12-2b to determine the structure of the platelet particle network, but sufficed to say, there is no apparent anisotropy in the orientation of the network.

Figure 12-3 below shows the response for the platelet and spheroid FSCRs to *p*-xylene. The spheroid-particle FSCR has a response midpoint of 7.7 μg/mL compared to 19.2 μg/mL for that of the platelet FSCR—this is a 2.5-fold decrease in sensitivity by this measure. It is evident that the shape of the particles has a large impact on the network structure and therefore the sensitivity of the sensors. A possible explanation is that the platelets appear to lack the attractive dipole-dipole interactions, which bring the network to the critical percolation threshold.

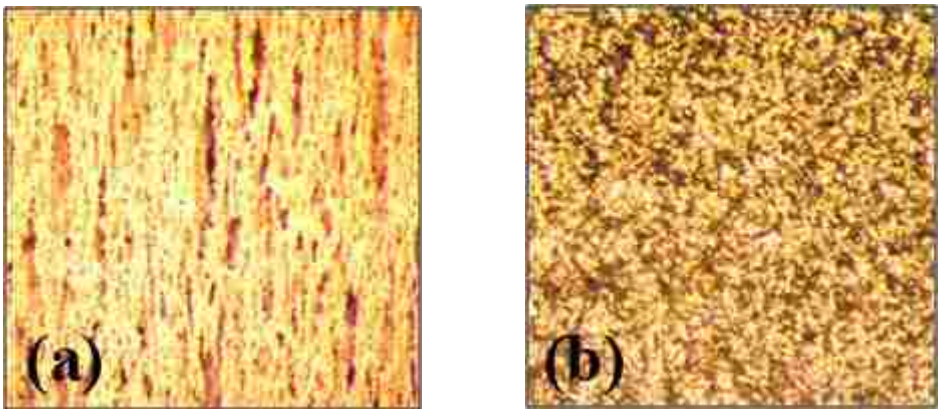

Figure 12-2. Micrographs at 60× magnification of the FSCR composites containing Au-plated Ni particles structured in a uniaxial magnetic field. **(a)** The spheroid particles are aligned into an anisotropic chain-like structure. **(b)** There is no apparent structure for platelet particle network.

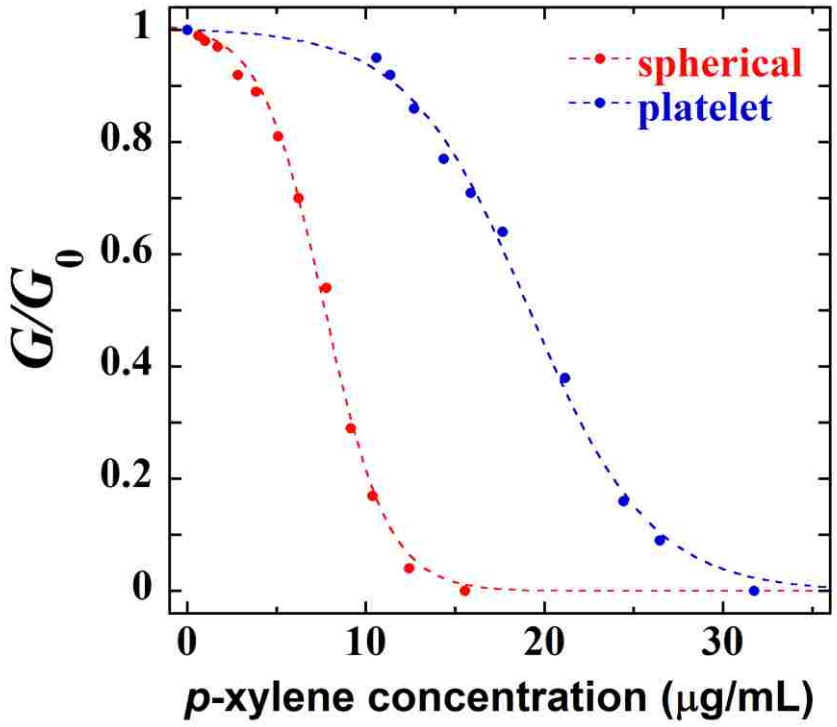

Figure 12-3. The spheroid-particle FSCR has a response midpoint of 7.7 μg/mL compared to 19.2 μg/mL for the platelet FSCR. This 2.5-fold decrease in sensitivity (by this measure) illustrates the impact of particle shape on the network structure and therefore on sensor response.

We are now interested in determining if sensitivity is affected by a decrease in the roughness and the degree of agglomeration as found with the Novamet Ag-Ni particles. Figure 12-4 below shows the response curves for two FSCRs containing Ag-coated spheres and those for two FSCRs containing Goodfellow Au-coated spheroid particles. Here, the Ag-Ni sensors are much more sensitive than the Au-Ni sensors with response midpoints of 5.5 μg/mL and 11.6 μg/mL respectively. This increase in sensitivity with the Ag-Ni particles could be attributed to the change in conductive shell material. Although Ag has a lower resistivity than Au, Ag readily forms an oxide which dramatically increases the resistivity. The initial resistances for the Ag and Au FSCRs are 18 and 2 Ω respectively.

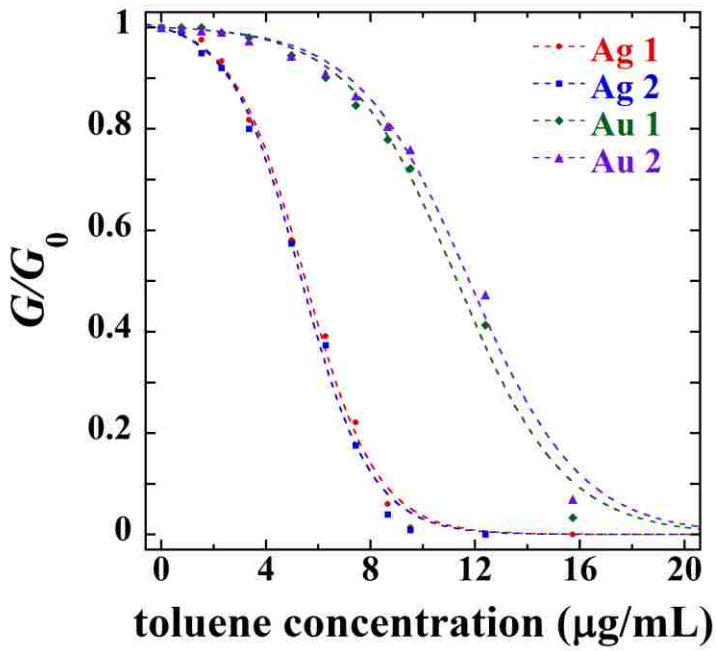

Figure 12-4. Response curves for four FSCRs show that sensors made with Ag-coated Ni have higher sensitivity than those made with the typical Goodfellow Au-coated Ni. There are two possible explanations for this sensitivity increase: (1) the disparate particle morphologies (as seen in Figure 12-1), or (2) the difference in resistivity between the Au and Ag shells.

To examine the effect of the resistivity of the particle shell on sensor response, FSCRs were made with Goodfellow Ni particles varying in their Au-shell thickness, which is accomplished by limiting the immersion-plating reaction time between 3 and 15 min. The change in Au coverage can be seen as a change in the color of the bulk powder from a cinnamon-brown to a grayish-brown for reduced reaction times. Figure 12-5a below shows a decrease in the initial resistance, R_0, of three FSCRs as the reaction time increases. In fact, sensors made with the uncoated Ni are completely non-conductive. The response of these sensors to xylene was determined with the results in Figure 12-5b, which illustrates that the increased resistivity of the particles has no apparent impact on FSCR response under conditions of constant particle morphology. If the resistivity of the particle shell does not affect sensor response, then what *is* the cause for the dramatic decrease in sensitivity observed from the Ag-Ni based sensors?

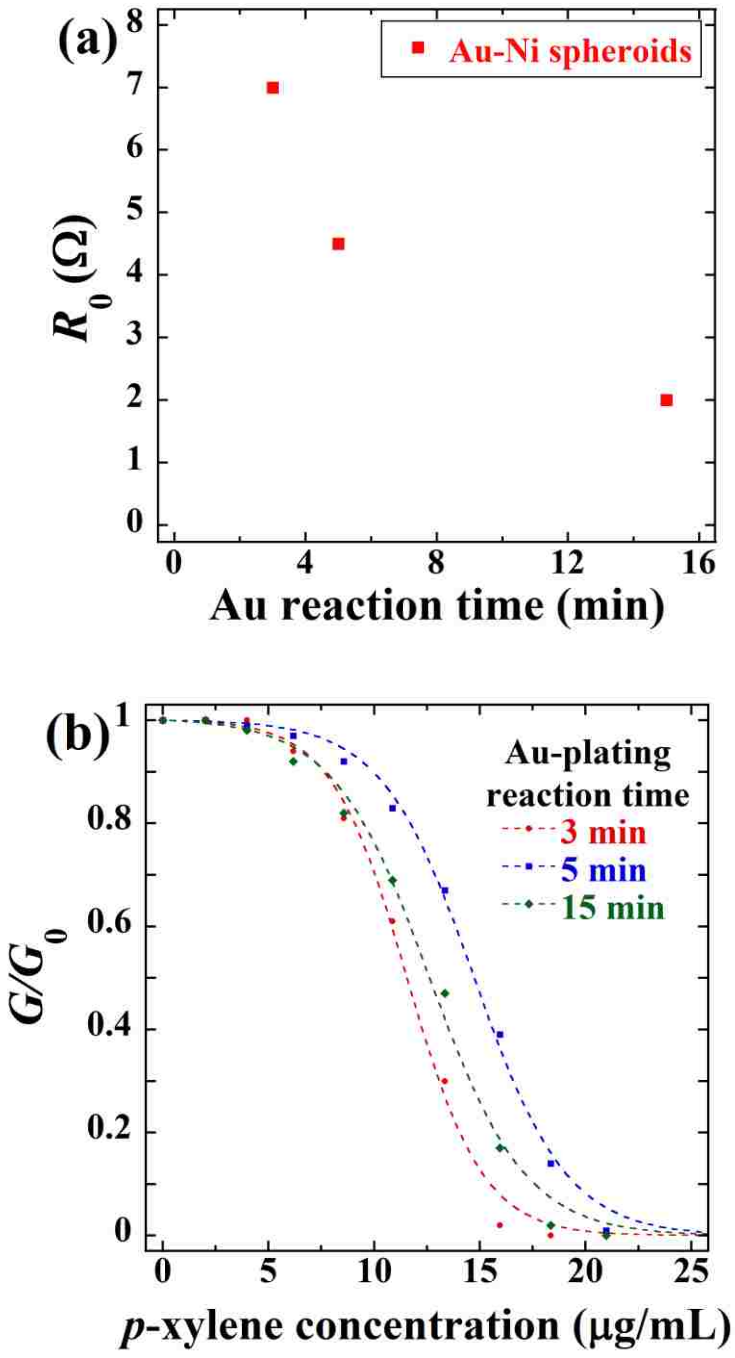

Figure 12-5. **(a)** FSCRs made with the Goodfellow Ni particles show a decrease in initial resistance, R_0, with increasing Au-plating reaction time (Au-shell thickness). **(b)** The response of these sensors to xylene, however, shows no dependence on the Au-shell thickness.

A smoother, rounder particle will have fewer contact points with its neighbors as the cartoon in Figure 12-6 illustrates—in fact, two hard, perfect spheres can only share one infinitesimally small contact point. It is therefore reasonable that a decrease in the contact area could have a direct impact on the composite's conductance with applied strain. Kchit and Bossis have developed a piezoresistivity model for FSCs that takes into account the surface roughness of the particles, which corroborates this hypothesis.[48]

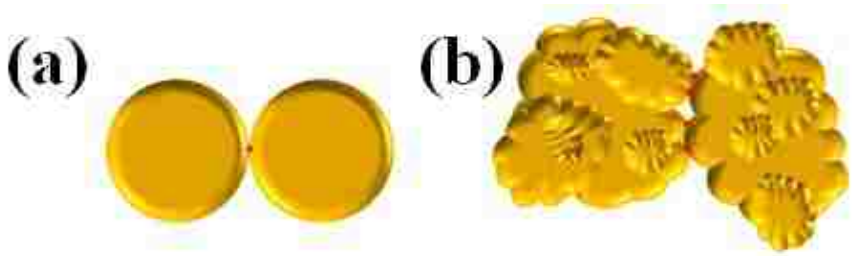

Figure 12-6. (a) Perfectly spherical, hard particles have a single infinitesimally small point of contact, whereas **(b)** rough agglomerated spheroids can have multiple contact points and even overlapping sections that could remain in contact with small strains. This difference in morphology could certainly affect the dependency of charge transport on strain.

To further probe effect of particle morphology, we would like to directly compare the response of sensors made with the Au-Ni Goodfellow particles to those made with smooth, monodisperse Au-Ni spheres. To accomplish this we employed the particles shown in Figure 12-7, which are offered by Selzer Metco as E-Fill 2755. Because of their equivalent shell material, they should reinforce the hypothesis that particle morphology and surface roughness are major factors in determining FSCR sensitivity.

The response curves for two sensors made with the morphologically disparate particles are shown in Figure 12-8 below. These response data show a dramatic increase in sensitivity for the sensor made with the E-Fill Au-Ni particles over that for the sensor

made with typical Goodfellow spherical agglomerate Au-Ni particles. The toluene-activity response midpoints for the two sensors are 0.08 and 0.16, which is a sensitivity increase of 2-fold by this measure. This sensitivity increase is attributed to the highly spherical morphology and smooth surface of the E-Fill particles, which is thought to decrease the number of particle-contact points. Although we have not recorded these images, micrographs show that the E-Fill particles produce finer (less clumped) chain-like structures when compared to the structures formed with the Goodfellow particles—despite the particles' similar sizes.

Figure 12-7. A SEM micrograph of 10 μm Au-coated Ni particles (offered by Sulzer Metco as E-Fill 2755) shows that these particles are smooth, relatively monodisperse spheres. This figure is digitally colored and reproduced from Sulzer Metco (www.conductivefillers.com).

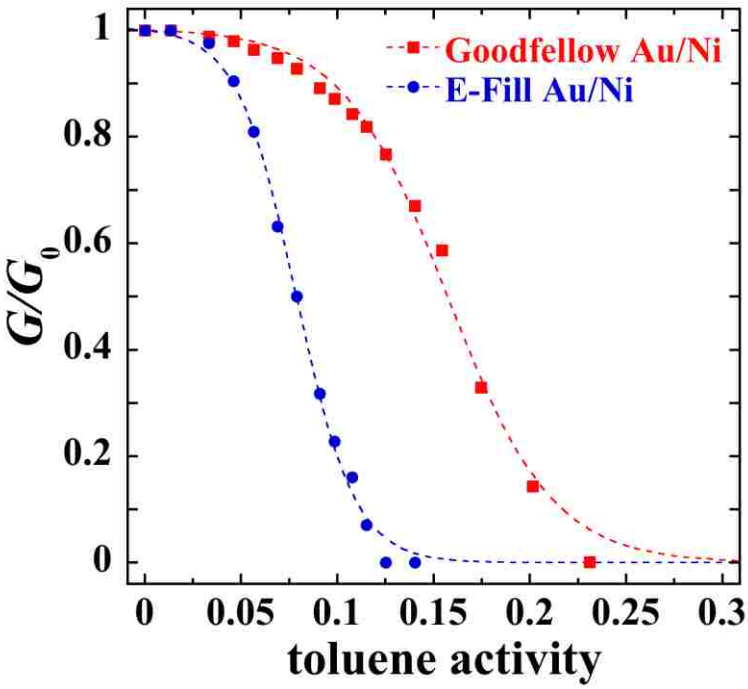

Figure 12-8. The response curve for a sensor made with E-Fill Au-Ni particles shows a dramatic increase in sensitivity over that for a sensor made with typical Goodfellow spherical agglomerate Au-Ni particles. The toluene-activity response midpoints for the two sensors are 0.08 and 0.16, which is a sensitivity increase of 2-fold by this measure. This sensitivity increase is attributed to the highly spherical morphology and smooth surface of the E-Fill particles, which is thought to decrease the number of particle-contact points. Both sensors were made with 15 vol.% particles and cured at 50°C.

12.4. Conclusion

We have previously developed techniques to tailor the sensitivity and range of FSCRs by controlling polymer cure stresses. In this chapter we showed that particle morphology also plays an important role in sensor response and allows for yet another means of controlling FSCR sensitivity. FSCRs made with Goodfellow Au-Ni spheroids have a ~2.5-fold increase in sensitivity over those made with platelet-shaped particles. This result reinforces the premise that FSCRs' low-dimensionality, structured chain-like particle networks have superior response compared to those whose particle networks are not brought to the critical percolation threshold. In addition, FSCRs containing Ag-Ni spheres that are relatively smooth and uniform show an additional ~2-fold increase in sensitivity compared to those containing the popcorn-like, agglomerated Au-Ni spheroids. This could be attributed to the higher resistivity of the particle-shell material, but experiments show that this does not lead to the pronounced increase in sensitivity we observe for the Ag-Ni sensors. Instead it is hypothesized that this sensitivity increase is due to the particle morphology and roughness. This is reasonable because fewer inter-particle contact points should bring the composite even closer to the critical point of conductivity. This hypothesis was substantiated with sensors made with more spherical, smoother, but similarly Au-coated particles, which show a dramatic increase in sensitivity over those made with spherical-agglomerate particles.

13. METHODS FOR MITIGATING FALSE-POSITIVE RESPONSE DUE TO TEMPERATURE

***Abstract*—**FSCRs respond to temperature by the same mechanism by which they respond to chemical vapors, polymer swelling. Obviously this themoresistivity property is an undesirable trait because a response due to a temperature change cannot be differentiated from that due to a chemical by the conductance data alone. In this chapter, we discuss methods for minimizing these temperature-induced baseline fluctuations. One such method is the use of the balanced Wheatstone bridge, which is a simple circuit constructed such that there is an output voltage if the relative resistances of two chemiresistors changes. This relative resistance will not change due to temperature fluctuations, but *will* change in response to an analyte. The data we present show a 23-fold decrease in baseline drift corresponding to a 7 °C temperature change.

13.1. Thermoresistance Properties of FSCRs

Field-structured chemiresistors (FSCRs) respond to changes in temperature by the same mechanism by which they respond to changes in analyte concentration—polymer swelling. In the case of temperature response, composite swelling is caused by the mismatch between the coefficient of thermal expansion (CTE) of the elastomer and that of the particle phase as described in Chapters 6 and 8. Figure 13-1 below shows the response of an FSCR to temperature. Thermoresistance is obviously an undesirable property of chemiresistors, due to the inability to differentiate between conductance changes caused by temperature fluctuations and those caused by an analyte. This chapter

details methods to minimize baseline drift and therefore maximize the practical resolution of FSCRs.

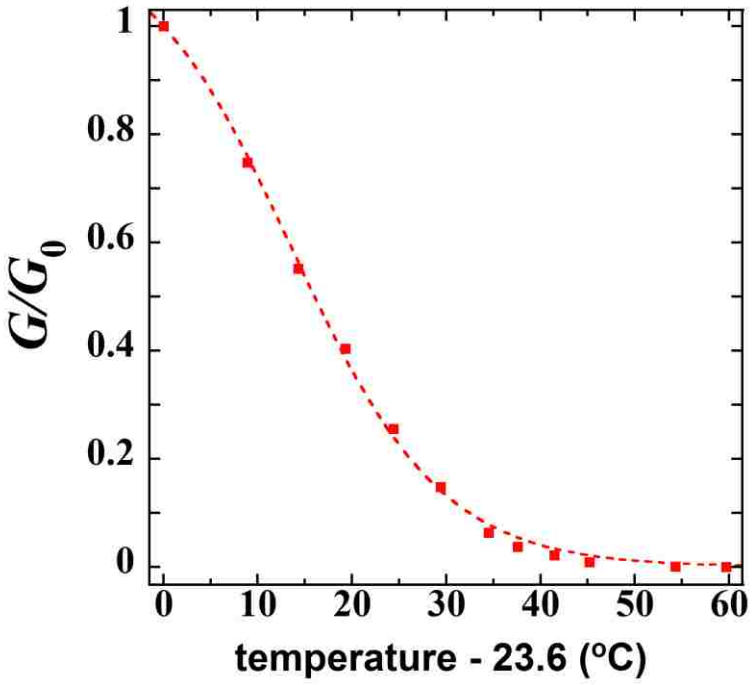

Figure 13-1. Response of an FSCR to temperature is caused by thermal expansion of the polymer phase. The response curve is similar to that for an analyte.

13.2. Methodology

Despite the temperature dependence of FSCR conductance, there are methods for eliminating false positive readings due to temperature fluctuations. The first method relies on simultaneously monitoring sensor conductance and temperature. In this case sensor response is correlated to thermocouple (TC) measurement and the baseline is corrected for any change in temperature. Coating the TC with a similarly thick polymer film will match the temperature response time of the TC to that of the sensor. Second, the temperature of the sensor can be controlled above ambient with a heated substrate. Both of these methods further complicate the necessary transduction process and are

antithetical to the simple chemiresistor concept—a reoccurring theme. The final method, which we describe in this chapter, involves normalizing the sensor's baseline conductance to that of a sensor with a similar response curve. This normalizing, or *dummy*, sensor is subjected to the same temperature fluctuations, but is isolated from possible analyte exposure. In this way, any baseline fluctuations that are not caused by an analyte can be corrected.

To demonstrate this method, six FSCRs were fabricated and their responses to toluene were simultaneously measured. Although all of the sensors responded similarly (within 5 %), two sensors were selected that have nearly identical response as shown in Figure 13-2 below. Additionally, the sensors were selected based on their similar response kinetics, which is determined by the composite thickness.

Figure 13-3 shows the conductance baselines of the two sensors over the course of 100 h. These baselines drift as much as 17% between 20–27°C. It is unimportant that the sensors' conductances are dissimilar only that their steady-state and response kinetics are identical. To correlate the time-dependent sensor baselines the baseline of *sensor A* is then plotted against that of sensor B, which results in a line that is fit with $G_{0,A}(t) = r^{-1} \cdot G_{0,B}(t)$ (Figure 13-4). $1/r$ is the calibration constant that we will use to create a predicted baseline for *sensor A*, $G_{0,\mathrm{A},calc}$, from *sensor B*'s actual baseline. Figure 13-5 shows agreement between this predicted baseline for *sensor A* and the actual baseline.

Since we know that changes in the calculated baseline are caused by temperature fluctuations, we can use this information to correct the actual baseline for *sensor A* and then normalize this corrected baseline to an arbitrary baseline, $G_{0,norm}$, using

$$G_{0,A,corrected} = \frac{G_{0,A,actual}}{G_{0,A,calc}} \cdot G_{0,norm} = \frac{r \cdot G_{0,A,actual}}{G_{0,B}} \cdot G_{0,norm} \quad \textbf{(13-1)}$$

In this case, we chose $G_{0,norm}$ to be the conductance value at room temperature and zero time, which is ~0.11 S. This corrected baseline is compared to the actual baseline in Figure 13-6, which shows that the maximum temperature-induced baseline drift is reduced from ~17% to ~0.7%—a 23-fold decrease in drift. It should be noted that this particular example was carried out using two existing FSCRs and no special effort was made to produce two identical sensors. Tighter control over the fabrication variables can be easily implemented leading to further improvements of baseline drift.

We know from Chapter 6 that an increase in temperature will also change the sensitivity of the transduction curve, so if large temperature changes are expected this must be taken into consideration. However, this is not troublesome because the effect of temperature change on sensitivity is well understood.

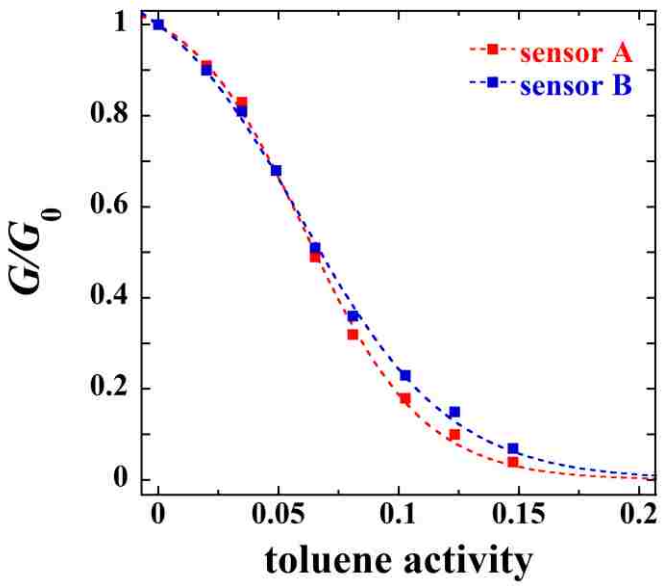

Figure 13-2. Two sensors were selected from a total of six to have similar steady-state and response kinetics. It is especially important that the sensors have similar sensitivities at low analyte concentration; this is the regime where temperature fluctuations will have an effect.

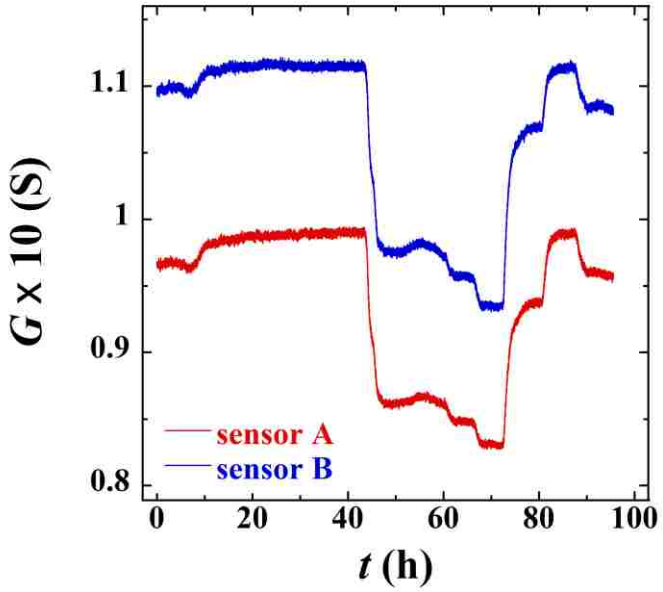

Figure 13-3. The time-dependent responses of two sensors to ambient temperature fluctuations (~20–27°C) over ~100 hours shows as much as a 17% response. The two sensors differ in their baseline conductance, but this is unimportant for the implementation of this method.

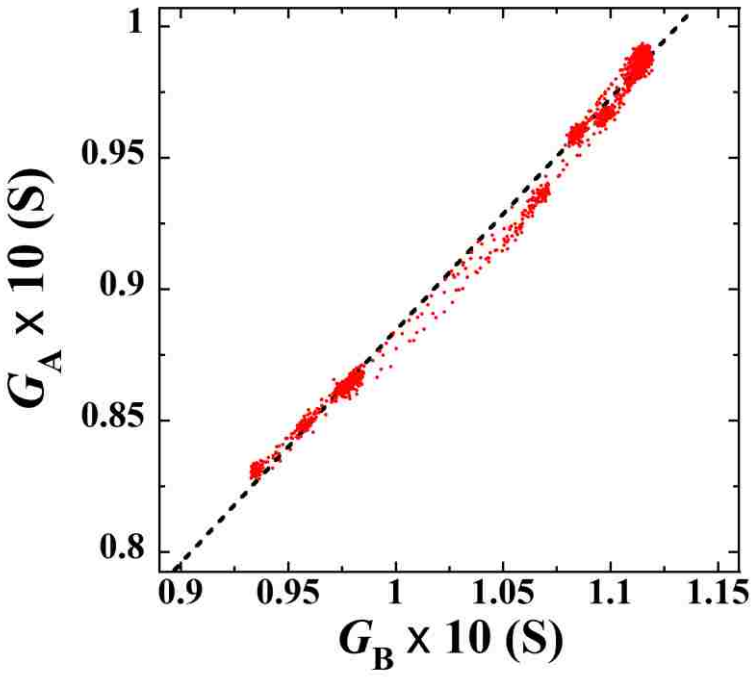

Figure 13-4. A plot the conductance data in Figure 13-3 for *sensor A* as a function of those for *sensor B* shows that the senors' baselines are well correlated. Fitting these data to a line with zero intercept yields $G_{0,A} = 0.884 \cdot G_{0,B}$. It should be noted that another function could give a slightly better fit in this case. The closer in sensitivity and response kinetics these sensors are, the more closely these data will fit a line.

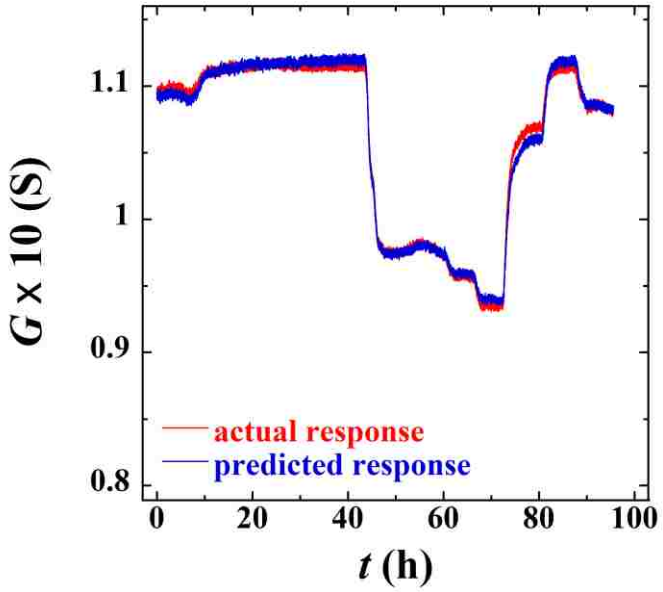

Figure 13-5. *Sensor A*'s baseline fluctuations due to temperature are predicted solely from those of *sensor B*. The comparison of the predicted kinetic temperature response of *sensor A* to the actual response shows good agreement.

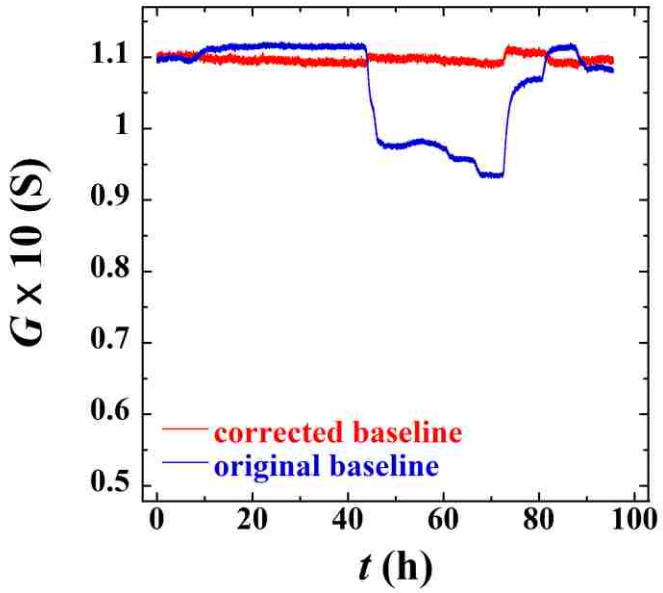

Figure 13-6. Comparison of the temperature-corrected baseline from Eq. 13-1 and the actual (non-corrected) baseline illustrates the utility of this method. The corrected baseline never deviates more than a signal-to-noise ratio of ~2 where the original baseline deviates more than 10-times this amount.

13.3. The Balanced Wheatstone Bridge Approach

Although the method described above is more than adequate for mitigating baseline fluctuations, it is none-the-less practically complicated to impliment in a simple field unit. We will now discribe a method that relies on the same priciples, but instead of requiring signal analysis and adjustment, the baseline is corrected by a simple circuit known as the Wheatstone bridge.

The Wheatstone bridge (shematically shown as in Figure 13-7) is a circuit that is used to measure an unknown electrical resistance by balancing two legs of a bridge circuit.[64,65] When these legs become unbalaced the measured output voltage becomes non-zero. The Wheatstone bridge is widely used for strain guages, which like chemiresistors, are inherently sensitive to thermal fluctuations (a chemiresistor is after all a specialized strain guage). In Figure 13-7 the chemiresistors are denoted by R_d and R_{cr}, where R_{cr} is the chemiresistor used to detect the analyte and R_d is the *dummy sensor* (the analyte-isolated sensor), which measures the temperature fluctuations *only*. R_1 and R_2 are fixed precision resistors. The circuit is designed such that $R_1 / R_2 = R_d / R_{cr} \equiv r$, where r is known as the *circuit efficiency*. It should be noted that although the fixed resistors are carefully chosen so that their resistance ratio is matched to that of the chemiresistors, it is unlikely that the bridge will output exactly zero volts when no analyte is present. To null this offset one of these fixed resistors is typically a potentiometer, which enables the bridge output to be physically adjusted to zero at room temperature.

The equation describing the change in the measured output voltage, V_{out} is [64]

$$\Delta V_{out} = V_{in} \cdot \frac{r}{(1+r)^2}\left(\frac{\Delta R_d}{R_{d,0}} - \frac{\Delta R_{cr}}{R_{cr,0}}\right)(1+\eta), \qquad \textbf{(13-2a)}$$

where η is approximatly zero when resistance changes are small (< 5%) and otherwise given by

$$\eta^{-1} = 1 + (1+r)\left(\frac{\Delta R_d}{R_{d,0}} + r \cdot \frac{\Delta R_{cr}}{R_{cr,0}}\right)^{-1} \qquad \textbf{(13-2b)}$$

From Eq.13-2, if the relative resistance changes of the two similar chemiresistors are equal (as would be expected from identical thermal fluctuations), then there is no change in the output voltage. If R_{cr} increases in the presence of an analyte while R_d does not, then the output voltage will decrease proportionately. Figure 13-8 below shows the calculated kinetic voltage output of the Wheatstone bridge (Eq. 13-2) for the fluctuating conductance baselines from previous Figure 13-3. For these sensors we recall that R_{cr} / R_d is 0.884, which is the value obtained from previous Figure 13-4. The Wheatstone baseline is similar to that of Figure 13-6, but it is now in terms of output voltage instead of conductance. Again, corrected thermal fluctuations are only 0.7% of the baseline (a signal-to-noise ratio of ~2), whereas those from the uncorrected curve are ~17%.

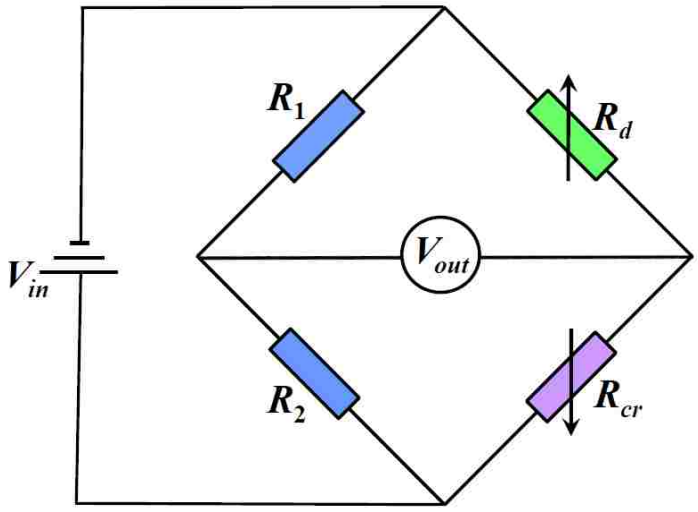

Figure 13-7. Circuit diagram for a Wheatstone bridge in a *half-bridge* configuration. R_d and R_{ch} are the *dummy* (analyte isolated) and and analyte chemiresitors, respectively, and R_1 and R_2 are fixed resistors. The fixed resistors are chosen (or adjusted) such that $R_1/ R_2 = R_d/ R_{cr}$, which yields an output voltage, V_{out}, equal to zero. When this ratio changes (i.e. R_{cr} increases disproportionately to R_d) due to the presence of an analyte, the circuit becomes unbalanced and V_{out} becomes non-zero.

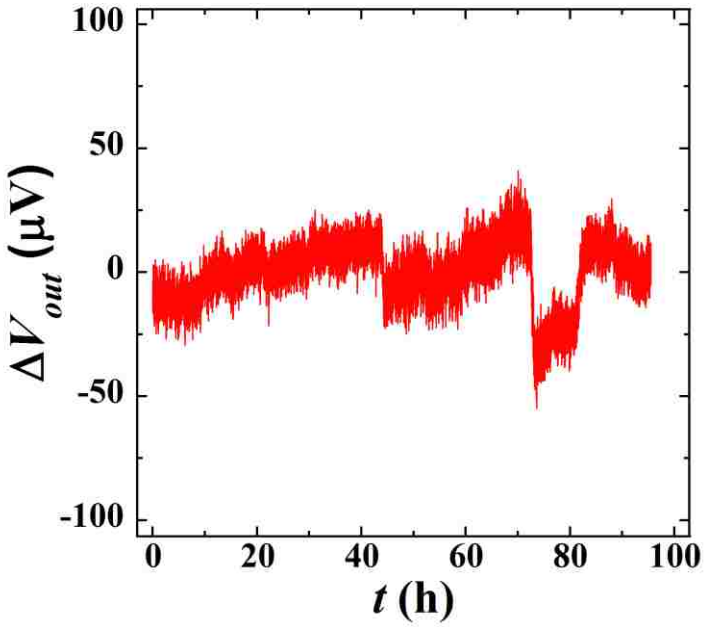

Figure 13-8. The corrected baseline is the output voltage from the Wheatstone bridge circuit. This baseline correction reduces temperature-induced fluctuations from ~17 to 0.7 %. Changes in V_{out} elicited by an analyte would be proportional to the change in conductance.

13.4. Conclusions

We have demonstrated a method for mitigating FSCR baseline drift due to ambient temperature fluctuations, which was shown to decrease baseline fluctuations from17 to 0.7%—a 23-fold decrease. This method relies on using a *dummy* chemiresistor that is isolated from possible analyte exposure to determine baseline fluctuations that are due solely to temperature. The method can be implemented using a simple circuit known as the Wheatstone bridge, which has zero output voltage when the resistances of the two chemiresistors change commensurately and a non-zero voltage when the resistance of the analyte chemiresistor changes disproportionately to the dummy sensor. This Wheatstone bridge is well suited to a field instrument where low power and simplicity are required, but where ambient fluctuations are present.

14. PROJECT CONCLUSIONS

14.1. Conclusion Statement

Unlike traditional chemiresistors, whose particle network is random, our approach is to force the conducting particles into well-organized percolative pathways to eliminate randomness from the particle composite. We have demonstrated that this field structuring of the particle phase leads to significantly improved chemiresistors, which is characterized by high sensitivity, reversibility, and response and sensor reproducibility. We have demonstrated that FSCRs transition from a conductor to an insulator over very narrow concentration ranges such that these devices can be described as chemical switches. We have shown that the sensitivity and response range of these sensors can be permanently or dynamically tailored over a wide range by controlling the stress within the composite, including through the application of a magnetic field or tensile strain. Such tailorable sensors can be used to create sensor arrays that can accurately determine analyte concentration over a broad concentration range, or can be used to create simple logic circuits that signal a particular chemical environment. It was shown through combined mass-sorption and conductance measurements, that the response curve of any individual sensor is a function of polymer swelling *alone*. This has the important implication that individual sensor calibration requires testing with only a single analyte. In addition, we demonstrated a method for analyte discrimination based on sensor response kinetics. This method is concentration independent and allows for discrimination even between chemically similar analytes based on only the analytes' saturation vapor pressures. In closing, these sensors fill a niche as a reliable, low-cost, low-power, tunable chemical sensor that could be used for applications ranging from military and home-land defense to environmental monitoring.

14.2. Bulleted Project Accomplishments

During the course of this project we have:

- developed of a vastly enhanced class of chemiresistors, which include improvements in: response reversibility, stability, and reproducibility (in terms of response and sensor-to-sensor fabrication), and sensitivity;
- isolated the variables that affect sensor response leading to complete control, and permanent and dynamic tunability of sensitivity and range. This has led to the development of *homo*-polymer chemical-switch arrays that maintain high sensitivity over the entire range of analyte concentrations;
- furthered the understanding of charge transport in field-structured composites and the variables that affect it;
- isolated the transduction mechanism of FSCRs leading to a new method for single-analyte calibration of polymer-selective sensors in general, and as a corollary this can be used as a simple and cost effective method to determine polymer-analyte interaction energies;
- developed a novel method for analyte discrimination for any selective-polymer based sensor that is independent of analyte concentration;
- described a simple, low-power method for mitigating false-positive response due to temperature fluctuations, which is suitable for a field unit;
- written five first-author publications (including a cover article in *Advanced Functional Materials*), and four patents/patent disclosures (pending). This research was selected to represent Sandia Labs as a 2007 *R&D 100* award application.
- FSCRs patents have been licensed by Smiths Detection and EmNet with licensing underway for Therm-O-Disc. EmNet is company specializing in environmental monitoring and control through embedded sensor networks that provide real-time analysis of large areas through interconnected wireless sensor nodes.

14.3. Publications

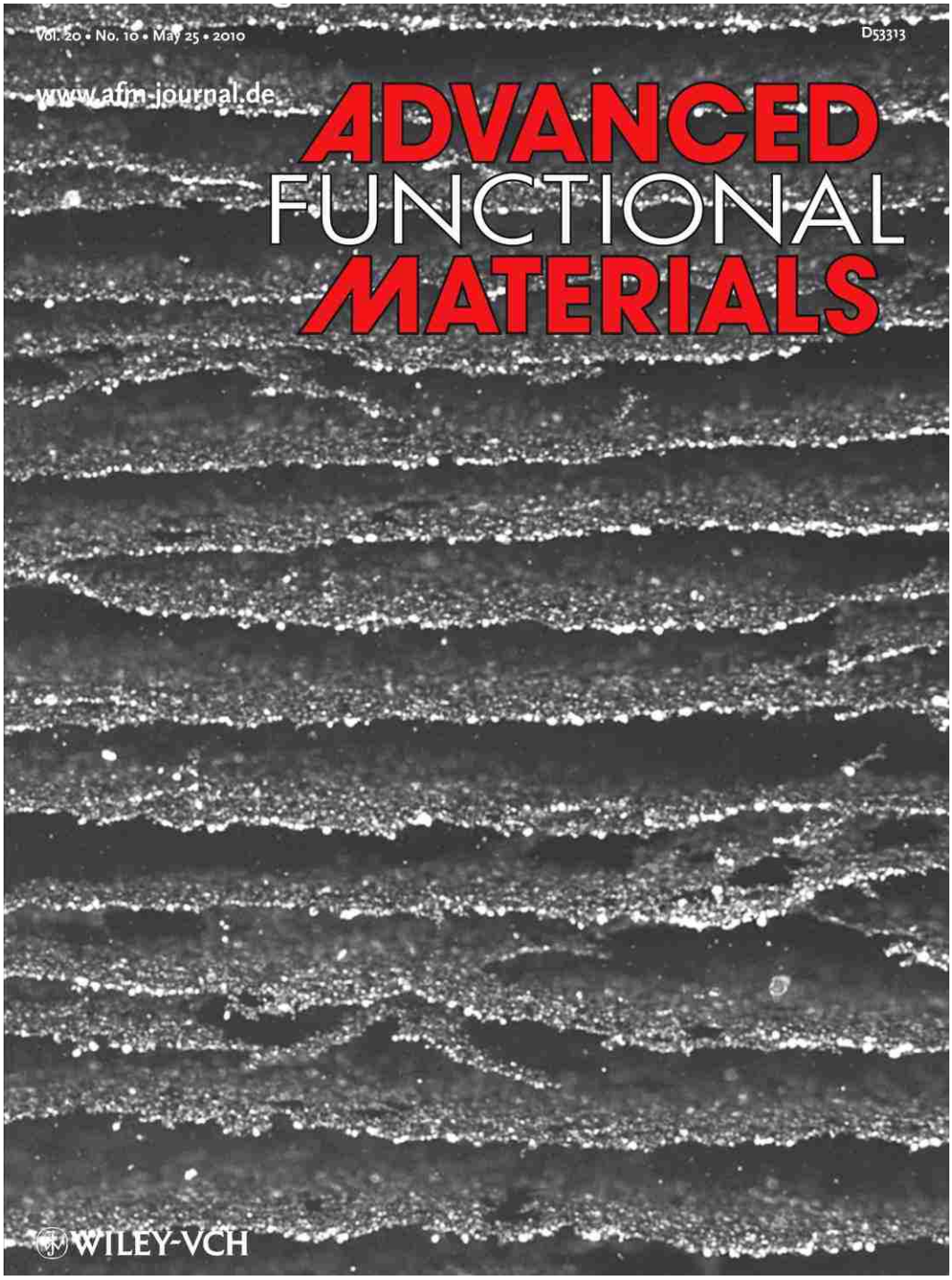

Figure 14-1. Inside cover of *Advanced Functional Materials*, Vol. 20, No. 10.

The following lists include *all* publications published during my Sandia Internship.

14.3.1. JOURNAL PUBLICATIONS

- Read, D. H., Martin, J.E. ***Field-Structured Chemiresistors***, **Cover Article**, *Advanced Functional Materials,* 20 (10), 2010, pp 1577–1584.
- Read, D. H., Martin, J.E. ***Strain-Tunable Chemiresistor***, *Analytical Chemistry*, 2010, 82 (5), pp 2150–2154.
- Read, D. H., Martin, J.E. ***A Master Transduction Curve for Field-Structured Chemiresistor Calibration***, *Analytical Chemistry* 20 (12), 2010, pp 5373–5379.
- Read, D. H., Martin, J.E. ***Analyte Discrimination from Chemiresistor Response Kinetics***, *Analytical Chemistry* (accepted pending minor revisions), 2010.
- Read, D. H., Martin, J.E. ***Role of Stress on Field-Structured Chemiresistor Response***, *Journal of the American Chemical Society* (in preparation, to be submitted by August, 2010).
- Martin, J.E., Read, D.H., Williamson, R.E. ***Field-Structured Chemiresistors (FSCRs): Tunable Chemical Switches for Sensor Arrays***, *R&D 100 Award Application*, 2007.
- Martin, J.E., Anderson, R.A., Read, D.H., Gulley, G. L. ***Magnetostriction of Field-Structured Magnetoelastomers***, *Physical Review E*, 74, 051507, 2006.

14.3.2. PATENTS AND PATENT DISCLOSURES

- Martin, J.E., Read, D.H. "Stress-Tuned Conductor-Polymer Composite for Use in Sensors*", U.S. Patent Pending*, 2007.
- Read, D. H., Martin, J.E. "A Method for Dynamic Sensitivity Tuning of Conductor-Polymer Composite Chemical Sensor Using Tensile Strain"*, U.S. Patent Application,* 2010.
- Martin, J.E., Read, D. H., "Methods for Increasing Sensitivity of Conductor-Polymer Composite Chemical Sensors by Reducing Volumetric Compressive Stresses", *SNL Patent Disclosure* (in preparation, to be submitted by Aug, 2010).
- Read, D. H., Martin, J.E. "A Method for Analyte Discrimination from Response Kinetics of Selective-Polymer-Based Chemical Sensors", *SNL Patent Disclosure* (in preparation), 2010.

14.3.3. INTERNAL PUBLICATIONS

- "Phase Changing Dielectrics for High Performance Pulsed Power Switches", Glover, S.F., Martin, J.E., Read, D.H., Reed, K.M., Rudys, J.M., Schneider, L.X., *SNL Report: SAND2007-5886P*, 2007.
- "Magnetostriction of Field-structured Magnetoelastomers", Huber, D.L., Martin, J.E., Anderson, R.A., Read, D.H., Frankamp, B.L., *SNL Report: SAND2005-8032*, 2005.
- "The Relationship between Interfacial Interactions and Crack Initiation: Effect of a Singular Stress Field", Kent, M.S., Yim, H., Read, D.H., Yuen, W., Reedy, E.D., *SNL Report: SAND2005-0577C and* SAND2005-0576C, 2005.
- "Dewetting of Thin Epoxy Films", Giunta, R., Kent, M.S., Weems, J.S., Read, D.H., Tallant, D.R., Garcia, M.J., Hammerand, S.T., *SNL Report: SAND2004-0679P*, 2004.
- "Resolving Fundamental Limits of Adhesive Bonding in Microfabrication", Giunta, R.K., Emerson, J.A., Lamppa, K.P., Holmes, M.A., Kent, M.S., Hall, J.S., Read, D.H., Adkins, D.R., Frischknecht, A.L., Kawaguchi, S.T., *SNL Report: SAND2004-0482*, 2004.
- "Using Self-Assembled Monolayers to Explore the Relationship Between Interfacial Interactions and Fracture in Structural Adhesive Joints", Kent, M.S., Yim, H., Read, D.H., Yuen, W., Reedy, E.D., *SNL Report: SAND2002-2735P*, 2002.

Figure 14-2. 2007 *R&D 100 Award* entry with triaxial Helmholtz coils.

REFERENCES

[1] Pottie, G.J.; Kaiser, W.J. *Commun. ACM*. **2000**, *43*(5), 51–58.

[2] Delin, K.A.; Jackson, S.P.; Johnson, D.W.; Burleigh, S.C.; Woodrow, R.R.; McAuley, J.M.; Dohm, J.M.; Ferré, F. Ip, T.P.A.; Rucker, D.F.; Baker, V.R. *Sensors* **2005**, *5*, 103–117.

[3] Seders, L.A.; Shea, C.A.; Lemmon, M.D.; Maurice, P.A.; Talley, J.W. *Environ. Eng. Sci.* **2007**, *24*(2), 183–191.

[4] Fraden, J. *Handbook of Modern Sensors: Physics, Designs, and Applications, 3rd ed.* **2003**, Spinger.

[5] GC Help Page, http://www.gchelp.tk/

[6] Sparkman, D.O. *Mass spectrometry desk reference*. Pittsburgh: Global View Pub., ISBN 0-9660813-2-3 (2000)

[7] Hierlemann, A.; Ricco, J.; Bodenho, K.; Dominik, A.; Golpel, W. *Anal. Chem.* **2000**, *72*, 3696–3708.

[8] Wibawa, G.; Takahashi, M.; Sato, Y.; Takishima, S.; Masuoka, H. *J. Chem. Eng. Data* **2002**, *47*, 518–524.

[9] Ho, C.K.; Lindgren, E.R.; Rawlinson, K.S.; McGrath, L.K.; Wright, J.L. *Sensors* **2003**, *3*, 236–247.

[10] Fang, M.; Vetelino, K.; Rothery, M.; Hines, J.; Frye, G.C. *Sens. Actuators, B* **1999**, *56*, 155–157.

[11] Janata, J. *Electroanalysis* **2004**, *16* (22), 1831–1835.

[12] Wilson, M.W.; Hoyt, S.; Janata, J.; Booksh, K.; Obando, L. *IEEE Sensors J.* **2001**, *1* (4), 256–274.

[13] Patel, S.V.; Mlsna, T.E.; Fruhberger, B.; Klaassen, E.; Cemalovic, S.; Baselt, D.R. *Sens. Actuators, B* **2003**, *96*, 541–553.

[14] Donaghey, L.F. Resistive Hydrocarbon Leak Detector. U.S. Patent 4,631,952, December 30, 1986.

[15] Lewis, N.S; Doleman, B.J; Briglin, S; Severin, E.J. Colloidal particles used in sensing arrays. U.S. Patent 6,537,498, March 25, 2003.

[16] Lundberg, B.; Sundqvist, B. *J. Appl. Phys.* **1986**, *60* (3), 1074–1079.

[17] Lei, H.; Pitt, W. G.; McGrath, L. K.; Ho, C. K. *Sens. Actuators, B* **2004**, *101*, 122–132.

[18] Ho, C. K.; Hughes, R. C. *Sensors* **2002**, *2*, 23–34.

[19] Doleman, B. J.; Lonergan, M. C.; Severin, E. J.; Vaid, T. P.; Lewis, N. S. *Anal. Chem.* **1998**, *70* (19), 4177–4190.

[20] Grate, J.W. *Chem. Rev.* **2008**, *108*, 726–745.

[21] Kim, Y.S.; Ha, S.C.; Yang, Y.; Kim, Y.J.; Cho, S.M.; Yang, H.; Kim, Y.T. *Sens. Actuators, B* **2005**, *108*, 285–291.

[22] Eastman, M.P.; Hughes, R.C.; Yelton, G.; Ricco, A.J.; Patel, S.V.; Jenkinsb, J. *Electrochem Soc.* **1999**, *146* (10), 3907–3913.

[23] Lu, C.; Lewis, O. *J. Appl. Phys.* **1972**, *43*, 4385.

[24] Russell, S. P.; Weinkauf, D. H. *Polymer* **2001**, *42***,** 2827.

[25] Moseley, P. T. *Meas. Sci. Technol.* **1997**, *8*, 223–237.

[26] Figaro Sensor Inc., http://www.figarosensor.com/

[27] Juanta, J. Thirty Years of ChemFETs – a personal view, Electroanalysis, **2004**, 16(22), 1831 - 1835

[28] Yang, D.R.; Park, J.; Colesniuc, C.N.; Schuller, I. K.; Royer, J. E.; Trogler, W. C.; Kummel, A.C. *J. Chem. Phys.* **2009**, 130, 164703.

[29] Seacoast Science, Inc. "White Paper"
http://www.seacoastscience.com/technology.htm

[30] Read, D. H.; Martin, J. E. *Anal. Chem.* **2010**, 82, 2150–2154.

[31] Safran, S.A.; Webman, I.; Grest, G.S. *Phys. Rev. A* **1985**, *32*, 506–511.

[32] Lux, F. *J. Mater. Sci.* **1993**, *28*, 285–301.

[33] Martin, J.E.; Anderson, R.A.; Odinek, J.; Adolf, D.; Williamson, J. *Phys. Rev. B* **2003**, *67*, 094207–094218.

[34] Lonergan, M.C.; Severin, E.J.; Doleman, B.J.; Beaber, S.A.; Grubbs, R.H.; Lewis, N.S. *Chem. Mater.* **1996**, *8*, 2298–2312.

[35] J.E. Martin, R.C. Hughes, and R.A. Anderson, *United States Patent #6,194,769 B1*, **2001**.

[36] J.E. Martin, R.C. Hughes, and R.A. Anderson, *United States Patent #6,290,868,* **2001**.

[37] J.E. Martin, R.A. Anderson, R.L. Williamson, *J. Chem. Phys.*, **2003**, *118* 1557–1570.

[38] J.E. Martin, E. Venturini, G. Gulley, J. Williamson, *Phys. Rev. E*, **2004**, *69*, 21508.

[39] J.E. Martin, R.A. Anderson, R.L. Williamson, *United States Patent #6,844,378,* **2005**.

[40] Flory, P.J. *J. Chem. Phys.* **1942**, *10*, 51–61.

[41] Huggins, M.L. *Ann. NY Acad. Sci.* **1942**, *43*, 1–32.

[42] Flory, P. J. *Princliples of Polymer Chemistry*, Cornell University, Ithaca and London, **1953**, Ch. XII-1f.

[43] Yaws, C.L.; Narasimhan, P. K.; Gabbula, C. *Yaws' Handbook of Antoine Coefficients for Vapor Pressure*, 1st Electronic Edition; Knovel: 2005.

[44] Ho, C. K.; McGrath, L. K.; Davis, C. E.; Thomas, M. L.; Wright, J. L.; Kooser, A. S.; Hughes, C. K. Sandia National Laboratories SAND Report, , *Chemiresistor Microsensors for In-Situ Monitoring of Volitile Organic Compounds: Final LDRD Report* **2003**, SAND2003-3410.

[45] Colin D.; Bain, E.; Troughton, B.; Tao, Y. T.; Evall, J.; George M.; Whitesides, R.; Nuzzo, *G* J. *Am. Chem. Soc.* **1989**, *111*(1), 321–335.

[46] Read, D. H.; Martin, J. E. Field-Structured Chemiresistors. *Adv. Funct. Mater. submitted, preprint available on request.*

[47] Martin, J.E.; Anderson, R.A.; Read, D.H.; Gulley G.L. *Phys. Rev. E* **2006**, *74*, 051507.

[48] Kchit, N.; Bossis, G. *J. Phys. D: Appl. Phys.* **2009**, *42*, 105505.

[49] Niezrecki, C.; Brei, D.; Balakrishnan, S.; Moskalik, A. *A. Shock Vibr. Dig.* **2001**, *33(4)*, 269-280.

[50] Barton, A. F. M. *CRC Handbook of Polymer-Liquid Interaction Parameters and Solubility Parameters*, **1990**, CRC Press: Boca Raton, FL.

[51] Krasteva, N.; Fogel, Y.; Bauer, R.E.; Müllen, K.; Joseph, Y.; Matsuzawa, N.; Yasuda, A.; Vossmeyer, T. *Adv. Func. Mater*. **2007**, *17*, 881–888.

[52] Zamborini, F.P.; Leopold, M.C.; Hicks, J.F.; Kulesza, P.J.; Malik, M.A.; Murray, R.W. *J. Am. Chem. Soc.* **2002**, *124*, 8958–8964.

[53] Leopold, M.C.; Donkers, R.L.; Georganopoulou, D.; Fisher, M.; Zamborini, F.P.; Murray, R.W. *Faraday Discuss.* **2004**, *125*, 63–76.

[54] Han, L.; Daniel, D.R.; Maye, M.M.; Zhong, C.J. *Anal. Chem.* **2001**, *73*, 4441–4449.

[55] Sauerbrey, G. *Z. Phys*. **1959**, *155*, 206–222.

[56] Martin, S. J.; Frye, G. C.; Senturia, S.D. *Anal. Chem*. **1994**, *66*, 2201–2219.

[57] Vogt, B.D.; Lin E.K.; Wu, W.L.; White, C.C. *J. Phys. Chem. B* **2004**, *108*, 12685–12690.

[58] Reed, C. E.; Kauazawa, K. K.; Kaufman, J. H. *J. Appl. Phys*. **1990**, *68* 1993–2001.

[59] Lucklum, R.; Behling, C.; Hauptmann, P. *Anal. Chem*. **1999**, *71*, 2488–2496.

[60] Zhang, Y.; Ge, S.; Rafailovich, M.H.; Sokolov, J.C.; Colby, R.H. *Polymer* **2003**, *44*, 3327–3332.

[61] Errede, L.A. 1992, *J. Appl. Polym. Sci.* **1992**, *45*, 619–631.

[62] Welty, J.R., Wicks, C.E., Wilson, R.E., Rorrer, G., *Fundamentals of Momentum, Heat, and Mass Transfer*, 4th Ed., **2001**, John Wiley & Sons, Inc., New York, Chapter 26.

[63] Martin, J. E.; Anderson, R. A.; Tigges, C. P. *J. Chem. Phys.* **1998**, 108, 3765–3788

[64] http://www.efunda.com/designstandards/sensors/methods/wheatstone_bridge.cfm

[65] National Instruments Inc., http://zone.ni.com/devzone/cda/tut/p/id/3432, "How Is Temperature Affecting Your Strain Measurement Accuracy?"

APPENDICES

A. SYMBOLS

a	analyte activity, the partial pressure of an analyte divided by its partial pressure at saturation
$a_{1/2}$	response midpoint of a sensor in terms of activity
a^*	fictive activity
$a_{1/2,swollen}$	the response midpoint of a sensor after post-cure swelling
C	analyte concentration in units of μg/mL or *ppm*
$C_{1/2}$	response midpoint of a sensor in terms of concentration
χ	Flory interaction parameter for a particular analyte-polymer pair
χ_s	entropic contribution to the Flory parameter in the Laar-Hildebrand equation
d	particle diameter
d	composite film thickness
D_t	diffusion coefficient
δ_1	Hildebrandt solubility parameter of the analyte
δ_2	Hildebrandt solubility parameter of the polymer
e	Cauchy (uniaxial) strain
$e_{1/2}$	the response midpoint of a sensor in terms of Cauchy strain
F	volumetric flowrate (mL/min)
ϕ	volume fraction of absorbed analyte
$\phi_{1/2}$	response midpoint of a sensor in terms of volume fraction of absorbed analyte
ϕ_∞	volume fraction of absorbed analyte at infinite time (or thermodynamic equilibrium)
ϕ_{vap}	volume fraction of analyte in the vapor phase
ϕ^*_{vap}	volume fraction of analyte in the vapor phase at saturation
G	sensor conductance at a particular analyte concentration (Siemens, S)
G_0	sensor conductance baseline when no analyte is present (Siemens, S)
γ	inverse sensitivity in the limit of low analyte concentration
γ_0	inverse initial sensitivity for an unswollen sensor

Γ	constant of the response curve that parameterizes the slope of an FSCR's conductor-insulator transition
k	slope of the mass-sorption isotherm
K	analyte-polymer partition coefficient
L	electrode gap length, or the distance between sensor substrate electrodes
LDL	sensor lower detection limit in terms of analyte concentration or activity
M_w	molecular weight
n	number of moles of a chemical
p	analyte partial pressure
p^*	analyte saturation partial pressure
P_{ch}	fraction or probability of a single non-conducting chain of particles in an FSC
P_0	probability of a non-conductive particle-particle contact in a chain of particles
ppm	part-per-million, or the number of moles of analyte divided by the number of moles of carrier gas times one-million
r	circuit efficiency
R	ideal gas constant
R	sensor resistance (Ω)
R_0	initial sensor resistance in the absence of an analyte (Ω)
ρ	analyte density (μg/mL)
R^2	the square of the Pearson correlation coefficient
S	sensor sensitivity, or the derivative of the response curve
S_0	initial sensor sensitivity (in the limit of low analyte concentration)
S	Siemens, the SI unit of conductance
σ	standard deviation
σ_{G0}	standard deviation of the sensor's baseline conductance
T	temperature (°C)
t	time
τ_{meas}	measured characteristic sensor response time
τ_d	characteristic analyte diffusion time into a polymer
τ_f	characteristic time for the analyte concentration in a flowcell to reach steady state

UDL	sensor upper detection limit in terms of analyte concentration or activity
V_1	molar volume of an analyte (μL/mol)
V_f	volumetric flowrate of carrier gas

B. GLOSSARY OF TERMS

activity	The concentration of a chemical vapor normalized by its concentration at total saturation. It is defined as
analyte	The chemical of interest for purposes of detection.
artificial nose	An array of sensors with polymers differing in their selectivity, whose
baseline	The magnitude of the transduction signal when no analyte is present.
CBCR	Carbon-Black Chemiresistor
CTE	Coefficient of Thermal Expansion
ChemFET	Chemical Field Effect Transistor
chemicapacitor	A capacitor-based sensor whose analyte selective polymer serves as the dielectric medium of the capacitor. The disparate permittivity of the absorbing analyte changes the capacitance of the device.
chemiresistor	A device whose resistance changes in the presence of a chemical.
dynamic range	The ratio of the upper and lower detection limits.
FSC	Field-Structured Composite
FSCR	Field-Structured Chemiresistor
LDL	Upper Detection Limit. The highest concentration that a sensor can detect.
magnetostriction	The property of an FSC material to constrict in a magnetic field.
MOS	Metal Oxide Semiconductor
offset	(see baseline)
range	The magnitude of the span of the response curve, e.g. 10 μg/mL xylene.
response time	The amount of time required for a sensor to fully respond to a change in analyte concentration
selectivity	An increased sensitivity to a specific class of analytes and lower sensitivity to others.
sensitivity	The slope or derivative of the sensor response curve.
UDL	Lower Detection Limit. The lowest concentration that a sensor can detect.

C. DERIVATIONS AND CALCULATIONS

C.1. CONCENTRATION CONVERSIONS

Definition of activity:

$$a_{1,fc} \equiv \frac{P_1(T_{fc})}{P_1^*(T_{fc})} \tag{1}$$

Raoult's Law:

$$P_1 = P_{tot} \cdot y_1 \equiv \frac{P_{tot} \cdot \dot{n}_1}{\dot{n}_1 + \dot{n}_{N_2,b}} \tag{2}$$

Eqn (2) into (1) yields:

$$a_{1,fc} \equiv \frac{P_{tot} \cdot \dot{n}_1}{P_{1,fc}^* \cdot (\dot{n}_1 + \dot{n}_{N_2})} \tag{3}$$

$$C_1 = \frac{\dot{n}_1 \cdot mw_1}{\dot{V}_{N_2}} \tag{4}$$

Ideal Gas Law for nitrogen:

$$\dot{V}_{N_2} = \frac{\dot{n}_{N_2} \cdot R_{ig} \cdot T(K)}{P_{amb}} \tag{5}$$

Substituting eqn.5 into eqn.4:

$$C_1 = \frac{\dot{n}_1 \cdot mw_1 \cdot P_{amb}}{\dot{n}_{N_2} \cdot R_{ig} \cdot T(K)} \text{ rearranged as, } \dot{n}_{N_2} = \frac{\dot{n}_1 \cdot mw_1 \cdot P_{amb}}{C_1 \cdot R_{ig} \cdot T(K)} \tag{6}$$

Substituting eqn.6b into eqn.3 and simplifying:

$$a_{1,fc} = \frac{P_{tot} \cdot \dot{n}_1}{P_{1,fc}^* \cdot \left(\dot{n}_1 + \frac{\dot{n}_1 \cdot mw_1 \cdot P_{amb}}{C_1 \cdot R_{ig} \cdot T(K)} \right)} = \frac{1}{P_{1,fc}^* \cdot \left(\frac{1}{P_{amb}} + \frac{mw_1}{C_1 \cdot R_{ig} \cdot T(K)} \right)} \tag{7}$$

Concentration in terms of parts-per-million (*ppm*):

$$C_1(ppm) \equiv \frac{n_1}{n_{N_2}} \times 10^6 \; ppm = \frac{C_1(\mu g / mL) \cdot R_{ig} \cdot T(K)}{mw_1 \cdot P_{atm}} \times 10^6 \; ppm \tag{8}$$

C.2. BUBBLER MODEL

Ideal Gas Law:

$$\dot{n}_{N_2,b} = \frac{P_{amb} \cdot \dot{V}_{N_2,b,STP}}{R_{ig} \cdot T_{amb}(K)} \tag{1}$$

Raoult's Law for Single Condensable Species:

$$y_1 \equiv \frac{\dot{n}_1}{\dot{n}_1 + \dot{n}_{N_2,b}} = \frac{P_1}{P_{tot}} \text{ rearranged as } \dot{n}_1 = \frac{\dot{n}_{N_2,b}}{P_{tot}/P_1 - 1} \tag{2}$$

Assuming nitrogen exits the bubbler fully saturated with analyte at thermodynamic equilibrium:

$$P_{1,b} = P_1^*(T_b) = P_{1,b}^* \tag{3}$$

Inserting equations (1) and (3) into (2) yields an expression for the molar flow rate of analyte entrained in the bubbler effluent:

$$\dot{n}_1 = \frac{\dot{V}_{N_2,b,STP}}{R_{ig} \cdot (T_{amb} + 273.15) \cdot \left(\frac{1}{P_{1,b}^*} - \frac{1}{P_{tot}} \right)} \tag{4}$$

The analyte's saturation vapor pressure is represented by the Antoine equation as:

$$\log_{10}\left(P_1^*\right) = A_1 - \frac{B_1}{T + C_1} \tag{5}$$

The total flow rate of nitrogen through the flow-cell is the sum of that of the dilution stream and that flowing through the bubbler:

$$\dot{V}_{N_2,fc} = \dot{V}_{N_2,b} + \dot{V}_{N_2,d} \tag{6}$$

Again, from the ideal gas law:

$$\dot{n}_{N_2,fc} = \frac{P_{fc} \cdot \dot{V}_{N_2,fc}}{R_{ig} \cdot (T_{fc} + 273.15)} \tag{7}$$

Definition of activity and from Raoult's Law (eqn.2):

$$a_{1,fc} \equiv \frac{P_1(T_{fc})}{P_1^*(T_{fc})} = \frac{P_{tot} \cdot y_{1,fc}}{P_1^*(T_{fc})} = \frac{P_{tot} \cdot \dot{n}_1}{P_{1,fc}^* \cdot (\dot{n}_1 + \dot{n}_{N_2,fc})} \tag{8}$$

Substituting the expressions for the molar flow rates of analyte (eqn.4) and nitrogen (IGL, eqn.7) into the definition of activity (eqn.8) yields the model for the analyte concentration in the flow-cell using the bubbler system:

$$a_{1,fc} = \frac{1}{P_{1,fc}^* \cdot \left[\frac{1}{P_{tot}} + \frac{\dot{V}_{N_{2,tot}}}{\dot{V}_{N_{2,bt}}} \cdot \left(\frac{1}{P_{1,b}^* - 1} \right) \right]} \tag{9}$$

The concentration can be calculated in terms of mass of analyte per unit of nitrogen volume as:

$$C_1(\mu g / mL) = \frac{\dot{m}_1}{\dot{V}_{N_2}} = \frac{\dot{n}_1 \cdot mw_1}{\dot{V}_{N_2}}. \tag{10}$$

E. EXPERIMENTAL DETAILS

E.1. ELECTROLESS GOLD-PLATING PROCEDURE

This is a mildly acidic, self-limiting immersion gold plating process for coating nickel to a thickness if 80-130 nm

WARNING CYANIDE, HANDLE WITH CARE AND READ MSDS!

Enthone Gold Plating Kit:

- Lectroless Prep Unit A (PCN: 210000-001): KAu(CN)2
- Lectroless Prep Unit B (PCN: 21004-001): EDTA, citric acid, proprietary ammonium compounds

A. Solution Preparation

1. Dissolve 5.3 g Unit B in 50 mL DI water at 65°C.
2. Dissolve 0.59 g Unit A in 25 mL DI water at 65°C.
3. Mix the two solutions and adjust the total volume to 100 mL with DI water.
4. Allow the solution to cool to near room temperature and adjust pH to 4.0 using either KOH (20% by weight) to raise the pH or H3P04 (20% by volume) to lower the pH.

B. Coating Procedure

1. Place 100 mL solution in 250 mL beaker and place in heating mantle.
2. Place stirring propeller in the solution at an angle such the Eddie current is asymmetric and there is turbulence (this helps to keep the particles from settling and clumping).
3. While stirring stabilize the solution at 85°C using a heating mantle.
4. Place 1g of 4–7 mm nickel particles in the solution.
5. Use a dropper or wash bottle with DI water to top-off the evaporating water and to wash the particles from the side of the beaker.
6. The reaction should take 15 min. The particles should become brown in color (looks like cinnamon) and solution should turn from clear to light blue.
7. Quench the reaction by filling with cold water. Suck down and hold the particles in place with a magnet while pouring out the solution (this is HAZ waste). Immediately fill with cold DI water. This entire step 7 should be done very quickly to prevent the particles from plating together while concentrated.

8. The solution is then rinsed a total of three times with water (stir, decant, fill). The particles are then transferred to a 20 mL scintillation vial with propanol and ultra-sonicated for ~10 min. decant and sonicate in isopropanol one more time.
9. Decant the isopropanol and let dry (mild heating in an oven will speed things up).
10. Place glass beads or ball bearings in the vial with the dry powder and shake, or vortex mix, to break up the clumps. Take caution to not over shake the powder, which will prevent ball-milling the powder.

E.2. DETAILED FSCR FABRICATION

Synthesis Steps for solvent-cast field-structured chemiresistors:

1. Mix equal parts of the silicone (by mass or volume – recall that the density of the silicone is ~1 g/mL). Make more than needed, mix, and then take the amount needed from this mixture. The dependence of polymer cure-time on catalyst concentration is shown in Figure E-1 below.
2. Use a small metal spatula to dab the necessary mass of pre-mixed silicone into a small glass vial. Do this by weight on a microbalance.
3. Use a small metal spatula to add the needed mass of particles to the same vial.
4. Use a calibrated finntip pipette to transfer the required amount of hexane to the vial. **Cap the vial quickly**. This whole step must be done quickly before the highly volatile hexane evaporates. Make sure you calibrate your transfer method by mass to ensure you get the right mass/volume of hexane in the vial. Do this by practicing transferring the hexane to vials and then weighing them. For instance, I have to set my pipette to suck up ~30% more hexane to end up with the correct amount.
5. Mix the contents of the vial well with a vortex mixer.
6. To deposit the composite precursor on your substrate, there are a couple of methods depending on how big your substrate/electrode is. If a fair amount of precursor is needed (~3-5 mm diameter chemiresistor), then use a micro-pipette that can deposit as little as 5 μL. When dealing with very small substrates (1-2 mm diameter chemiresistors), use a needle to dab into the liquid and then drag the drop on the needle between the electrodes to deposit the material. Either way, make sure to give a quick mix on the vortex mixer before pull out your material or else the particles will have settled to the bottom and you will not be pulling out a homogeneous aliquot. Also keep the cap on the vial to prevent your solvent from evaporating. Vortex mixing every time is not necessary when not solvent casting.
7. Now place the chemiresistor in the magnetic field and let cure.

Here is an example of the quantities used when for a typical batch of chemiresistors for research purposes (very small quantities to save on materials (especially gold-plated nickel).

1. Thoroughly mix 0.25g of part A with 0.25g of part B (for a total mass of 0.5g silicone) in a small weigh dish with a rod or spatula.
2. Using a small metal spatula, dap 0.1g of the mixed silicone into a 10mL scintillation vile.
3. Add 0.157g gold-plated nickel to the vial. Recall m_Ni=[(vol_frac_Ni)x(density_Ni)x(Vol_silicone)]/(1-vol_frac_Ni) or in this case: m_Ni=[(0.15)x(8.9g/mL)x(0.1mL)]/(1-0.15)=0.157g.
4. When using the solvent casting method, do not mix the two of these together with a stirring rod. There is so little material that you will end up with an appreciable amount sticking to the stirring rod, which will throw off your solvent casting quantities. Instead transfer 0.1mL of hexane to the vial. Cap and mix with a vortex mixer.

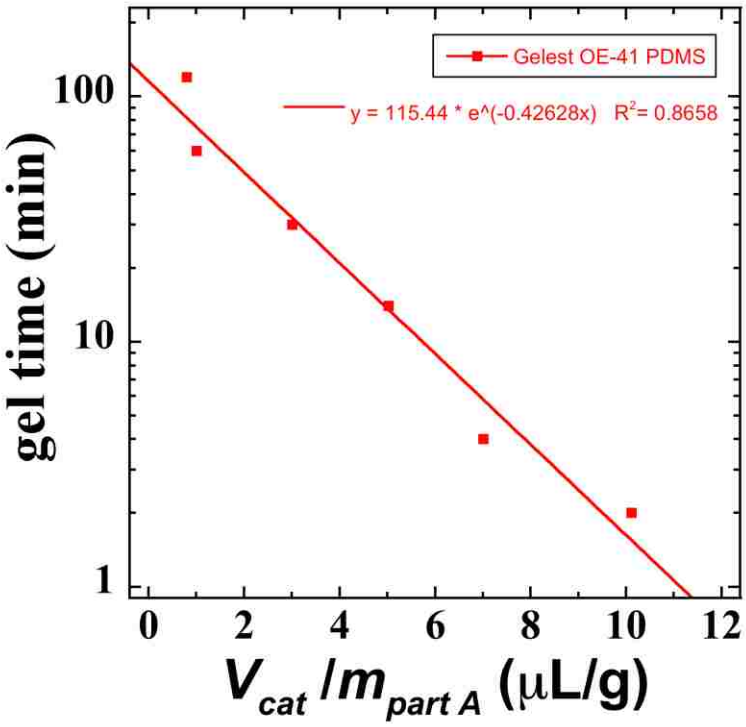

Figure E-1. Cure time for the Gelest OE-41 PDMS as a function of catalyst concentration shows an exponential decrease in gel time with increasing catalyst. Here V_{cat} is the volume of Pt-divinyl tetramethyl-disiloxane catalyst and $m_{part\ A}$ is the mass of the crosslinker resin.